Stony Brook University

Exploring the Role of Serotonin on Hypoglossal Motoneuron Excitability and Plasticity Through Postnatal Development Via Mathematical Models

A Dissertation Presented

by

Kyle Graham Horn

to

The Graduate School

in Partial Fulfillment of the

Requirements

for the Degree of

Doctor of Philosophy

in

Neuroscience

(Concentration – Computational Neuroscience)

Stony Brook University

December 2013

Stony Brook University
The Graduate School

Kyle Graham Horn

We, the dissertation committee for the above candidate for the
Doctor of Philosophy degree, hereby recommend
acceptance of this dissertation.

Irene C. Solomon – Dissertation Advisor
Professor of the department of Physiology & Biophysics

William F. Collins, III - Chairperson of Defense
Associate Professor of the department of Neurobiology & Behavior

Alfredo Fontanini - Member of Defense Committee
Assistant Professor of the department of Neurobiology & Behavior

Robert J. Butera – Outside Member of Defense Committee
Professor of Bioengineering, School of Electrical and Computer Engineering
and
Wallace H. Coulter Department of Biomedical Engineering
Georgia Institute of Technology, Atlanta, GA
(Disciplines: Computational Neuroscience, Neuroengineering, Neurophysiology)

This dissertation is accepted by the Graduate School

Charles Taber
Dean of the Graduate School

Abstract of the Dissertation

Exploring the Role of Serotonin on Hypoglossal Motoneuron Excitability and Plasticity Through Postnatal Development Via Mathematical Models

A Dissertation Presented

by

Kyle Graham Horn

Doctor of Philosophy

in

Neuroscience

(Concentration – Computational Neuroscience)

Stony Brook University

2013

Neuronal plasticity is a key facet of neurons throughout the central and peripheral nervous system. Unlike most forms of plasticity, however, dysfunctions in respiratory motoneuron plasticity can be fatal. With respect to hypoxic conditions, hypoglossal motoneurons (HMs), which participate in a variety of upper airway behaviors, are considered critical for maintaining upper airway patency. Failure in these neurons can disfacilitate the tongue, rendering an obstruction in the upper airway. This can exacerbate hypoxic conditions, and may potentially contribute to sudden infant death syndrome (SIDS) and obstructive sleep apnea (OSA).

Serotonin (5-HT) affects HM excitability through a wide variety of mechanisms, and the density of 5-HT receptors has been shown to change during postnatal development. 5-HT is known to participate in the initiation of both short- and long-term hypoxic responses in the isolated HM, with repeated bouts of either hypoxia or 5-HT evoking a persistent increase in HM excitability known as long-term facilitation (LTF). In addition, 5-HT modulates intracellular Ca^{2+} levels, which regulate neural excitability through Ca^{2+}-gated-K^{+} channels.

Here, short-term, long-term, and intracellular Ca^{2+} responses to simulated hypoxic bouts are investigated via three developmentally distinct 5-HT sensitive HM computational models: neonatal (P3-P5), juvenile (P7-P12), and adult (>P21). Results from model simulations demonstrate that (1) the intracellular Ca^{2+} response to 5-HT is likely driven by two separate effects: a reduction in Ca^{2+} influx from the membrane and a concomitant release of Ca^{2+} from intracellular stores, (2) the 5-HT_{1A} receptor is implicated primarily in the short-term hypoxic response while the 5-HT_2 receptor plays a greater role in the long-term response, (3) LTF initiation is governed by PKC activation and maintenance derives from MAPK cascade bistability, and (4) the juvenile HM model exhibits a blunted capability to undergo LTF compared to the neonatal and adult HM models, which may play a role in age-specific pathologies. Finally, a mathematical reduction over these models is implemented to identify the fundamental requirements to derive such behavior in neural systems in general.

Table of Contents

List of Figures

List of Tables

List of Abbreviations

5-HT	Serotonin
5-HT_{1A}R	Serotonin 1A receptor
5-HT_{2}R	Serotonin 2 receptor
5-HTR	Serotonin receptor
AMPA	2-amino-3-(3-hydroxy-5-methyl-isoxazol-4-yl)propanoic acid
AMPAR	AMPA receptor
BK	Big-conductance calcium-gated-potassium channel
Ca^{2+}	Calcium
HM	Hypoglossal motoneuron
HVA	High-voltage activated
InsP3R	Inositol triphosphate receptor
IP3	Inositol triphosphate
ivLTF	In vitro LTF
K^{+}	Potassium
LTF	Long-Term Facilitation
LTP	Long-Term Potentiation
LVA	Low-voltage activated
MAPK	Mitogen activated protein kinase
MAPKK	Mitogen activated protein kinase kinase
MAPKKK	Mitogen activated protein kinase kinase kinase
Na^{+}	Sodium
NE	Norepinephrine
NMDA	N-Methyl-D-aspartic acid or N-Methyl-D-aspartate
nXII	Hypoglossal motor nucleus
OSA	Obstructive Sleep Apnea
PKC	Protein kinase C
PM	Phrenic Motoneuron
P*x*	Post-natal day *x* (eg: P3 = Post-natal day 3)
SIDS	Sudden Infant Death Syndrome
SK	Small-conductance calcium-gated-potassium channel
STF	Short-Term Facilitation
XII	Hypoglossal nerve / Cranial nerve 12

A. Introduction

Neuronal plasticity is a key facet of neurons throughout the central and peripheral nervous system. The ability to adapt to changing conditions is especially critical in respiratory motoneurons, where a failure to adapt to hypoxic conditions can result in death of the organism or hypoxic brain injury.

Hypoglossal motoneurons (HMs) participate in a variety of upper airway behaviors, including but not limited to breathing, swallowing, suckling, speech, and maintenance of upper airway patency. Thus, they are of particular interest since failure in these neurons can disfacilitate the tongue, leading to airway obstruction. This could potentially exacerbate hypoxic conditions, and therefore, may potentially contribute to sudden infant death syndrome (SIDS) and obstructive sleep apnea (OSA). An increase in HM excitability is a fundamental part of the hypoxic response, and a better understanding of this phenomenon could aid in the understanding of SIDS, OSA, and the hypoxic response with respect to the animal as a whole.

In HMs, neuronal plasticity, termed long-term facilitation (LTF), is quite distinct from Long-Term Potentiation (LTP) observed many other neurons; LTP is the more commonly-known and understood form of neuronal plasticity. HMs primarily rely on activation by serotonin (5-HT) and norepinephrine (NE) (Feldman et al 2005), but it remains unclear whether NMDA plays a formative role (Ling 2008) in LTF, as it does in LTP. HMs also exhibit lower Ca^{2+} buffering capabilities than other neurons (Lips & Keller 1998), which in turn may lead to more complex intracellular Ca^{2+} dynamics, and may play an important role in various behaviors exhibited during 5-HT application to these motoneurons.

5-HT, which originates from the raphe nucleus, provides an excitatory stimulus to HMs, constituting one of the many sources of excitatory drive. Hypoxic conditions generally produce elevated levels of presynaptic 5-HT release onto HMs. With application of intermittent pulses of 5-HT onto HMs, an initiation of LTF is observed. This experimental paradigm is suggested to be comparable to intermittent hypoxic challenges in the intact animal. In contrast, a single application of 5-HT elicits an immediate short-term increase in excitability of HMs that disappears rapidly after removal of 5-HT, and is referred to as short-term facilitation (STF). In general, STF is exhibited whenever 5-HT is applied while LTF only appears when the 5-HT stimulus is repetitive and properly patterned. An example of both STF and LTF in a biological preparation depicting hypoglossal nerve (XII) activity is shown in Figure 1A.

Intracellular Ca^{2+} can also be substantially elevated by 5-HT, with several mechanisms being described for this 5-HT-induced modulation of intracellular Ca^{2+}, including inhibition of voltage-gated Ca^{2+} channels (Grunnet et al 2004, Talley et al 1997). The specific underlying mechanisms for manifestation of LTF and STF, however, remain unknown. Paradoxically, while the overall intracellular concentration of Ca^{2+} is increased by 5-HT, the magnitude of individual Ca^{2+} spikes, each of which corresponds to a single HM burst, appears to be reduced (Figure 1B). Ca^{2+} plays a major role in setting firing frequency via small-conductance Ca^{2+}-gated K^+ (known as SK) channels; however, the cytosolic Ca^{2+} concentration depicted in Figure 1B is distinct from the Ca^{2+} detected by SK channels. Ca^{2+}-gated-K^+ channels detect changes in Ca^{2+} from

volumes proximal to the opening of voltage-gated-Ca^{2+} channels. Such volumes are called Ca^{2+} microdomains, which exist along the interior of the cell membrane directly beneath voltage-gated-Ca^{2+} channels. To accommodate these two spatially distinct pools of Ca^{2+}, our models include realistic intracellular Ca^{2+} determinations via a Ca^{2+} diffusion model, which separately tracks microdomain Ca^{2+} and cytosolic Ca^{2+}, and interfaces with 5-HT receptors appropriately to produce results that match published observations from Ca^{2+} fluorescence experiments. Additionally, conducting simulation experiments that correspond to the addition of various pharmacological blockers, we demonstrate that the influence of 5-HT on cytosolic and microdomain Ca^{2+} is multifaceted. Since intracellular Ca^{2+} is integrally tied to firing frequency, understanding how 5-HT modifies firing frequency in the short-term requires an understanding of numerous cellular behaviors, including the direct effects of 5-HT on intracellular Ca^{2+} levels, the effects of 5-HT on voltage-gated Ca^{2+} channels, and the effects of 5-HT on non-Ca^{2+} related processes.

The 5-HT neurotransmitter system also exhibits alterations during postnatal development, with numerous transient and permanent reductions in 5-HT receptor (5-HTR) subtype expression being observed roughly around P12; the most relevant examples are illustrated in Figure 2A-B. In addition to the changes in neurotransmitter receptor densities, developmental changes in electrophysiological properties of HMs have also been reported albeit these changes are seen roughly around P7-P12 (Figure 2C). As previously noted, 5-HT can elevate intracellular Ca^{2+}, and Ca^{2+}-gated-K^+ channels can exert a potent effect on HM firing frequency. Thus, many of the developmental changes can be considered coupled. Additional evidence for a special period during development is detailed in biological experiments from the Wong-Riley lab (Liu & Wong-Riley 2010b, Wong-Riley & Liu 2008), who refer to this period as a "respiratory critical period". The concept of a respiratory critical period, which is defined as a state of dramatic change in respiratory properties at both the cellular and organism level that alter the overall behavior of the system, is of particular relevance in the study of SIDS. The triple-risk model of SIDS (Filiano & Kinney 1994) states that SIDS may result from a confluence of three factors: an intrinsically vulnerable infant, a respiratory critical period, and exogenous respiratory stressors. Based on these studies, we posit that the electrophysiological and 5-HTR changes that occur around P7-P12 may be sufficient to generate such a critical period.

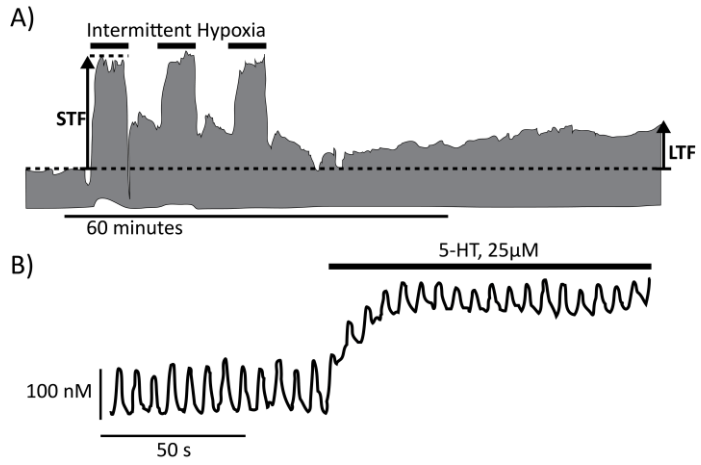

Figure 1: 5-HT Related HM Behaviors
Examples of behaviors exhibited by HMs in biological preparations. Shown here are A) hypoxia-induced STF and LTF in the XII nerve (adapted from Baker-Herman and Strey, 2011), and B) a rise in Ca^{2+} imaged from the soma of a HM during the application of 5-HT (adapted from Ladewig et al, 2004).

For this reason, we refine a known non-developmentally specific HM model (Purvis & Butera 2005) to match the properties of HMs at three developmentally distinct

age groups: neonatal (P3-P5), juvenile (P7-P12), and adult (>P21), where the juvenile age group represents the developmental period where a respiratory critical period would be expected. Each of these age categories is associated with distinct electrophysiological properties (Viana et al 1995) and differing postsynaptic concentrations of 5-HT receptors (Liu & Wong-Riley 2008, Liu & Wong-Riley 2010a), and for the current study, each age group is considered separately to facilitate our understanding of how development might change the capacity of the rat HM to respond to hypoxic challenges, and how HMs might be susceptible to disease at specific ages.

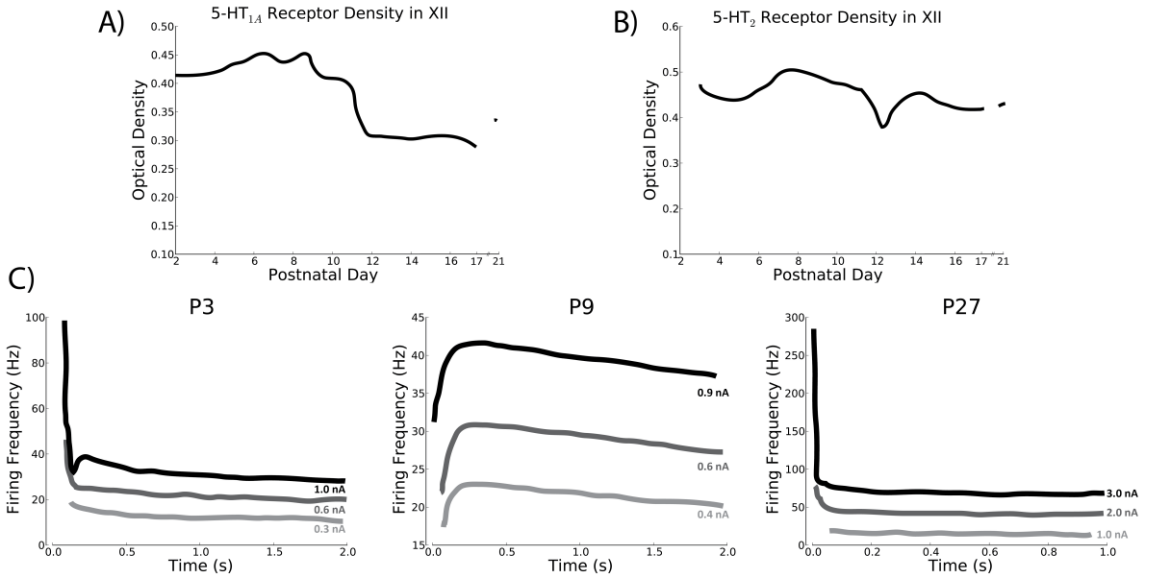

Figure 2: Known Developmental Changes From Biological Data.
Postnatal developmental changes that affect various serotonergic and electrophysiological aspects of the HM: A) dramatic statistically significant drop in 5-HT_{1A}R around P12 (adapted from Liu and Wong-Riley, 2010a), B) transient statistically significant drop in 5-HT_2R around P12 (adapted from Liu and Wong-Riley, 2008), and C) transient change from an adapting firing frequency to an accelerating one around P9 (adapted from Viana et al, 1995).

The goal of the current project is to ultimately investigate LTF in the HM, but because STF is a natural consequence of the application of 5-HT, any study of LTF would necessitate an investigation of STF. Protein Kinase C (PKC) has been implicated in the initiation of LTF (Neverova et al 2007); therefore, we modify our HM models to include a PKC pathway. We also include a MAPK cascade model, as MAPK has been suggested as a potential player in LTF (Fuller et al 2000). Moreover, both PCK and MAPK are presumed to work through modifications to AMPAR conductance, with MAPK being presumed to increase the production of AMPAR receptors and PKC implicated in direct phosphorylation of AMPAR (Boehm et al 2006, Chung et al 2000). In order to include AMPAR-mediated effects, we further extend our HM models to include AMPAR production and insertion, and evaluate the influence of 5-HT-related Ca^{2+} and AMPAR effects on STF. For these simulation experiments, we again leverage a variety of simulated pharmacological agents in an attempt to associate specific 5-HTR subtype-mediated effects with specific STF behaviors, and find that these relatively simple pharmacological manipulations clearly identify the intrinsic cellular signaling processes responsible for the 5-HT-induced HM modifications under a single hypoxic challenge. While there are good reasons to believe that 5-HT-mediated-LTF is a

byproduct of changes in postsynaptic HM AMPAR density, it is not entirely clear from the literature how it might differ, if at all, from AMPAR-related effects on STF. Subsequently, we find that the mechanisms involved in LTF differ from those of STF, and that these differences manifest themselves through distinct 5-HTR subtypes. Furthermore, we find that there are distinct portions of the model responsible for the initiation versus the maintenance of LTF, and that LTF can be recovered in models where it did not previously appear based on several experiments using simulated pharmacological manipulations.

Respiratory LTF can be expressed as either an increase in burst amplitude (Baker-Herman & Mitchell 2008, McKay et al 2004) or a combination of increased burst amplitude and frequency (Bach & Mitchell 1996, Baker & Mitchell 2000). Because LTF has been observed in the isolated HM with 5-HT application (Feldman et al 2005), termed in vitro LTF (ivLTF), we opt to restrict our model to a single HM. In doing so, however, it should be noted that several distinctions arise between our models and biological data. In our models, measurement of LTF is based on firing frequency, most notably peak firing frequency within each HM burst. In comparison to the entire nXII, an increase in firing frequency of all neurons within this motor nucleus would result in an increase in voltage amplitude, as the action potentials from every neuron contribute to a stronger overall nXII response. In comparison, because our models will be driven by a steady rhythmic presynaptic glutamatergic input, which will remain unaffected by changes in the HM itself, our model is incapable of exhibiting frequency-based LTF without the addition of more detailed presynaptic mechanisms.

With a thorough understanding of a complex dynamical system comes the capacity to produce reduced and minimal models that mimic the behavior of their more complicated versions. Here, we generate reduced models for the two aforementioned mechanisms documented in the literature: intracellular Ca^{2+} changes and LTF. We did not specifically generate a reduced model for STF at this time because STF behavior implicitly appears in our reduced LTF model. The reduced models demonstrate that while hundreds of differential equations are used in the full HM models discussed above, they are not strictly necessary to produce the desired behavioral outcomes. It should be noted, however, that such reduced models offer fewer opportunities for simulated pharmacological manipulations, and generally only exhibit the behaviors verified to exist in the full models. Such models are also critically important for future studies transitioning the single HM LTF model into a nXII LTF network model. Furthermore, these reduced models highlight how similar behaviors can arise in other biological systems under otherwise distinct circumstances, and illuminate that some otherwise unique effects are necessary to produce LTF.

By investigating all of these various properties of 5-HT on the HM, and its role in Ca^{2+}, STF, and LTF, we can come to a clearer understanding of how this neurotransmitter can modify the HM response to both short-term and long-term hypoxic insults as well as provide insight into both developmental regulation and disease states exhibited by this motoneuron.

A1. Known and Unknown Aspects

Known and unknown aspects of the HM response to 5-HT and to hypoxia from the previous section are summarized below. Additionally, pertinent questions related to aspects not fully understood are provided below.

Known Aspects

- At the single HM level, hypoxic responses (STF, LTF) can be observed after application of 5-HT (Feldman et al 2005).
- Overall cytosolic Ca^{2+} rises during 5-HT application (Ladewig et al 2004).
- HMs contain Ca^{2+}-gated-K^{+} channels (Viana et al 1993).
- PKC is involved in initiation of LTF (Neverova et al 2007).
- PKC is not involved in the maintenance of LTF (Fuller et al 2001).
- PKC can phosphorylate AMPAR (Boehm et al 2006, Chung et al 2000).

Unknown Aspects

- The mechanism(s) of maintenance for LTF.
- Whether PKC initiates LTF directly via AMPAR phosphorylation or indirectly through other pathways, or both.
- The exact mechanism(s) governing the rise in cytosolic Ca^{2+} during 5-HT application.
- The role of different 5-HTR subtypes.
- The role of intracellular Ca^{2+} with respect to excitability during 5-HT application.
- The role of development on hypoxic responses.

Major Questions

- Why does cytosolic Ca^{2+} increase dramatically with 5-HT application?
- Why do cytosolic Ca^{2+} spikes change in size during 5-HT application?
- 5-HT is responsible for STF, but are there receptor subtype differences?
- Does LTF change over postnatal development? Is there a “critical period” where LTF vanishes?
- PKC is implicated in LTF initiation, but not in maintenance. What maintains LTF?
- Are the underlying dynamics exhibited by LTF in the HM applicable to understanding the dynamics of other neural systems?

A2. Specific Aims

To address the questions posed in the previous section, a number of specific aims have been posed to evaluate the underlying mechanisms mediating the changes in cytosolic Ca^{2+}, STF, and LTF, and to make predictions about the stability of LTF through development. Since the response to hypoxia is complex and 5-HT plays a major role in many aspects of the electrophysiological, Ca^{2+}-related, and secondary messenger aspects of this response, the primary questions are grouped together into four themed aims. Each aim, as appropriate, includes a hypothesis to be directly tested, alternate explanations that

must be ruled out as part of confirming the hypothesis, and the simulations run to test the hypothesis and alternate explanations. Further details on the simulations can be found in the Methods section.

1. In HMs, cytosolic intracellular Ca^{2+} ($[Ca^{2+}]_{c1}$) exhibits two distinct changes with the application of 5-HT: a slow increase in baseline Ca^{2+} (low-frequency change) and an increase in the peak of the Ca^{2+} spikes with each burst (high-frequency change)

1a. Cytosolic intracellular Ca^{2+} exhibits a slow increase in baseline Ca^{2+} with the application of 5-HT in biological experiments.

Hypothesis: The slow increase in cytosolic intracellular Ca^{2+} is hypothesized to be driven by InsP3R-mediated release of Ca^{2+} from intracellular stores via secondary messenger cascades beginning with 5-HT_2R activation.

Alternate Explanation: An increase in firing frequency could increase cytosolic intracellular Ca^{2+} in the Ca^{2+} microdomains via voltage-gated Ca^{2+} channels. This Ca^{2+} influx, in turn, could diffuse into the cytosol from the membrane. Such increases would be expected with increased AMPAR conductance.

1b. Cytosolic intracellular Ca^{2+} exhibits an increase in the peak of Ca^{2+} spikes with each burst with the application of 5-HT.

Hypothesis: The increase in cytosolic intracellular Ca^{2+} is hypothesized to be driven by 5-HTR_{1A}R inhibition of high-voltage activated (HVA) Ca^{2+} channels, which in turn would reduce microdomain Ca^{2+}, and the magnitude of the Ca^{2+} spikes, diffusing into the cytosol from the membrane.

Alternate Explanation: An increase in cytosolic Ca^{2+} could result in a diffusion of cytosolic Ca^{2+} into the microdomains. This, in turn, could activate SK channels, which would inhibit voltage-gated Ca^{2+} channels, and reduce microdomain Ca^{2+}. An initial rise in cytosolic Ca^{2+} could come from InsP3R-mediated Ca^{2+} release.

Simulations:

- Blockade of 5-HT_2R to eliminate InsP3R-mediated Ca^{2+} release and AMPAR-related effects.
- Blockade of InsP3R to eliminate InsP3R-mediated Ca^{2+} release alone.
- Blockade of 5-HTR_{1A}R to eliminate inhibition of HVA Ca^{2+} channels.

2. STF appears rapidly after the application of 5-HT in biological experiments, and persists until 5-HT is removed. Additionally, the return to baseline excitability is far slower than its initial rise, implicating an additional potential mechanism for short-term sustainment of at least part of the STF response.

2a. STF appears rapidly following 5-HT application in biological experiments.

Hypothesis: Since one of the most rapid serotonergic effects is 5-HT_{1A}R inhibition of Ca^{2+} channels, which would subsequently inhibit SK channels, it is hypothesized that the majority of the STF response results from 5-HT_{1A}R activation while other changes in excitability play less of a role in STF.

Alternate Explanation: Phosphorylation of AMPAR by PKC increases their insertion rate into the membrane, which in turn, would increase excitability.

2b. A portion of the STF response persists transiently even after the removal of 5-HT.

Hypothesis: Since the trafficking of AMPAR is relatively rapid but not necessarily instantaneous, it is hypothesized that the phosphorylation of AMPAR via PKC is responsible for the transient potentiation.

Alternate Explanation: InsP3R-mediated Ca^{2+} release from extracellular stores increases the levels of Ca^{2+} exposure to pumps and exchangers, resulting in an overall net reduction of Ca^{2+} within the cell, and subsequent inhibition of SK channels.

Simulations:

- Blockade of 5-HTR$_{1A}$R to eliminate inhibition of HVA Ca^{2+} channels.
- Blockade of 5-HT_2R to eliminate InsP3R-mediated Ca^{2+} release and any AMPAR-related effects.
- Blockade of InsP3R to eliminate InsP3R-mediated Ca^{2+} release alone.
- Blockade of PKC to eliminate AMPAR-related effects alone.

3. LTF only appears after intermittent applications of 5-HT. Whether known changes during development produce a critical period remains an open question. Additionally, although PKC appears to be required for the initiation of LTF, the mechanisms underlying its maintenance are less well understood.

3a. Developmentally-related changes may be transiently disruptive to LTF.

Hypothesis: A decrease in 5-HT_2R density may dramatically weaken AMPAR-related potentiation, which in turn may disrupt LTF. The natural decline in 5-HT_2R density around P7-P12 may result in a developmental-specific loss of LTF.

Simulations:

- Produce HM models based on biological data for HM behavior before, during, and after the hypothesized P7-P12 respiratory critical period.

3b. PKC is required for initiation of LTF, but mechanisms for maintenance of LTF have not been identified.

Hypothesis: Maintenance of LTF results from activation of MAPK cascade cellular signaling, leading to AMPAR upregulation in the cell.

Alternate Explanation: InsP3R-mediated release of Ca^{2+} from extracellular stores increases the levels of Ca^{2+} exposure to pumps and exchangers, resulting in an overall net reduction of Ca^{2+} within the cell, and subsequent inhibition of SK channels and an increase in excitability until Ca^{2+} levels are restored.

Simulations:

- Simulated block of PKC before initiation, after initiation, and both before and after initiation.
- Simulated block of MAPK before initiation, after initiation, and both before and after initiation.

In addition, as part of our explorations of LTF, we have generated a series of reduced models of varying scope based on our full HM model. These models lend insight into the underlying mechanisms of LTF, and may be applicable to similar related processes:

4. By combining a series of reduced models, we produce a reduced model of LTF that incorporates simplified systems for spike generation, secondary messenger systems, and AMPAR upregulation. While no hypothesis is specifically tied to this aim, we remark that such a model is far better suited for use in network models than the far more computationally intensive full model. In addition, reduced models lend insight into underlying mechanisms and dynamics driving LTF that may otherwise be obscured by the complexity of full models.

B. Background & Significance

B1. Neural Control of Respiration

Gas exchange in all living organisms helps to maintain proper pH and provides oxygen, which is necessary for organisms that undergo aerobic respiration. Active pumping of gases is important for animals with high metabolic rates, particularly in warm-blooded mammals and birds (Feldman & McCrimmon 2008, Feldman et al 2003). The neurons involved in respiration, including those that generate the respiratory rhythm, innervate respiration-associated muscles, and sense blood gasses, are all located in the medulla and pons (Abdala et al 2009, Duffin 2004, Feldman et al 2003). These regions also play roles in a variety of other behaviors, including coughing, sneezing, swallowing, spitting, sighing, and vomiting.

The precise location and organization of the respiratory rhythm generator is currently a matter of open inquiry. At present, it is believed that the preBötzinger Complex (preBötC) is either the primary area of respiratory rhythm generation (Gray et al 2001) or is the main inspiratory rhythm generator, with the retrotrapezoid nucleus (RTN) being the main expiratory rhythm generator (Feldman & Del Negro 2006, Janczewski & Feldman 2006). The RTN and the parafacial respiratory group (pFRG),

another region implicated in respiratory rhythm generation (Onimaru & Homma 2003), may be functionally and anatomically part of one larger region, and so are often referred to together as the RTN/pFRG. The preBötC is located in the most rostral part of the ventral respiratory group (VRG), and just caudal to the Bötzinger Complex (BötC). Both the preBötC and the RTN/pFRG are located in the rostral half of the ventral respiratory column (VRC) (Feldman & McCrimmon 2008, Moss 2005). Modeling efforts have extended to simulations of preBötC bursting pacemaker cells, involving models of both isolated and synaptically coupled cells (Butera et al 1999a, Butera et al 1999b, Del Negro et al 2001) as well as synaptically coupled intrinsically bursting cells attached to an inhibitory network (Smith et al 2000). Models of the VRG involving the spike train generator model SYSTM11 (MacGregor 1987) have also been constructed to study cough (Shannon et al 2000, Shannon et al 1998).

The modern study of respiratory circuitry is mostly performed on rodents. Several preparations in particular are commonly used to study either adult or neonatal respiratory neurons. For neonates, there are two main preparations, both of which are *in vitro*: the medullary slice and the *en bloc* preparations. In the medullary slice preparation, a coronal or sagittal slice containing the preBötC is taken from the neonatal rodent. Electrophysiological recordings are then typically taken from the preBötC, the XII nerve, and various other nuclei (Smith et al 1991). The *en bloc* preparation involves maintaining an isolated intact brainstem and spinal cord, transected either at the most rostral end of the pons or at the pontomedullary junction, and removed from the body (Brockhaus et al 1993). Unlike the medullary slice, an *en bloc* preparation maintains the complex synaptic connections and dendritic trees of all the neurons under study, but likewise suffers from greater difficulty in keeping the tissue properly oxygenated (Richter & Spyer 2001). For adults, there are also two main preparations: *in situ* and *in vivo*. The *in situ* preparation, also called the arterially-perfused rodent (*a.k.a.*, working heart-brainstem) preparation, involves a bisection below the diaphragm, precollicular decerebration, and removal of skin and forepaws of limbs (Paton 1996). Following this, the rodent is perfused with artificial cerebrospinal fluid that contains an oncotic agent to minimize tissue edema, and electrophysiological recordings are taken from the exposed brainstem. *In vivo* preparations typically involve recording from alive, anesthetized or decerebrate animals that are intubated and artificially ventilated with oxygen-rich air (Koshiya & Guyenet 1996, Paton & Richter 1995). It should be noted that anesthetic can affect respiratory neuron electrophysiological properties (Richter & Spyer 2001), and so *in vivo* anesthetized preparations may not necessarily be superior to the *en bloc* preparation, which lacks anesthesia at the time of recording.

Because of differences in both maturity and synaptic isolation between adult and neonate preparations, several distinctions arise. Neonatal neurons have less developed dendritic trees than adult neurons, and this can impart conduction delays to some signals. More gap junctions tend to be present in neonates, and so more regular bursting is observed. The physical elimination of synaptic drives from respiratory afferents and other parts of the nervous system in neonatal preparations can reduce excitability significantly, which may require alterations such as increasing extracellular K^+ concentration, which no longer reflects regular cellular conditions (Richter & Spyer 2001). While no preparation is perfect, each one yields important insight on respiration from a unique perspective.

The act of breathing itself has two major phases: inspiration and expiration, where expiration is often then broken down into two sub-phases: E1 and E2. These phases are driven by the respiratory rhythm generators, which ultimately drive respiratory motoneurons (Feldman & McCrimmon 2008). These motoneurons enact the physiological changes necessary for drawing air into and out of the lungs.

B2. Respiratory Motoneurons

Respiratory motoneurons can be classified into two major groups: pump motoneurons that mostly exist in the spinal cord and drive air in and out of the lungs, and resistance motoneurons that mostly reside in brainstem cranial nuclei and modulate airway resistance (Moss 2005).

Pump motoneurons predominantly include the phrenic (located at vertebrae C_3-C_5), intercostal (at T_1-T_{12}), and abdominal motoneurons (at T_4-L_3), which innervate the diaphragm, intercostal muscles, and abdominal muscles, respectively (Bianchi et al 1995, Feldman et al 1985, Furusawa et al 1991). Because the diaphragm is the primary inspiratory muscle, it is the most frequently motor output recorded in animal models, except the medullary slice preparation, which does not contain the spinal cord. In this preparation, hypoglossal motoneurons/nerves are typically recorded from instead.

Resistance motoneurons consist of the hypoglossal, glossopharyngeal, and vagal motoneurons. Unlike pump motoneurons, resistance motoneurons often project to a number of targets. Hypoglossal motoneurons (HMs) innervate various tongue muscles, including the styloglossus, hyoglossus, and genioglossus (Topert et al 1998), which elevate and withdraw the tongue, depress the tongue, and protrude the tongue, respectively (Bass & Morrell 1997, Fregosi & Fuller 1997, Gilliam & Goldberg 1995, Kristensson & Olsson 1971). Glossopharyngeal (IX) motoneurons predominantly innervate the stylopharyngeus, which elevates both the larynx and pharynx (Barsh 1999, Bass & Morrell 1997). The vagus nerve branches repeatedly, and the pharyngeal plexus (PhX), superior laryngeal nerve (SLN), and recurrent laryngeal nerve (RLN) branches innervate respiratory muscles. The pharyngeal branch innervates many muscles of the pharynx: the palatopharyngeus, hyopharyngeus, thyropharyngeus, and the semicircular muscle. The RLN innervates most of the larynx, including the cricovocal and cricoarytenoid muscles, whereas the SLN only innervates one laryngeal muscle: the circothyroid muscle, along with esophageal muscles, and the semicircular muscle (Kobler et al 1994).

In general cranial and spinal neurons are considered to contain somatotopic organization (Rekling et al 2000), and this has been specifically confirmed for the phrenic nerve (Mosfeldt Laursen & Rekling 1989) and hypoglossal nerve (Karschin et al 1996, Topert et al 1998).

The pump and resistance motoneurons must coordinate their activities to ensure proper airflow through the respiratory system, as air cannot flow without being pumped, nor can it flow if the upper airway is closed. This coordination is reflected in the near-synchronization seen between phrenic motoneurons (PMs) and HMs. However, despite this coordination, HMs begin firing in the pre-inspiratory phase, just prior to when PMs begin firing at the start of the inspiratory phase. HMs can also activate independently of PMs during swallowing (Jean 2001). These findings imply that though PMs and HMs

typically fire almost concurrently, they may be driven partly or wholly by different rhythmic signals and cues (Saito et al 2002).

B3. Projections to Respiratory Motoneurons

Spinal and cranial motoneurons are both driven and modulated by a variety of other medullary and pontine nuclei. Projections releasing glutamate, GABA, and glycine act directly on motoneurons via ionotropic receptors, and help drive and control the precise timing of motoneuron firing. Projections releasing amines (such as serotonin), peptides, and other neurotransmitters acting on metabotropic receptors facilitate long-term changes to excitability with sleep, hypoxia, exercise, and various other behaviors (Henry & Manaker 1998, Kinney et al 2007, Rekling et al 2000).

Both the nXII and spinal motor nuclei receive projections from the locus coeruleus (LC) and nucleus subceruleus (nSC), pontine respiratory group, reticular formation, and neurons in and around the DRG as well as indirect drive from various rhythmogenic parts of the VRC.

The LC and the nSC have a multitude of wide-spanning norepinephrine (NE) projections that have been associated with alertness, and are known to be involved in responses to hypoxia (Breen et al 1997, Nygren & Olson 1977). These two nuclei send projections ubiquitously throughout the spinal cord (Holstege & Kuypers 1987) whereas only the nSC projects to nXII neurons innervating protrusion muscles via excitatory synapses (Aldes 1990). LC and nSC projections to spinal and cranial nuclei are excitatory and NEergic (Aldes 1990, Aldes et al 1992, Holstege & Kuypers 1987, Nygren & Olson 1977). The nXII may also receive NE input from other regions in the pons (Aldes et al 1992).

The reticular formation has been implicated in a variety of autonomic behaviors, such as respiration, cardiovascular regulation, habituation to stimuli, and sleep (Bourgin et al 1995, Lingenhohl & Friauf 1994, Schulz et al 1983). Reticular formation projections come to the nXII mainly from the caudal medullary intermediate reticular region (IRt) (Volgin et al 2008) and the lateral reticular formation, particularly from the nucleus reticularis parvocellularis (RPc), with fewer projections coming from the nucleus reticularis gigantocellularis (RGc) and the nucleus reticularis ventralis (RV) (Borke et al 1983). Projections to the lumbar spinal cord, however, come from the ventromedial reticular formation (Holstege 1991). Projections to both cranial and spinal neurons predominantly carry GABA and glycine (Holstege 1991, Li et al 1997), except for IRt projections to the nXII, which comprise a significant glutamatergic input, and potentially a smaller cholinergic input as well (Volgin et al 2008).

The NTS envelops the solitary tract, and is involved in a host of behaviors including swallowing, sensation in the larynx and pharynx, baroreception, and various other gastric functions (Hornby 2001). The ventrolateral subnucleus of the NTS (vl-NTS) itself contains the DRG, which receives input from chemoreceptors and lung stretch receptors, and is thought to be critical to maintaining the respiratory rhythm (Moss 2005). These vl-NTS neurons project to the nXII (Ono et al 1994) and phrenic motor nucleus (Rikard-Bell et al 1984), as do other subsets of NTS neurons project to the (nXII projecting, Borke et al 1983; PMN projecting (Rekling et al 2000).

The caudal raphe nuclei send projections with 5-HT, substance P, and enkephalin (Enk) to the nXII (Chan-Palay et al 1978, Connaughton et al 1986, Henry & Manaker 1998, Manaker & Tischler 1993), and various parts of the raphe nuclei send 5-HT, substance P, Enk, glutamate, aspartate, and TRH to the spinal cord (Bowker et al 1983, Holstege & Kuypers 1987, Nicholas et al 1992). In both projections to the nXII and to the spinal cord, 5-HT and substance P are often colocalized (Chan-Palay et al 1978, Nicholas et al 1992). The raphe nuclei also have 5-HT, substance P, and methionine-enkephalin (Met-Enk) projections to the facial (nVII) and trigeminal (nV) nuclei (Rekling et al 2000).

Since both the nXII and PMs discharge with inspiration, it is not surprising that they receive input from the VRG, either directly or indirectly. Though the preBötC does not project directly to the nXII or appreciably to PMs, there is a population of premotoneurons ventrolateral to the nXII that receive synapses from the preBötC, and then subsequently synapse onto the nXII (Koizumi et al 2008). PMs receive excitatory input from the rVRG, an area implicated in inspiratory drive (Dobbins & Feldman 1994), and inhibitory input from the Bötzinger complex, an area implicated in expiratory drive (Fenik et al 2005). The nXII, on the other hand, is excited by inputs during the inspiration phase, predominantly by glutamatergic input (Volgin et al 2008), but is disfacilitated in the expiratory phase (Peever et al 2002). Feldman and Janczewski, however, hypothesize that the nXII may receive inhibitory expiratory drive from the RTN/pFRG (Feldman & Janczewski 2006).

Both nXII and PMs share some, but not all premotor input (Ono et al 1994), which is not surprising, as the nXII and PM fire mostly concurrently, but can be decoupled in their activity (St-John et al 2004). The nXII also receives input from other medullary and pontine nuclei that do not project to PMs, like the trigeminal nucleus and the pontine tegmentum.

The spinal trigeminal nuclei receive pain and somatosensory afferents from the face (Henry et al 2008, Upadhyay et al 2008). The spinal trigeminal pars oralis (SpVO) and interpolaris (SpVI) have GABA and glycine projections into the nXII ipsalaterally (Borke et al 1983, Li et al 1997)

The pedunculopontine tegmental (PPT) nucleus and the laterodorsal tegmental (LDT) nucleus of the pontine tegmentum, which are particularly active during wakefulness and REM, have cholinergic synapses with the nXII (Rukhadze & Kubin 2007). Acetylcholine itself has an unusual modulatory effect on HMs, as activation of nicotinic acetylcholine receptors increase excitability while activation of muscarinic acetylcholine receptors decreases excitability (Bellingham & Berger 1996, Liu et al 2005). The overall effect of acetylcholine, however, is generally inhibitory.

B4. Motoneuron Electrophysiology

Electrophysiologically, both spinal and cranial motoneurons in isolation share a variety of similar properties due to similarities in ion channel content. Channels can be classified by the ion they gate and the conditions that activate them. For voltage-gated channels, motoneurons express sodium, potassium, and calcium channels. For ion-activated channels, motoneurons express Ca^{2+}-activated K^+ channels, Ca^{2+}-activated Na^+

channels, and K^+-activated Na^+ channels. Motoneurons also express a variety of leak channels. Additional details describing the individual ion channel types expressed in motoneurons are summarized below:

For voltage-gated Na^+ channels, all motoneurons express fast inactivating Na_T channels to drive their action potentials. Persistent Na_P channels, which amplify excitatory membrane responses, are also expressed in HMs (Mosfeldt Laursen & Rekling 1989) and in spinal motoneurons, Na_P channel currents are known to be enhanced by 5-HT (Harvey et al 2006). Na_P channels are also known to play a role in plateau potential in spinal motoneurons, particularly after injury (Li & Bennett 2003).

Voltage-gated K^+ channels are critical for repolarization following an action potential, maintenance of the resting potential, and modulating firing frequency (McLarnon 1995). Inward recitfying K_{ir} channels are expressed in motoneurons, and $K_{ir}2.2$, $K_{ir}3.2$, $K_{ir}3.3$, and $K_{ir}3.4$ proteins are specifically known to reside in HMs (Karschin et al 1996), along with $K_{ir}2.4$, which is not seen anywhere else in the nervous system (Topert et al 1998). K_{ir} channels also exist in spinal motoneurons (Takahashi 1990a). Both delayed rectifier K_{dr} channels and rapidly inactivating A-current channels are also known to exist in spinal neurons (Takahashi 1990b) and HMs (Haddad et al 1990, Lape & Nistri 1999). The A-current may also activate at lower voltages in the presence of NE (Parkis et al 1995).

For voltage-gated Ca^{2+} channels, two varieties exist: low-voltage activated (LVA) and high-voltage activated (HVA), and both types are responsible for the post-spike afterdepolarization (ADP) that is seen in some motoneurons just after the spike. PMs (Martin-Caraballo & Greer 2001) and HMs (Powers & Binder 2003, Umemiya & Berger 1994, Umemiya & Berger 1995) contain the LVA T-channel and the HVA L-, N-, and P-channels, and therefore share a unique spike shape when recorded in synaptic isolation. Ca^{2+} channels are also a major source of modulation, where glutamate (acting on metabotropic receptors) reduces HVA currents in trigeminal MNs; however, modulatory effects of adenosine and 5-HT are not always consistent across MNs. For example, adenosine enhances HVA currents in vagal MNs (Marks et al 1993) but decreases them in spinal MNs (Mynlieff & Beam 1994) while 5-HT inhibits N- and P-channels in HMs (Bayliss et al 1995) but enhances LVA and HVA channels in spinal MNs (Berger & Takahashi 1990, Hounsgaard & Kiehn 1989). L-type Ca^{2+} channels, much like Na_P channels, have also been implicated in plateau potentials (Li & Bennett 2003).

Ca^{2+}-activated K^+ channels are the primary contributor to the afterhyperpolarization (AHP) following each spike in many motoneurons (often called the medium-duration afterhyperpolarization; mAHP), and therefore play a formative role in spike frequency modulation (Rekling et al 2000). There are two varieties of Ca^{2+}-activated K^+ channels: small voltage SK-channels, and big voltage BK-channels. SK-channels are not voltage-gated at all, only open in the presence of Ca^{2+}, are sensitive to apamin (Lape & Nistri 2000, Xia et al 1998), and are inhibited either directly or indirectly by 5-HT_{1A}R activation (Grunnet et al 2004, Talley et al 1997). BK-channels are both voltage- and calcium-activated (Schreiber & Salkoff 1997), and tend to open and close more rapidly than SK-channels. Both types of Ca^{2+}-activated K^+ channels have been previously modeled (Engel et al 1999). NE may also have a mild inhibitory effect on these channels (Parkis et al 1995).

Ca^{2+}-activated Na^+ channels are present in neurons that innervate the esophagus, and result in prolonged firing from short stimulations due to the slow clearance of Ca^{2+} (Rekling et al 2000), but otherwise have not been found to be expressed in any other neurons.

Na^+-activated K^+ channels induce a hyperpolarization that manifests after long spike trains, but otherwise do not strongly influence individual spikes. They can be found on spinal motoneurons (Safronov & Vogel 1996).

Leak channels come in a variety of forms and play important roles in setting the resting membrane potential. Of the main leak channels identified in motoneurons, K^+, Cl^-, and Na^+ leak channels are expressed, along with the hyperpolarization-activated inward current I_h, which technically is not a leak current but is often open at the resting membrane potential, and therefore behaves as a leak current. I_h gates Na^+ and K^+ ions, and can be found in HMs (Bayliss et al 1994a) and PMs (Di Pasquale et al 2001). The I_h current is also enhanced by 5-HT in trigeminal, facial, and spinal MNs (Hsiao et al 1997, Larkman & Kelly 1997), and reduced by NE (Parkis & Berger 1997) and 5-HT_2R activation (Xu et al 2009) in HMs. The K^+ leak channel is also a common target of neurotransmitter modulation, receiving inhibition from TRH in HMs and spinal MNs (Bayliss et al 1994b, Fisher & Nistri 1993, Rekling 1990), glutamate (on metabotropic receptors) in trigeminal MNs and PMs (Del Negro & Chandler 1998, Dong et al 1996), substance P in spinal MNs (Fisher & Nistri 1993), 5-HT in trigeminal and facial MNs (Hsiao et al 1997, Larkman & Kelly 1998), and NE in HMs, where the mechanisms underlying K^+ leak modification in HMs under TRH and NE application are thought to be related (Parkis et al 1995). A pH sensitive K^+ leak channel family, the TASK channels, are also present in HMs (Berg et al 2004), and these channels can be inhibited by 5-HT, NE, and substance P (Talley et al 2000, Xu et al 2009).

Electrophysiologically-based Hodgkin-Huxley like models of respiratory motoneurons have been constructed from biological data for synaptically isolated PMs (Amini et al 2004) and neonatal HMs (Purvis & Butera 2005). The PM model simulates behavior during normal conditions, TEA application, block of Ca^{2+}-gated K^+ channels, and block of Ca^{2+} channels. The HM model simulates behavior during normal and apamin block conditions, and has been subsequently extended to include secondary messenger systems related to intracellular Ca^{2+} concentration (Tsao & Butera 2008).

B5. Developmental Changes to Hypoglossal MNs

Throughout postnatal development, HMs exhibit a variety of changes that include alterations in electrophysiological properties, neuroanatomical structures, and neurotransmitter/neuromodulator systems. Many of the changes in electrophysiological properties are associated with the ion channels described above; however, changes associated with metabotropic ligand-gated ion channels are also manifest. Well-documented developmentally-regulated electrophysiological changes include differences in spike shape, adaptation changes vs input current, membrane resistance, and rheobase (Viana et al 1995). Additionally, a tenfold increase in I_h in adult HMs (Bayliss et al 1994a), a decrease in I_T shortly after birth (Umemiya & Berger 1994), and a shift in HVA Ca^{2+} current composition (Miles et al 2004, Umemiya & Berger 1994) have also been

reported. Developmentally-regulated neuroanatomical alterations include changes in the span of dendritic tress, the number of dendritic branches, branch order of dendritic trees, and dendrite diameter (Núñez-Abades & Cameron 1995, Nunez-Abades et al 1994). Developmentally-regulated changes in 5-HTR membrane density for various receptor subtypes has also been described (Liu & Wong-Riley 2008, Liu & Wong-Riley 2010a). Other plausible but unconfirmed developmentally-regulated changes include modifications to Ca^{2+} ion channel trans-membrane protein composition (McEnery et al 1998), changes to BK-channel membrane density (where they definitively exist in the adult (Pedarzani et al 2000)), and changes in buffer proteins (Tsai et al 1997).

Since firing frequency can be dramatically altered by changes in intracellular Ca^{2+}, changes in LVA and HVA Ca^{2+} channels are of particular interest. LVA currents comprise about 33% of neonatal Ca^{2+} currents and 15% of both juvenile and adult Ca^{2+} currents (Umemiya & Berger 1994), and the known changes in HVA channel composition in neonatal HMs are described in the table below:

Paper	P/Q-type	N-type	L-type	R-type
Miles et al (2004)	43%	11%	0%	46%
Umemiya and Berger (1994)	50%	29%	6%	15%

P/Q-type Ca^{2+} channels are sensitive to ω-agatoxin, N-type Ca^{2+} channels are sensitive to ω-conotoxin, Ca^{2+} L-type channels are sensitive to 1,4-dihydropyridine, and R-type Ca^{2+} channels are merely resistant to the three aforementioned blockers. Since each of these Ca^{2+} channel blockers may not completely block every single ion channel, the percentages indicated likely overestimate R-type Ca^{2+} current composition and underestimate the other Ca^{2+} current types. Furthermore, the R-type current is poorly understood, and therefore, it was omitted from the original Purvis and Butera (2005) model; in our models, this current is divvied up between the P/Q and N-type currents. As in the Purvis and Butera (2005) model, we conclude that the L-type current is sufficiently small to discard from our model.

B6. Intracellular Calcium, Buffering, and Secondary Messenger Interactions

Ca^{2+} plays a crucial role in both secondary messenger pathways and electrical excitability. Ca^{2+} first enters the membrane through voltage-gated Ca^{2+} channels, and is removed through various pumps, exchangers, and leak currents. Ca^{2+} also diffuses inward, where it is rapidly buffered and stored.

While voltage-gated Ca^{2+} channels have already been discussed in terms of electrophysiological properties in Section C4, it should be noted that these channels also play a crucial role for microdomain Ca^{2+}. The microdomain is oftentimes a space no more than 0.5μm in diameter just below voltage-gated ion channels (Sugimori et al 1994) although compelx microdomains also exist where many voltage-gated Ca^{2+} channels are tightly flanked by Ca^{2+} storing endoplasmic reticulum (Sugimori et al 1994). Approximately 5-10% of the space just beneath the membrane is considered part of the Ca^{2+} microdomain (Sugimori et al 1994), suggesting that Ca^{2+} is spatially localized

within the cell, even prior to sequestration within the endoplasmic or sarcoplasmic reticulum. Microdomain Ca^{2+} is involved in gating various Ca^{2+}-gated ion channels, such as BK and SK channels mentioned in Section C4. Ca^{2+} itself may also directly activate cyclic AMP, and therefore it can act on cell signaling cascades without an intermediary (Mons et al 1998).

The endoplasmic reticulum contains two distinct receptors serving as ion channels for the release of Ca^{2+}: inositol triphosphate receptors (IP_3R/InsP3R) and ryanodine receptors (RYR). IP_3R is a ligand gated ion channel, being activated by IP_3, a byproduct released by the cleavage of phosphatidylinositol 4,5-bisphosphate (PIP_2) by phospholipase C (PLC) after G-protein coupled receptor activation. RYR receptors, on the other hand, are Ca^{2+}-gated Ca^{2+} channels, and are particularly important in excitation-contraction coupling in muscle fibers (Panigrahy et al 2000). In addition to playing a role in microdomain and cytosolic Ca^{2+} concentrations, release of Ca^{2+} from IP_3R and RYR has been directly implicated in synaptic vesicle release (Berridge 1987). Ca^{2+} can also be sequestered in mitochondria, where both mitochondria and sarcoplasmic reticulum play a role in excitation-contraction coupling in heart and skeletal muscle (Han & Bakker 2006, Keifer et al 2007, Moser et al 2012 Sulakhe, Schechter et al 2005).

While Ca^{2+} may be sequestered in organelles, it can also be buffered by free-floating Ca^{2+} buffers, such as parvalbumin and calbindin-D28k (Ladewig et al 2004), calbindin-D9k (Lips & Keller 1998), and calretinin (Neverova et al 2007). These buffers bind to Ca^{2+}, making it unavailable for other reactions. Though mobile buffers are better studied, there are more immobile buffer sites in the cell than mobile ones (Ling 2008).

In addition to Ca^{2+} buffers, to maintain low intracellular Ca^{2+} concentrations in the cytosol and high Ca^{2+} concentrations inside of the endoplasmic and sarcoplasmic reticulum, active transport is required. This is primarily accomplished through Ca^{2+} pumps, which exist in the cell membrane (PMCA) (Smallwood et al 1983), the sarcoplasmic reticulum (SERCA) (Weber et al 1966), and the golgi bodies (SPCA) (Antebi & Fink 1992) as ATPases that shuffle Ca^{2+} across the cell membrane or into an organelle (Berridge 1997). Ca^{2+} pumps are generally less electrically active than might be anticipated for an ion transporter, such that they are electrically neutral or slightly electrogenic. This feature is accomplished by the counter-transport of H^+ ions in PMCA and SERCA pumps, and by Mn^{2+} in SPCA pumps (Van Baelen et al 2001). While SERCA pumps are known to have a slight lack of electroneutrality (Yu et al 1993), whether PMCA pumps are electrically neutral (Niggli et al 1982, Thomas 2009) or generate a slight current (Hao et al 1994) is still under debate. Ca^{2+} pumps are also aided by Na^+/Ca^{2+} exchangers, which are potently electrogenic, and play a key role in refilling the sarcoplasmic and endoplasmic reticulum, excitation-contraction coupling, cardiac muscle relaxation, and photoreception (Dipolo & Beaugé 2006).

B7. Serotonin, LTF, and Pathology

HMs and PMs are highly plastic, and can dynamically regulate the amplitude and frequency of their bursts depending on external conditions. During hypoxic challenges, ventilation is increased in a process known as the Hypoxic Ventilatory Response (HVR) (Feldman & McCrimmon 2008). During this response, phrenic nerve and hypoglossal

nerve burst amplitude increase. With repeated hypoxic challenges, the phrenic and nXII undergo an adaptive process called long-term facilitation (LTF), where either amplitude alone (Baker-Herman & Mitchell 2008, McKay et al 2004) or amplitude and frequency (Baker & Mitchell 2000) of bursts increases, and this increase persists for several minutes after the hypoxic challenges have ended (Feldman & McCrimmon 2008). LTF has also been shown to occur in singular HMs (Feldman et al 2005), and in this case, it is referred to as *in vitro* LTF (ivLTF); this observation allows for our study of LTF in singular motoneurons. The process of LTF is initiated by 5-HT, and as noted above, 5-HT exerts a variety of effects on HMs.

Activation of 5-HT_2Rs has been implicated as necessary for the initiation of LTF as measured by ventilation (McGuire et al 2004), *in vivo* adult phrenic nerve recordings (Kinkead & Mitchell 1999), and *in vitro* neonatal XII nerve recordings (Feldman et al 2005). In HMs, activation of 5-HT_2Rs has also been hypothesized to release stores of intracellular Ca^{2+} based on secondary messenger signaling modeling (Tsao & Butera 2008), resulting in membrane depolarization via inhibition of TASK channels and the I_h current (Xu et al 2009). 5-HTRs in general are also known to be necessary for LTF in the *in vivo* adult XII nerve response (Bach & Mitchell 1996). Activation of 5-HT_1Rs is generally not viewed as necessary for initiation of LTF in either the phrenic or XII nerve response (Feldman et al 2005, Kinkead & Mitchell 1999), but they are known to inhibit mAHP in HMs by inhibition of HVA Ca^{2+} channels (Talley et al 1997), and also possibly through direct inhibition of SK-channels (Grunnet et al 2004), making them a potent regulator of spike frequency (Talley et al 1997). 5-HT is not considered to be necessary for the maintenance of LTF (Fuller et al 2001).

The raphe nuclei, the primary source of 5-HT neurons in the brainstem, play a critical role in intermittent hypoxia-induced LTF in both the nXII and PMs (Bach & Mitchell 1996). These nuclei also play a complex role in the modulation of sleep states in the nXII and throughout the brain (Fenik et al 2005, Ursin 2002). During sleep, 5-HT output from the raphe is reduced (Portas et al 1998), which potentially disfacilitates both the HVR and LTF. Such a disfacilitation could play a role in respiratory-related pathologies in sleep, such as SIDS and OSA, which both have been linked to disorders in 5-HT-related systems (Behan & Brownfield 1999, Kinney et al 2007, Kraiczi et al 1999, Narita et al 2001, Panigrahy et al 2000, Weese-Mayer et al 2003). Additionally, developmental changes to 5-HTR density (Liu & Wong-Riley 2008, Liu & Wong-Riley 2010a) could exacerbate pathological conditions. In neonates, these characteristic developmental changes in 5-HTRs could jeopardize responses to hypoxic challenges, and potentially cause death (SIDS). In adults, disfacilitation of the nXII could result in insufficient tongue mobility during inspiration, leading the tongue to act as an obstruction (OSA).

Excitatory respiratory drive to HMs primarily stems from glutamatergic drive to AMPA receptors (AMPAR) (Greer et al 1991). LTF is generally considered to be the product of either the phosphorylation or upregulation of AMPAR (Feldman et al 2005). Therefore, consideration of possible mechanisms underlying APMAR-mediated changes is crucial for understanding how to simulate both realistic respiratory drive and plasticity changes to that drive.

Synaptic plasticity, including AMPAR-related plasticity, is known to be tied to mitogen activated protein kinase (MAPK) signaling cascades (Thomas & Huganir 2004),

which are implicated in the initiation of transcriptional events. Changes to AMPAR transcription would directly affect the concentration of free cytosolic AMPAR for insertion, and in turn result in an increase in membrane AMPAR concentrations.

In the absence of transcription, extant AMPARs can be modified through phosphorylation, which can aid in insertion into the extrasynaptic membrane (Liao et al 2001, Lu et al 2001), stabilize AMPAR already in the membrane (O'Brien et al 1999), and/or alter channel properties to enhance conductance. AMPARs contain no fewer than twelve phosphorylation sites (Song & Huganir 2002), leaving these receptors capable of receiving multiple modifications from a variety of sources. In the case of HMs, whether AMPAR phosphorylation enhances stability, insertion probability, conductance, or a combination of these three processes, is still an open question. It is known, however, that PKC can directly phosphorylate GluR1 or GluR2 AMPAR subunits during plasticity events (Boehm et al 2006, Chung et al 2000), and it has been hypothesized that this may occur in HMs (Feldman et al 2005).

C. Models

C1. Research Design

C1.a Numerical Integration

Numerical integration for all models except for the reduced and minimal models were performed via RK4, the most common Runge-Kutta method (Press 1992). All reduced and minimal models are numerically integrated via Euler's method, but initially checked against RK4 to ensure sufficient numerical accuracy and stability using Euler's.

C1.b Packages

Simulations were performed using the Python programming language (python.org) accompanied by the Scientific Tools for Python package (scipy.org). Speed-critical code was written in C++, and plugged into Python using the C-Extensions for Python library (cython.org). Plotting was done via the matplotlib library (matplotlib.sourceforge.net).

C1.c Model Types

All motoneuron models that follow are of the form of Hodgkin-Huxley type models. These models encapsulate motoneuron electrophysiology via Kirchoff's law, treating the membrane as a capacitor, and ion channels as variable resistors. All secondary messenger systems primarily take the form of kinetic equations, where the rates of chemical reactions are modeled by differential equations. Both Hodgkin-Huxley style models and kinetic equations are treated more completely, with derivations, in the Appendix.

C2. Hypoglossal Motoneuron Electrophysiology

The electrophysiological properties of all motoneuron models used in this project are Hodgkin-Huxley style models based on Purvis and Butera (2005), a HM model, and Amini et al (2004), a PM model. These properties are summarized in Figure 19 and the equations and parameters provided below:

$$C\frac{dV}{dt} = I_{input}(t) - \bar{g}_{leak}(V - E_{leak}) - \bar{g}_{Na}m_{Na}^3 h_{Na}(V - E_{Na}) - \bar{g}_{Na,p}m_{Na,p}h_{Na,p}(V - E_{Na})$$
$$- \bar{g}_K n_K^4 (V - E_K) - \bar{g}_A m_A h_A (V - E_K) - \bar{g}_h m_h (V - E_h) - \bar{g}_{SK} z_{SK}^2 (V - E_K) - \bar{g}_{BK} b_{BK} (V - E_K)$$
$$- \bar{g}_T m_T h_T (V - E_{Ca}) - \bar{g}_N m_N h_N (V - E_{Ca}) - \bar{g}_P m_P (V - E_{Ca})$$

Each of the above gating variables changes over time based on the following equations and parameters, where:

$$w = \{m_{Na}, h_{Na}, n_k, m_{Na,p}, h_{Na,p}, m_A, h_A, m_h, m_T, h_T, m_N, h_N, m_P, z_{SK}, b_{BK}\}$$

$$x = \{m_{Na}, h_{Na}, n_k, m_{Na,p}, h_{Na,p}, m_A, h_A, m_h, m_T, h_T, m_N, h_N, m_P\}$$

$$y = \{h_{Na}, n_k, m_A, m_h, m_T, h_T\},\ z = \{m_{Na}, m_{Na,p}, h_{Na,p}, h_A\ m_N, h_N, m_P, z_{SK}\}$$

$$\frac{dw}{dt} = \frac{w_\infty(V) - w}{\tau_w(V)} \qquad \tau_y(V) = \frac{\gamma_y}{e^{(\delta_{1,y}+V)/\varepsilon_{1,y}} + e^{-(\delta_{2,y}+V)/\varepsilon_{2,y}}} + \sigma_y$$

$$x_\infty(V) = \frac{1}{1 + e^{(\alpha_x - V)/\beta_x}} \qquad \tau_z(V) = \mu_z$$

With the following parameters:

	α	β	γ	δ_1	ε_1	δ_2	ε_2	σ	μ
m_{Na}	36	-8.5							0.1
h_{Na}	44.1	7	3.5	35	4	35	25	1	
n_k	30	-25	2.5	30	40	30	50	1	
$m_{Na,p}$	47.1	-4.1							0.1
$h_{Na,p}$	65	5							150
m_A	27	-16	1	40	5	74	7.5	0.37	
h_A	80	11							20
m_h	79.8	5.3	475	70	11	70	11	50	
m_T	38	-5	5	28	25	28	70	2	
h_T	70.1	7	20	70	65	70	65	1	
m_N	30	-6							5
h_N	70	3							25
m_P	17	-3							10
z_{SK}									1
b_{BK}									

$$\bar{g}_{leak} = 0.005\mu S, \quad \bar{g}_{Na} = 0.7\mu S, \quad \bar{g}_{Na,p} = 0.08\mu S, \quad \bar{g}_{K} = 1.3\mu S,$$
$$\bar{g}_{A} = 1.0\mu S, \quad \bar{g}_{h} = 0.005\mu S, \quad \bar{g}_{SK} = 0.7\mu S, \quad \bar{g}_{BK} = 0.08\mu S,$$
$$\bar{g}_{T} = 0.03\mu S, \quad \bar{g}_{N} = 0.05\mu S, \quad \bar{g}_{P} = 0.05\mu S, \quad \bar{g}_{Ca,leak} = 0.0003\mu S, \quad C = 0.04\,nF$$
$$E_{leak} = -80\,mV, \quad E_{Na} = 60\,mV, \quad E_{K} = -80\,mV, \quad E_{Ca} = 80\,mV, \quad E_{h} = -38.8\,mV$$

Gating variables associated with Ca^{2+}-gated K^{+} currents have custom steady state and/or tau equations, as shown below:

$$z_{SK,\infty}([Ca^{2+}]_m) = \frac{1}{1+\left(\frac{0.003}{[Ca^{2+}]_m}\right)^5}$$

$$b_{BK,\infty}(V,[Ca^{2+}]_m) = \frac{75\,[Ca^{2+}]_m\, e^{(V+30)/24}}{0.2\, e^{-(V+30)/24} + 75\,[Ca^{2+}]_m\, e^{(V+30)/24}}$$

$$\tau_b(V,[Ca^{2+}]_m) = \frac{0.4}{0.2\, e^{-(V+30)/24} + 75\,[Ca^{2+}]_m\, e^{(V+30)/24}}$$

Where $[Ca^{2+}]_m$ listed above corresponds to microdomain Ca^{2+} in the following section.

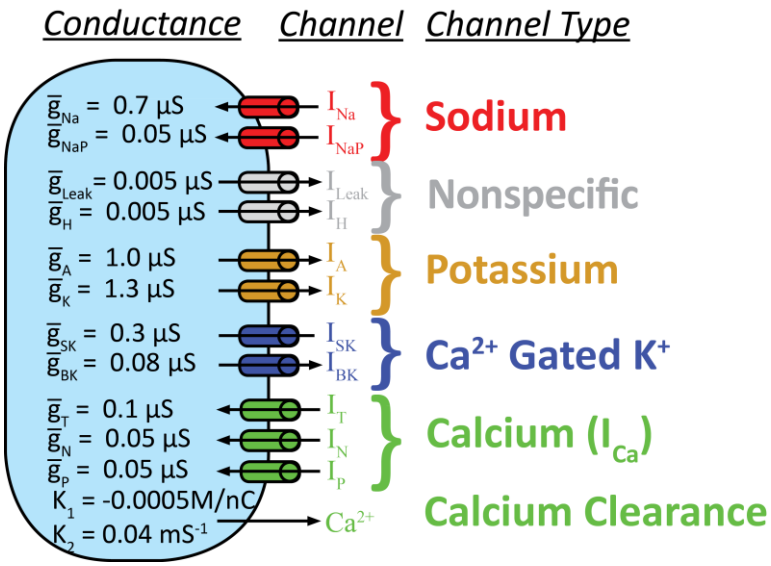

Figure 3: Electrophysiological Properties.
The electrophysiologial and Ca^{2+} related components of the modified Purvis & Butera model prior to more specific developmental modifications.

C3. Intracellular Calcium from the Microdomain to the Deep Cytosol

Intracellular Ca^{2+} is divided into two main domains: the Ca^{2+} microdomain ($[Ca^{2+}]_m$) and the deep cytosolic compartments.

The microdomains represent small volumes at the surface of the cell directly beneath voltage-gated Ca^{2+} channels. This imparts an irregular shape to its volume, and it must be handled separately from the rest of the cytosol. Inward current from voltage-

gated Ca^{2+} channels increases microdomain Ca^{2+}, and diffusion further into the cell and pumping out of the cell decrease microdomain Ca^{2+}. This can be represented mathematically as follows, and is based in part on Purvis and Butera (2005), Amini et al (2004), and custom derivations.

$$\frac{d[Ca^{2+}]_m}{dt} = \frac{d[Ca^{2+}]_m^{membrane}}{dt} + \frac{d[Ca^{2+}]_m^{diffusion}}{dt} + \frac{d[Ca^{2+}]_m^{buffering}}{dt}$$

The first member on the RHS of this equation represents the flow of ions across the cell membrane, both from ion channels and pumps, and is described mathematically as:

$$\frac{d[Ca^{2+}]_m^{membrane}}{dt} = K_1 I_{Ca} - K_2 [Ca^{2+}]_m$$

The following two members of the RHS of this equation represent the change in Ca^{2+} due to diffusion into the cytosolic space and buffering, respectively. Since Ca^{2+} flow from these two components moves to other parts of the model, they will be handled in subsequent parts in this section.

Deep cytosolic compartments, on the other hand, represent spherical shells of volume adjacent to the microdomains, moving progressively inward until the center of the cell is reached (Figure 4A). When these shells of volume are assumed to be infinitely thin, the necessary differential equations can be derived based on the continuity equation in radial coordinates. The full derivation is given in the Appendix, and is based on a derivation first suggested by Koch and Segev (1989). In addition, a number of modifications are made here to accommodate interactions with buffers and secondary messengers, which are written out based on $[Ca^{2+}]$ for readability, where $\rho = \{c1, c2, ..., c\max - 1\}$ represents the Ca^{2+} compartment:

$$\frac{\partial [Ca^{2+}]_\rho}{\partial t} = D\left(\frac{\partial^2 [Ca^{2+}]_\rho}{\partial r^2} + \frac{2}{r} \frac{\partial [Ca^{2+}]_\rho}{\partial r} \right) + \frac{d[Ca^{2+}]_\rho^{buffering}}{dt} + \frac{d[Ca^{2+}]_\rho^{IP3}}{dt}$$

Where the outermost compartment requires a slightly modified version of this equation:

$$\frac{\partial [Ca^{2+}]_{c\max}}{\partial t} = D\left(\frac{\partial^2 [Ca^{2+}]_{c\max}}{\partial r^2} + \frac{2}{r} \frac{\partial [Ca^{2+}]_{c\max}}{\partial r} \right)$$
$$+ \frac{d[Ca^{2+}]_{c\max}^{diffusion}}{dt} + \frac{d[Ca^{2+}]_{c\max}^{buffering}}{dt} + \frac{d[Ca^{2+}]_{c\max}^{IP3}}{dt}$$

While this describes how Ca^{2+} is shuffled about within the cytosol, it does not address how Ca^{2+} flows between the outermost shell and the irregularly shaped microdomains. If the innermost Ca^{2+} compartment is defined as $\frac{u_1}{r} = [Ca^{2+}]_{c1}$, the

outermost compartment as $\frac{u_{\max}}{r} = [Ca^{2+}]_{c\max}$, given the microdomain Ca^{2+} as $[Ca^{2+}]_m$, the following equation is obtained for the movement of Ca^{2+} between the cytosolic spherical diffusion system and microdomains:

$$\frac{d[Ca^{2+}]_m^{diffusion}}{dt} = K_3\left([Ca^{2+}]_{c\max} - [Ca^{2+}]_m\right)$$
$$\frac{d[Ca^{2+}]_{c\max}^{diffusion}}{dt} = K_3\left([Ca^{2+}]_m - [Ca^{2+}]_{c\max}\right)$$

Where the change to $[Ca^{2+}]_{c\max}$ due to diffusion into the microdomains is equal and opposite to the equation above.

Buffering is based on the Athanasiades et al (2000) model, but expanded to every compartment in the cytosolic Ca^{2+} diffusion model as well as to the microdomain. Buffering here loosely represents both free buffers and stored Ca^{2+} in the sarcoplasmic reticulum, and is governed by the following equations. Based on the observation that most buffers are not mobile (Ling 2008), diffusion of free Ca^{2+} binding proteins between compartments is not modeled. The fraction of total buffer saturation per Ca^{2+} compartment, B_i for $i = \{m, c1, c2, ..., c\max\}$, varies from zero to one, where zero indicates that all buffers are free and one indicates that all buffers are bound:

$$\frac{d[Ca^{2+}]_i^{buffering}}{dt} = -IW_i \frac{dB_i}{dt}$$
$$\frac{dB_i}{dt} = K_u [Ca^{2+}]_i (1 - B_i) - K_r B_i$$

When all of these Ca^{2+} mechanisms are combined, as summarized in Figure 4B, and this is incorporated into the HM motoneuron model from the previous section, the distinct behaviors in the microdomains ($[Ca^{2+}]_m$) and the cytosol ($[Ca^{2+}]_{c1}$) become apparent. Each individual rise in Ca^{2+} in $[Ca^{2+}]_m$ corresponds to an individual action potential whereas each individual rise in $[Ca^{2+}]_{c1}$, a Ca^{2+} spike, corresponds to a full burst of the HM (Figure 4C).

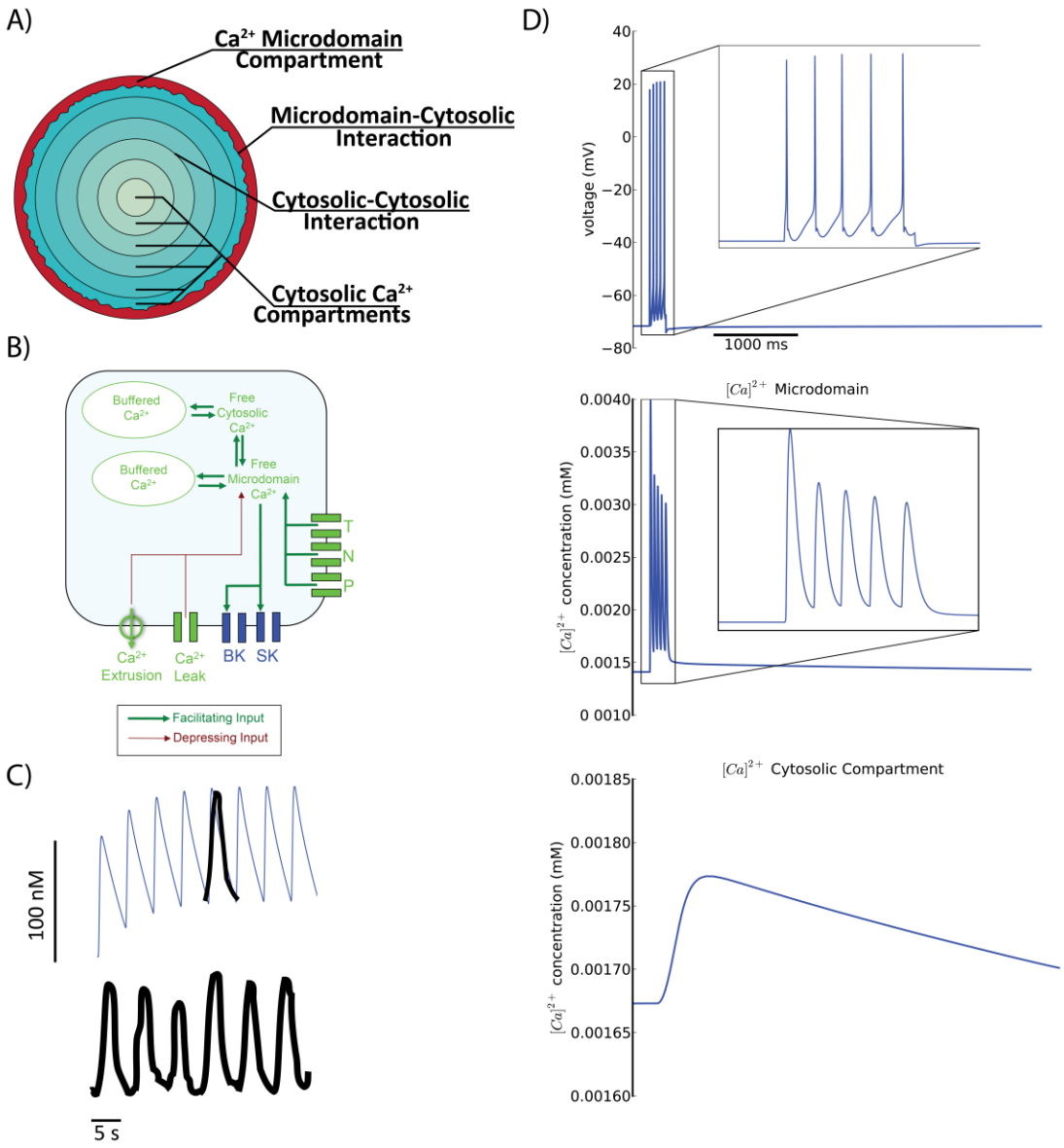

Figure 4: Ca^{2+} Modeling and Temporal Properties.
The complete listing of Ca^{2+}-related mechanisms in the HM model prior to being fit to specific developmental age ranges. A) Diagram of the spherical shells for spatial diffusion of Ca^{2+} in the HM model, with separate cytosolic and microdomain compartments. B) Schematic of all Ca^{2+}-related mechanisms, and their relationship, within the model. C) A comparison of model cytosolic Ca^{2+} (above, blue) to biological data (below, black) (adapted from Ladewig et al, 2004), where a single burst from the biological data is overlaid over the model, with both sets of data identically scaled. D) Ca^{2+} behavior in the HM model during constant current pulse in terms of voltage, microdomain Ca^{2+} ($[Ca^{2+}]_m$), and the innermost cytosolic Ca^{2+} compartment ($[Ca^{2+}]_{c1}$).

Parameters from this section are defined as follows, where $\rho = \{c1, c2, ..., c\max - 1\}$:

$$K_1 = -0.0005\,M/nC, \quad K_2 = 0.04\,ms^{-1}, \quad K_3 = 0.05575\,ms^{-1}, \quad D = 0.223\,\mu m/ms$$

$$IW_m = 0.012, \quad IW_\rho = 0.00001, \quad K_u = 100\,ms^{-1}, \quad K_r = 0.0952\,ms^{-1}$$

C4. 5-HT Based Secondary Messenger Systems

There are three main secondary messenger pathways in the model that are tied to 5-HT: the 5-HT_2/PKC pathway, the 5-HT_{1A} pathway, and the MAPK pathway, which begins at the end of the 5-HT_2/PKC pathway. All of these pathways are illustrated in Figure 5.

The 5-HT_2/PKC pathway is complex and plays a role in modulating cytosolic [Ca^{2+}], altering I_h conductance, and activating a MAPK signaling cascade critical to AMPAR upregulation. Once activation of 5-HT_2Rs activates its G-protein coupled $G_{\alpha q}$, it binds to PLC, splitting it into DAG and IP3, which in turn activates InsP3R to release Ca^{2+} stores from the sarcoplasmic reticulum. The model for this cascade is based on a heavily modified version of Cuthbertson and Chay (1991), and is shown below:

$$\frac{d[G_{\alpha q}\text{-}GTP]}{dt} = r_g - h_g\,[G_{\alpha q}\text{-}GTP] + k_{g2}[5\text{-}HT]$$

$$\frac{d[DAG]}{dt} = k_d[PLC] - h_d[DAG] + l_d$$

$$\frac{d[PKC]}{dt} = -q_2[PKC] + K_w([DAG] - K_0)$$

Where:

$$[5\text{-}HT] = \begin{cases} 0\mu M & \text{without } 5\text{-}HT \text{ application} \\ 50\mu M & \text{with } 5\text{-}HT \text{ application} \end{cases}$$

Due to dependencies between variables, some variables can be reduced to constants:

$$[IP3] = [DAG]$$

$$g^* = [G_{\alpha q}\text{-}GTP] / K_g$$

$$d^* = [DAG] / K_d$$

$$[PLC] = \frac{(d^*)^2}{1+(d^*)^2}\ \frac{(g^*)^4}{1+(g^*)^4}$$

IP3 releases stored Ca^{2+} and so we interpret this as releasing buffered Ca^{2+}. This gives rise to the following modification to the equation for changes to the fraction of occupied Ca^{2+} buffer, where deviations from the steady-state value of IP3 Ca^{2+} release and $\rho = \{c1, c2, ..., c\max\}$:

$$\frac{dB_\rho}{dt} = K_u\,[Ca^{2+}]_\rho\left(1 - B_\rho\right) - K_r\,\left(1 + K_v([IP3] - K_0)\right)B_\rho$$

Unlike the aforementioned changes, which involve the PKC pathway, the effect of activation of 5-HT_2Rs on I_h is expedient and does not appear to require secondary messengers. Therefore, it is modeled as a more direct modifier of I_h conductance directly from activated G-coupled proteins:

$$I_h = \bar{g}_h m_h (V - E_h) \frac{1}{1 + c_h [G_{\alpha q}\text{-}GTP]}$$

The 5-HT_{1A} pathway acts rapidly on High-Voltage Activated (HVA) Ca^{2+} channels, reducing their overall current in a manner similar to the effect of 5-HT_2 on I_h. This is accounted for in the model by the following modifications to N- and P-type Ca^{2+} channel current equations:

$$I_N = \bar{g}_N m_N h_N (V - E_{Ca}) \frac{1}{1 + c_N [G_i / G_0]}$$

$$I_P = \bar{g}_P m_P (V - E_{Ca}) \frac{1}{1 + c_P [G_i / G_0]}$$

Where $[G_i / G_0]$ is the G-coupled protein associated with 5-HT_{1A}R. For simplicity, it is assumed that 5-HT_2 and 5-HT_{1A} activate with the same dynamics, but with different overall concentrations due to differences in receptor density. Ergo, $[G_i / G_0]$ observes the following:

$$\frac{d[G_i / G_0]}{dt} = r_g - h_g [G_i / G_0] + k_{g1A}[5\text{-}HT]$$

Interfacing with genetic machinery will require that PKC now interact with MAPK signaling cascades. These chained kinase reactions are particularly useful in that they are known to exhibit both oscillatory and bistable properties, as seen in Qiao et al (2007), the MAPK signaling cascade model that we subsequently modify and incorporate into our model is as follows:

$$\frac{d[RAS]}{dt} = q_2 [PKC] - q_5 [RAS]$$

$$\frac{d[KKK\text{-}E1]}{dt} = a_1 [KKK][E1] - (d_1 + k_1)[KKK\text{-}E1] + .001(q_2 [PKC] - q_5 [RAS])$$

$$\frac{d[KKKs]}{dt} = k_1 [KKK\text{-}E1] - a_2 [KKs][E2] + d_2 [KKK\text{-}E2] - a_3 [KKKs][KK] + (d_3 + k_3)[KKKs\text{-}KK]$$
$$- a_5 [KK\text{-}P][KKKs] + (d_5 + k_5)[KK\text{-}P\text{-}KKKs]$$

$$\frac{d[KKK\text{-}E2]}{dt} = a_2 [KKK][E2] - (d_2 + k_2)[KKK\text{-}E2]$$

$$\frac{d[KK\text{-}KKKs]}{dt} = a_3 [KK][KKKs] - (d_3 + k_3)[KK\text{-}KKKs]$$

$$\frac{d[KK\text{-}P]}{dt} = k_3 [KK\text{-}KKKs] - a_4 [KK\text{-}P][KK\text{-}Pase] + d_4 [KK\text{-}P\text{-}KK\text{-}Pase] - a_5 [KK\text{-}P][KKKs]$$
$$+ d_5 [KK\text{-}P\text{-}KKKs] - k_6 [KK\text{-}PP\text{-}KK\text{-}Pase]$$

$$\frac{d[KK\text{-}P\text{-}KK\text{-}Pase]}{dt} = a_4 [KK\text{-}P][KK\text{-}Pase] - (d_4 + k_5)[KK\text{-}P\text{-}KK\text{-}Pase]$$

$$\frac{d[KK\text{-}P\text{-}KKKs]}{dt} = a_4 [KK\text{-}P][KK\text{-}Pase] - (d_5 + k_5)[KK\text{-}P\text{-}KKKs]$$

$$\frac{d[KK\text{-}PP]}{dt} = k_5[KK\text{-}P\text{-}KKKs] - a_6[KK\text{-}PP][KK\text{-}Pase] + d_6[KK\text{-}PP\text{-}KK\text{-}Pase] - a_7[KK\text{-}PP][K] + (d_7 + k_7)[K\text{-}KK\text{-}PP] - a_9[K\text{-}P][KK\text{-}PP] + (d_9 + k_9)[K\text{-}P\text{-}KK\text{-}PP]$$

$$\frac{d[KK\text{-}PP\text{-}KK\text{-}Pase]}{dt} = a_6[KK\text{-}PP][KK\text{-}Pase] - (d_6 + k_6)[KK\text{-}PP\text{-}KK\text{-}Pase]$$

$$\frac{d[K\text{-}KK\text{-}PP]}{dt} = a_7[K][KK\text{-}PP] - (d_7 + k_7)[K\text{-}KK\text{-}PP]$$

$$\frac{d[K\text{-}P]}{dt} = k_7[K\text{-}KK\text{-}P] - a_8[K\text{-}P][K\text{-}Pase] + d_8[K\text{-}P\text{-}K\text{-}Pase] - a_9[K\text{-}P][KK\text{-}PP] + d_9[K\text{-}P\text{-}KK\text{-}PP] - a_8[K\text{-}P][K\text{-}Pase] + d_8[K\text{-}P\text{-}K\text{-}Pase]$$

$$\frac{d[K\text{-}P\text{–}K\text{-}Pase]}{dt} = a_8[K\text{-}P][K\text{-}Pase] - (d_8 + k_8)[K\text{-}P\text{-}K\text{-}Pase]$$

$$\frac{d[K\text{-}P\text{-}KK\text{-}PP]}{dt} = a_9[K\text{-}P][KK\text{-}PP] - (d_9 + k_9)[K\text{-}P\text{-}KK\text{-}PP]$$

$$\frac{d[K\text{-}PP]}{dt} = k_9[K\text{-}P\text{-}KK\text{-}PP] - a_{10}[K\text{-}PP][K\text{-}Pase] + d_{10}[K\text{-}PP\text{-}K\text{-}Pase]$$

$$\frac{d[K\text{-}P\text{-}K\text{-}Pase]}{dt} = a_{10}[K\text{-}PP][K\text{-}Pase] - (d_{10} + k_{10})[K\text{-}PP\text{-}K\text{-}Pase]$$

Again, some variables may be set to constants based on their relationships with other variables:

$$[KKK] = [KKK\text{-}tot] - ([KKKs] + [KKK\text{-}E1] + [KKKs\text{-}E2] + [KK\text{-}KKKs] + [KK\text{-}P\text{-}KKKs])$$

$$[KK] = [KK\text{-}tot] - ([KK\text{-}P] + [KK\text{-}PP] + [KK\text{-}KKKs] + [KK\text{-}P\text{-}KKKs] + [KK\text{-}P\text{-}KK\text{-}Pase] + [KK\text{-}PP\text{-}KK\text{-}Pase] + [K\text{-}KK\text{-}PP] + [K\text{-}P\text{-}KK\text{-}PP])$$

$$[K] = [K\text{-}tot] - ([K\text{-}P] + [K\text{-}PP] + [K\text{-}KK\text{-}PP] + [K\text{-}P\text{-}KK\text{-}PP] + [K\text{-}P\text{-}K\text{-}Pase] + [K\text{-}PP\text{-}K\text{-}Pase]$$

$$[E1] = [E1\text{-}tot] - [KKK\text{-}E1]$$

$$[E2] = [E2\text{-}tot] - [KKK\text{-}E2]$$

$$[KK\text{-}Pase] = [KK\text{-}Pase\text{-}tot] - ([KK\text{-}P\text{-}KK\text{-}Pase] + [KK\text{-}PP\text{-}KK\text{-}Pase])$$

$$[K\text{-}Pase] = [K\text{-}Pase\text{-}tot] - ([K\text{-}P\text{-}K\text{-}Pase] + [K\text{-}PP\text{-}K\text{-}Pase])$$

A schematic summary of 5-HT-related secondary messenger pathways can be found in Figure 5.

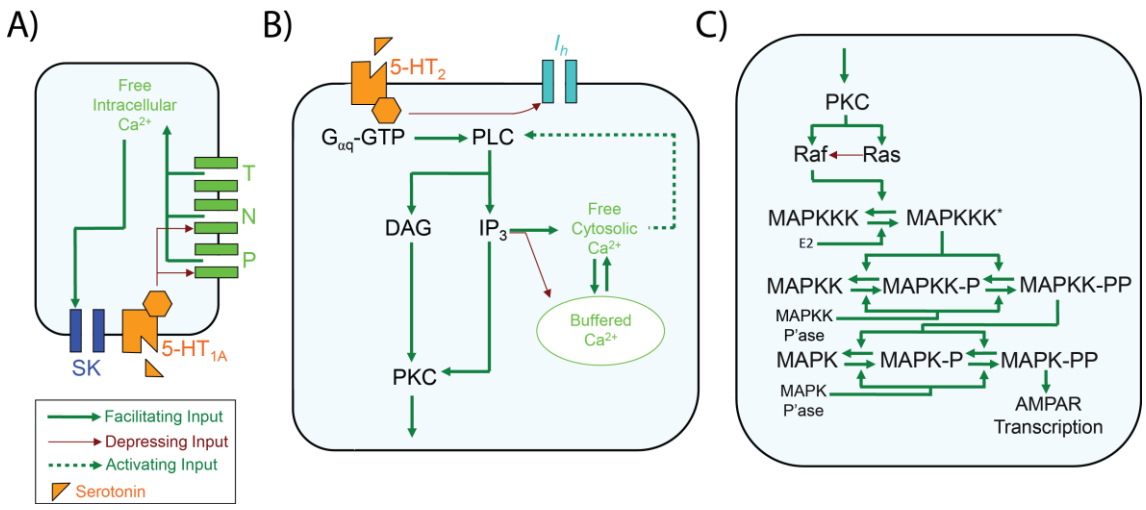

Figure 5: Serotonin Secondary Messenger Pathways.
Schematics detailing the relationships between electrophysiological, secondary messenger, and Ca^{2+} components. The 5-HT_2R pathway is split into two schematics for clarity. A) Diagram of relationships for 5-HT_{1A}R. B) Diagram of the first half of the 5-HT_2R pathway, and its interactions with intracellular Ca^{2+} stores through IP3. C) Diagram of the second half of the 5-HT_2R pathway, and its interactions with the MAPK cascade, and AMPAR transcription.

Parameters for this section are as follows:

$$r_g = 0.8\,\mu M/ms,\quad h_g = 5ms^{-1},\quad k_{g2} = 2ms^{-1},\quad k_{g1A} = 2ms^{-1},\quad k_d = 500\,\mu M/ms,\quad h_d = 5ms^{-1},$$

$$l_d = 0.3\,\mu M/ms,\quad K_g = 50\,\mu M,\quad K_d = 5\,\mu M,\quad K_u = 100ms^{-1},\quad K_r = 0.0952ms^{-1},$$

$$K_v = 1000,\quad K_w = 0.05714ms^{-1},\quad K_0 = 0.075\,\mu M,\quad c_h = 0.01\,\mu M^{-1},\quad c_N = 0.08\,\mu M^{-1},$$

$$c_P = 0.08\,\mu M^{-1},\quad q_1 = 3.0878x10^{-5}ms^{-1},\quad q_2 = 1.2121x10^{-4}ms^{-1},\quad q_3 = 2.6881x10^{-5}ms^{-1},$$

$$q_4 = 1.2420x10^{-4}ms^{-1}\quad q_5 = 1.4286x10^{-4}ms^{-1},\quad q_6 = 2.2263x10^{-5}ms^{-1},$$

$$q_7 = 4.0189x10^{-5}ms^{-1},\quad a_1 = 4.8143x10^{-2}ms^{-1},\quad a_2 = 2.6286x10^{-1}ms^{-1},$$

$$a_3 = 1.7571x10^{-1}ms^{-1},\quad a_4 = 4.2286x10^{-1}ms^{-1},\quad a_5 = 4.8286x10^{-1}ms^{-1},$$

$$a_6 = 2.780x10^{-1}ms^{-1},\quad a_7 = 3.2857x10^{-2}ms^{-1},\quad a_8 = 4.2429x10^{-2}ms^{-1},$$

$$a_9 = 4.8429x10^{-1}ms^{-1},\quad a_{10} = 1.3929x10^{-1}ms^{-1},\quad d_1 = 3.7286x10^{-2}ms^{-1},$$

$$d_2 = 2.8286x10^{-2}ms^{-1},\quad d_3 = 8.900x10^{-2}ms^{-1},\quad d_4 = 2.3286x10^{-2}ms^{-1},$$

$$d_5 = 8.6429x10^{-2}ms^{-1},\quad d_6 = 6.9714x10^{-3}ms^{-1},\quad d_7 = 9.9143x10^{-2}ms^{-1},$$

$$d_8 = 4.300x10^{-2}ms^{-1},\quad d_9 = 6.9286x10^{-2}ms^{-1},\quad d_{10} = 8.3857x10^{-2}ms^{-1},$$

$$k_1 = 2.0857x10^{-2}ms^{-1},\quad k_2 = 4.8286x10^{-2}ms^{-1},\quad k_3 = 6.000x10^{-2}ms^{-1},$$

$$k_4 = 9.543x10^{-2}ms^{-1},\quad k_5 = 3.0714x10^{-2}ms^{-1},\quad k_6 = 9.7143x10^{-3}ms^{-1},$$

$$k_7 = 6.2429x10^{-3}ms^{-1},\quad k_8 = 4.5286x10^{-3}ms^{-1},\quad k_9 = 9.3857x10^{-3}ms^{-1},$$

$$k_{10} = 2.5143x10^{-3}ms^{-1},\quad [KKK\text{-}tot] = 9.2235x10^{-4}\,\mu M,\quad [KK\text{-}tot] = 5.13\mu M,$$

$$[K\text{-}tot] = 8.1552x10^{-1}\,\mu M,\quad [E1\text{-}tot] = 7.9433x10^{-5}\,\mu M,\quad [E2\text{-}tot] = 3.2830x10^{-4}\,\mu M,$$

$$[KK\text{-}Pase\text{-}tot] = 9.2235x10^{-4}\,\mu M,\quad [K\text{-}Pase\text{-}tot] = 5.0345x10^{-1}\,\mu M$$

C5. Glutamate & AMPA

Since HMs are primarily driven by glutamatergic inputs, and a major facet of HM plasticity lies in an increase in AMPAR current, modeling some of the glutamatergic machinery is a prerequisite to a fully functional HM LTF model. There are three main parts that require particular attention: modeling of AMPAR current, modeling of upregulation of AMPAR production, and modeling of the effects of phosphorylation of AMPARs.

Electrophysiologically, AMPARs can be modeled just as any other ion channel, except for its gating properties, which must be considered separately. Since AMPARs are ligand-gated ion channels rather than being gated by membrane voltage, their gating properties are modeled via a kinetic model, where $[AMPAR]$ is the concentration of unbound AMPAR, $[Glu]$ is the concentration of glutamate in the synaptic cleft, $[AMPAR\text{-}Glu]$ is the concentration of bound AMPAR, and a and b are rate constants:

$$[AMPAR]+[Glu] \underset{b}{\overset{a}{\rightleftarrows}} [AMPAR\text{-}Glu]$$

$$\frac{d[AMPAR\text{-}Glu]}{dt} = a[AMPAR][Glu] - b[AMPAR\text{-}Glu]$$

To combine this model with an H-H-style current equation, we must convert the concentration of bound AMPAR to a gating variable whose values vary between zero and one. We can easily accomplish this by defining the gating variable $r(t)$ as the ratio of bound to total AMPAR:

$$r = \frac{[AMPAR\text{-}Glu]}{[AMPAR]+[AMPAR\text{-}Glu]}$$

$$\frac{dr}{dt} = a[Glu](1-r) - br$$

$$I_{Glu} = g_{Glu}\, r(t)(V - E_{Glu})$$

The concentration of glutamate in the synaptic cleft is a function of presynaptic voltage, and so we introduce the following equation based on Golomb and Amitai (1997), whose model for AMPAR is very similar to the derivation given above.

$$[Glu] = \frac{1}{1+e^{-(V_{pre}-\theta)/\sigma}}$$

$$V_{pre} = \begin{cases} -20mV & \text{when presynaptically active} \\ -80mV & \text{when presynaptically quiescent} \end{cases}$$

The variable g_{Glu} can be defined as being dependent on the concentration of AMPAR in the post-synaptic density (PSD):

$$g_{Glu} = \bar{g}_{Glu} \frac{[AMPAR_{PSD}^{free}] + [AMPAR_{PSD}^{bound}]}{AMPAR_{\max}}$$

An increase in PSD AMPARs can be achieved through three biologically plausible mechanisms: upregulation, insertion, and stabilization. The first of these mechanisms is slow, and may take several minutes to accomplish, as changes to AMPAR transcription must occur. The second two mechanisms are fast, and can occur as quickly as AMPARs can be phosphorylated. All three mechanisms first require a model of AMPAR movement and insertion into the PSD. The Earnshaw and Bressloff (2006) model is used for this, and we simplify and integrate this model into our HM models. AMPARs in the cell membrane can either be in the PSD, free floating ($[AMPAR_{PSD}^{free}]$) or bound to scaffolding proteins ($[AMPAR_{PSD}^{bound}]$), or in the extrasynaptic membrane (ESD), where it cannot contribute to AMPAR conductance at the synapse ($[AMPAR_{ESM}^{free}]$). Intracellular stores (ICS) of AMPARs in the dendritic spine ($[AMPAR_{store}]$) can be exocytosed directly into the ESM. AMPARs that are unbound can freely slide from the PSD to the ESM, where they are also endocytosed back into the ICS. Equations describing these behaviors are provided below:

$$[AMPAR_{PSD}^{free}] = -\alpha(L - [AMPAR_{PSD}^{bound}])[AMPAR_{PSD}^{free}] + \beta[AMPAR_{PSD}^{bound}] - \frac{h}{A_{PSD}}([AMPAR_{PSD}^{free}] - [AMPAR_{ESM}^{free}])$$

$$[AMPAR_{PSD}^{bound}] = \alpha(L - [AMPAR_{PSD}^{bound}])[AMPAR_{PSD}^{free}] - \beta[AMPAR_{PSD}^{bound}]$$

$$[AMPAR_{ESM}^{free}] = \frac{h}{A_{PSD}}([AMPAR_{PSD}^{free}] - [AMPAR_{ESM}^{free}]) - \frac{\Omega}{A_{ESM}}([AMPAR_{ESM}^{free}] - [AMPAR_{ESM}^{free}]_{bkg})[AMPAR_{PSD}^{free}] - \kappa[AMPAR_{ESM}^{free}] + \frac{s_k}{A_{ESM}}[AMPAR_{store}]$$

$$[AMPAR_{ESM}^{free}] = -s_k[AMPAR_{store}] + \delta$$

Where L represents the concentration of scaffolding protein binding sites in the PSD, s_k is the exocytosis rate per AMPAR within the ICS, κ is the endocytosis and degradation rate for AMPAR in the ESM, Ω represents the rate at which AMPAR in the ESM move off of the dendritic spine entirely, A_{ESM} and A_{PSD} are representations of surface area, h is the rate that free AMPAR hop between the PSD and ESM, α and β dictate binding and unbinding rates to scaffolding proteins, and δ represents the rate of AMPAR production.

With a model of AMPAR movement in place, this model can now be modified to incorporate AMPAR trafficking and phosphorylation. Increases in AMPAR trafficking due to MAPK interactions with genetic machinery are modeled as follows:

$$\delta = \bar{\delta}(1 + \delta_\alpha[K\text{-}PP])$$

Phosphorylation by PKC can result in two possible effects, and it is unclear which one actually occurs in HMs, although both produce similar outcomes. The first effect is an increase in exocytosis probability, resulting in heightened AMPAR insertion into the ESM:

$$s_k = \bar{s}_k(1 + s_\alpha[PKC])$$

The second effect is a stabilization of the AMPAR, reducing the likelihood of endocytosis from the ESM:

$$\kappa = \bar{\kappa}(1 + \kappa_\alpha[PKC])$$

A schematic representation of AMPAR trafficking, and its relation to secondary messenger systems, is given in Figure 6.

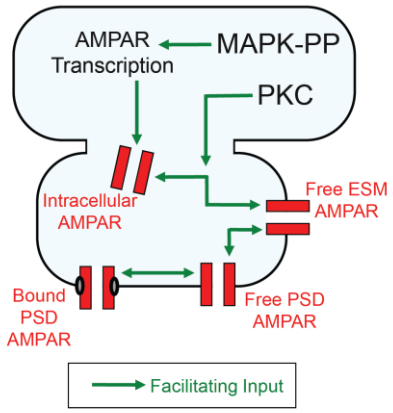

Figure 6: AMPAR Trafficking and Its Relation to Secondary Messenger Systems.
Diagram showing the complete process of AMPAR trafficking, including the relationship between the different AMPAR variables. AMPAR insertion can be increased by either an increase in AMPAR transcription or phosphorylation of the AMPAR by PKC.

Parameters for this section are as follows:

$$a = 1.0\mu M^{-1},\quad b = -0.0067,\quad \theta = -20,\quad \sigma = 2.0,\quad \bar{g}_{Glu} = 4.0\mu S,\quad AMPAR_{\max} = 50\mu M,$$
$$\alpha = 1x10^{-9}\,\mu m^2/ms,\quad \beta = 1x10^{-8}\,ms^{-1},\quad [AMPAR_{ESM}^{free}]_{bkg} = 10\mu m^{-2},\quad L = 159.15\mu m^{-2},$$
$$h = 1.257x10^{-6}\,\mu m^2/ms,\quad \Omega = 1.257x10^{-6}\,\mu m^2/ms,\quad A_{PSD} = 0.1257\mu m^2,$$
$$A_{ESM} = 10A_{PSD},\quad \kappa = 1.667x10^{-5}\,ms^{-1},\quad s_k = 5.556x10^{-7}\,ms^{-1},\quad \delta = 2.77810^{-4}\,\mu m^2/ms$$

C6. Complete Secondary Messenger Systems

While the relationship between each secondary messenger system in the previous sections has already been explicitly detailed, differential equations alone may not impart an intuitive sense for how each subsystem interacts. For this reason, the interactions

among all of the previously detailed secondary messenger systems is provided below in Figure 7.

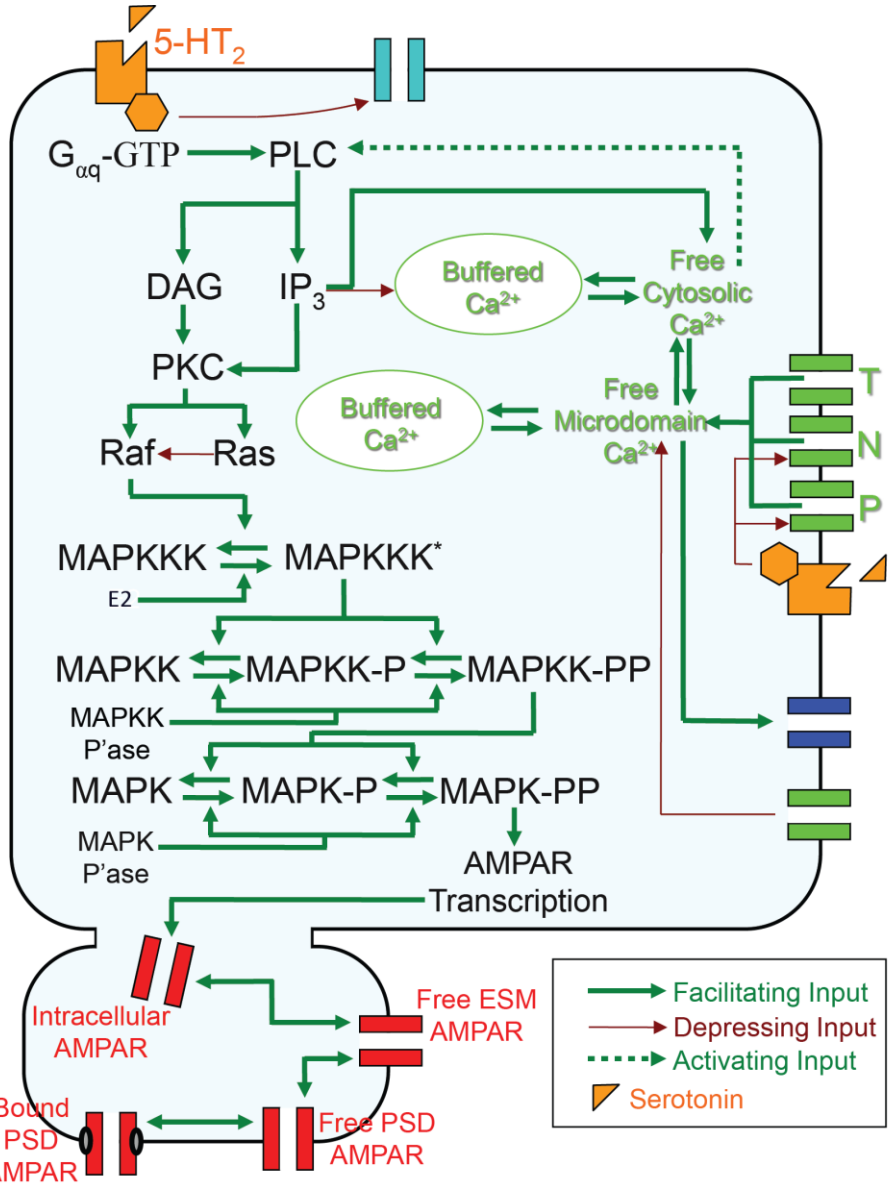

Figure 7: Schematic of All Secondary Messenger Systems and Their Interactions.
Diagram demonstrating all components of the model that are not purely electrophysiological, and their interactions. This includes 5-HT mechanisms, AMPA mechanisms, the flow of Ca^{2+}, a PKC pathway, MAPK signaling cascades, and AMPAR upregulation and trafficking.

The MAPK-AMPAR components of the model exhibit bistability. When this system is taken from its steady-state, and MAPKK-PP is forced to various values (0.0µM, 0.5µM, 1.0µM, 1.5µM, 1.6µM, 1.9µM, 2.0µM, 2.5µM, 3.0µM, 3.5µM), the system returns to one of two equilibrium points (Figure 8A,B). This bistability is not exhibited when MAPKKK*, MAPK-PP, free AMPAR, or bound AMPAR are similarly modified (not shown). When coming to one of two equilibria, other components downstream of MAPKK-PP in the model, such as MAPK-PP and total PSD AMPAR

(Free+Bound PSD AMPAR), also come to a new equilibrium (Figure 8C,D). Attempting to force MAPK-PP, free PSD AMPAR, or bound PSD AMPAR to a new value after MAPKK-PP has been forced to one of its two equilibrium points will result in a steady decay back to the equilibrium dictated by MAPKK-PP. The importance of this bistability occuring beyond the MAPK circuit in AMPAR density is that such changes in state are not simply reserved for internal MAPK dynamics, but have a tangible effect on firing frequency.

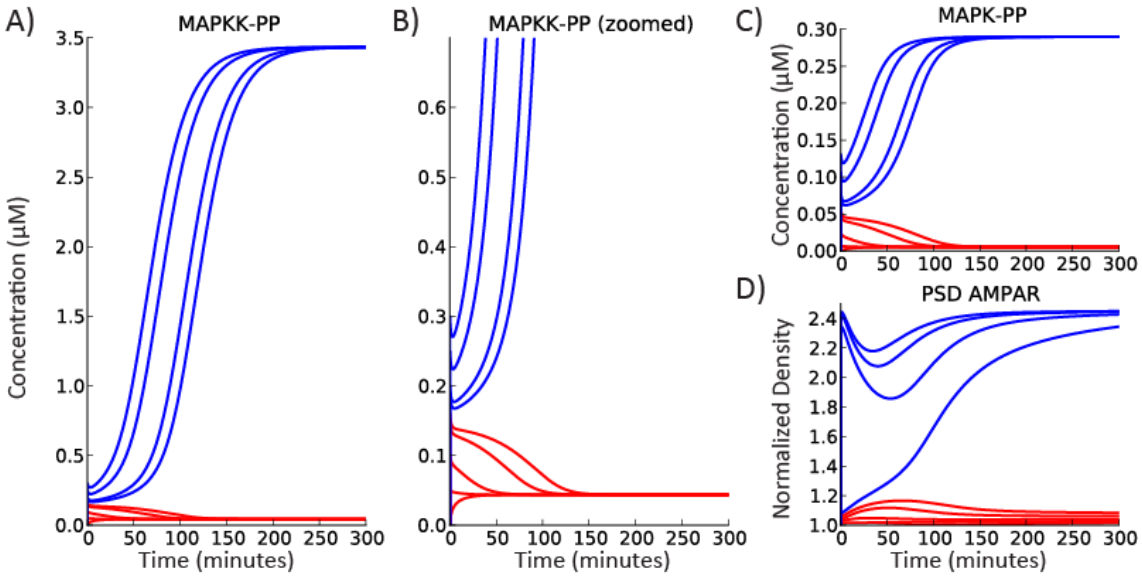

Figure 8: MAPK Bistability and its Effect on Long-Term AMPAR Density.
Demonstration of bistability within the MAPK signaling cascade when MAPKK-PP is forced to a series of different values. A,B) MAPKK-PP, the component of the model exhibiting independent bistability, C) MAPK-PP, the final output of the MAPK circuit that directly affects AMPAR production, which exhibits bistability dependent on MAPKK-PP, and C) The sum of free and bound AMPAR in the PSD normalized to its steady-state value, which exhibits bistability dependent on MAPKK-PP.

D. Model Development

Since HMs of various ages exhibit distinct firing properties, and since only some developmental changes can be known from the biological literature, a degree of unverifiable parameter manipulation will be required to generate full HM models for various ages. Rather than applying an optimization algorithm over the parameters, and risk converging to something biologically implausible, we opt to evaluate likely mechanisms that could explain various behaviors, and to a lesser extent explore parameter space for parameters not clearly defined by the biological literature. In this manner, we lay out logical reasons for each biologically unverified change to the original Purvis and Butera (2005) model.

As noted by Viana et al (1995), there are two main firing profiles in HMs: Type I and Type D. In Type I HMs, firing frequency gradually increases to steady-state, while in Type D HMs, firing frequency is initially very high but rapidly comes to equilibrium at a lower frequency. Both firing behaviors are of developmental interest, as Type I firing observed exclusively in juvenile HMs while Type D firing is primarily observed in neonatal and adult HMs. A specific subtype of Type I behavior, termed Type ID behavior, begins with firing frequency gradually increasing, but rather than coming to steady state, it mildly adapts with a downward slope.

To better elucidate the mechanisms driving the distinctions between Type I and Type D behaviors, we take the Viana et al (1995) observation that replacing extracellular Ca^{2+} with Mn^{2+} converts Type I firing into Type D firing, and investigate mechanisms associated with Ca^{2+} to narrow down possible candidates useful for converting between types. First we consider the addition of BK, buffering, and linear cytosolic diffusion to the original Purvis and Butera (2005) model. Next, we add developmentally known changes, and additionally consider the effects of altering voltage-gated Ca^{2+} channel conductance, modifying the kinetics of HVA channels, and again look at changes to BK, buffering, and spherical cytosolic diffusion. In this manner we gain a better understanding of the Purvis and Butera (2005) model both in its original form, and after modifications to make it more developmentally relevant.

Our simulations indicate that Ca^{2+} related mechanisms alone can convert between Type I and Type D behaviors in the original Purvis and Butera (2005) model, and that cytosolic diffusion outside of Ca^{2+} microdomains may play more of a role in firing properties than is typically considered. In particular BK-channels heighten Type I behavior in the original model (Figure 12), and microdomain buffering converts Type I behavior to Type D behavior (Figure 14). When a simplified linear diffusion model is added it becomes possible to capture a series of slow adaptation behaviors, where adaptation may take over a second or last beyond tens of seconds, seen in both early neonates, neonates, and juveniles (Figure 15).

With some understanding of the mechanisms that set firing behavior type, we now add known developmental changes from the literature. Numerous changes occur to HMs through development, many of which are summarized in Figure 9. Variation in firing properties are quite common in HMs (Viana et al 1995), and so fitting firing behaviors precisely to data from a single neuron is less important than being able to reproduce key firing behaviors. Aforementioned differences in the Background & Significance section on Developmental Changes to Hypoglossals also highlight that the ratio of different HVA channels may vary from HM to HM, reinforcing the difficulty in finding a "perfect fit" to parameters that aren't entirely consistent. Regardless, based on what is known about HM development, we propose the following modifications to the Purvis and Butera (2005) model to better fit three developmentally distinct ages:

	Neonate (P3-P5)	Juvenile (P7-P12)	Adult (>P21)	Support
$\bar{g}_h$	0.005 μS	0.005 μS	0.05 μS	Bayliss et al (1994a)
$\bar{g}_N$	0.05 μS	0.2 μS	0.0375 μS	Miles et al (2004), Umemiya and Berger (1994), sections D6. D7.
$\bar{g}_P$	0.1 μS	0.1 μS	0.1125 μS	

$\bar{g}_{BK}$	0 μS	0 μS	0.09 μS	Pedarzani et al (2000), section D2.
$\bar{g}_{Ca,leak}$	0.0003 μS	0.0005 μS	0.0005 μS	
IW_m	0.2	0.0	0.075	Tsai et al (1997), sections D3. D7.
μ_{mN}	2.5 *ms*	5 *ms*	2.5 *ms*	McEnery et al (1998), section D5.
μ_{mP}	5 *ms*	10 *ms*	5 *ms*	
k_g	2.0	1.2	2.0	Liu and Wong-Riley (2008), Liu and Wong-Riley (2010a)
S_{5-HT}	1.0	0.75/0.6	0.75	

These changes generate distinct firing properties that closely match a variety of topological and numerical properties observed in actual HMs, as shown in Figure 10. Additionally, we presume that distinct firing behaviors seen through development are contiguous (neonate cells become juvenile cells, who later become adult cells), and so every attempt was made to minimize the number of overall changes necessary, resulting in a series of models that are still close in parameter space, and can reasonably be transitioned through a small set of modifications, as would be expected to happen during development.

While the above parameters are not absolute, except for those derived from biological data, the logic for said changes is rooted in a combination of the literature and the given findings below, with additional considerations for families of valid parameters given in section D7.

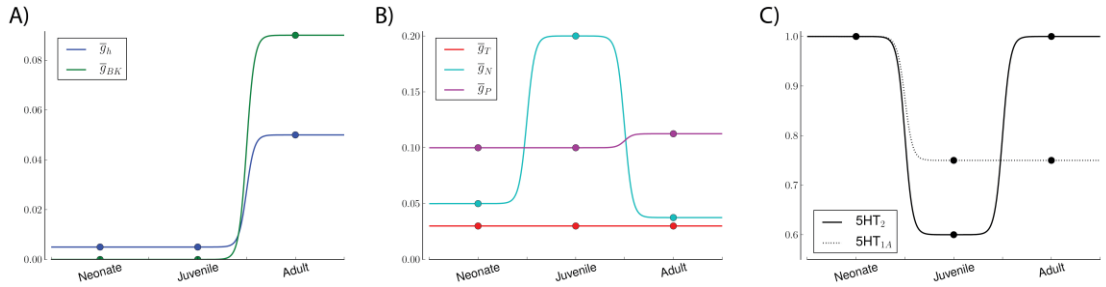

Figure 9: Developmental Conductance Changes to the Three HM Models.
Plots for changes to conductances that distinguish the three developmental HM models: neonatal, juvenile, and adult. A) Changes to I_h and BK channels based on the literature. B) Changes to voltage-gated Ca^{2+} channels based on the literature and fitting. C) Changes to 5-HTR subtypes based on the literature.

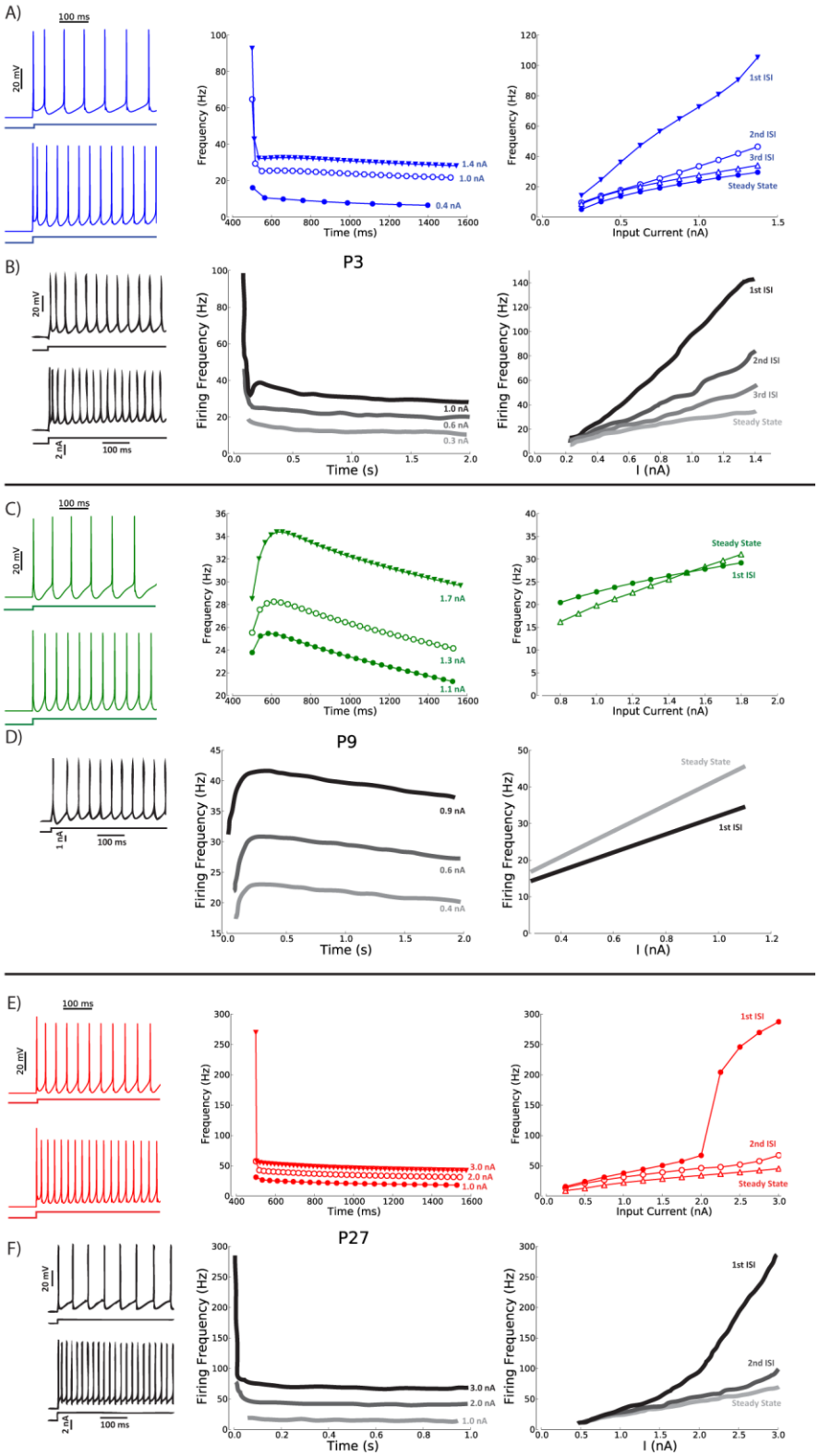

Figure 10: Developmental HM Models Compared to Biological Data.
Spike traces, firing frequency over time, and firing frequency vs input current with changes both from literature and from Ca^{2+} modification investigations for A) the final neonatal HM model, B) biological neonatal HM data, C) the final juvenile HM model, D) biological juvenile HM data, E) the final adult HM model, F) biological adult HM data. All data adapted from Viana et al (1995).

D1. Ca^{2+} Extrusion Mechanisms

Because Ca^{2+} plays many key roles in firing properties and plasticity in motoneurons, an investigation of how Ca^{2+} extrusion mechanisms affect excitability may yield further insight into firing behaviors. Three forms of Ca^{2+} extrusion are considered: an exponential decay of Ca^{2+}, Ca^{2+} pumps, and Na^{+}/Ca^{2+} exchangers. While initially changing the exact mechanism for Ca^{2+} extrusion in the original Purvis and Butera (2005) model does not seem to generate significant differences in behavior, such models frequently exhibit nonlinear effects. So, each mechanism for extrusion additionally had either BK-channels or microdomain buffering added to the model. The results of these perturbations are described below (Figure 12, Figure 14), and otherwise indicate that an exponential decay of Ca^{2+} most reasonably captures behavior observed in HM biological data.

D2. BK-Channels and Type I behavior

As described in (Viana et al 1995), juvenile HMs exhibit Type I firing behavior. wherein a rapid acceleration quickly comes to a steady state firing frequency. When BK-channels are added to the Purvis and Butera (2005) model with three distinct mechanisms for Ca^{2+} extrusion, in every model all but the first Ca^{2+} spike is reduced, which subsequently pushes models toward Type I behavior (Figure 11). This transition toward Type I behavior is consistent even under a variety of input currents (Figure 12).

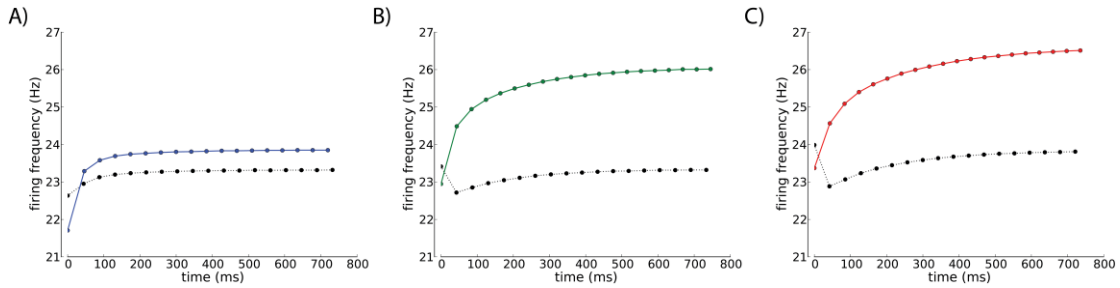

Figure 11: The effect of BK-channels on Firing Frequency.
While the initial addition of BK channels does not seem to make a marked difference in each of the models' voltage traces (not shown,) subtle changes arise when we look at how this addition modifies firing frequency over time. The original firing frequency (dotted lines) are compared to the addition of BK (colored line) in each of the three Ca^{2+} extrusion models: A) exponential decay of Ca^{2+} (blue), B) Ca^{2+} pump (green), and C) Na^{+}/Ca^{2+} exchanger (red). Without BK, only an exponential decay of Ca^{2+} nicely characterizes Type I firing.

When Na^{+}/Ca^{+2} exchangers are used for Ca^{2+} extrusion, the first inter-spike interval (ISI) appears to be fixed regardless of input current, which is not observed in the biological data. When Ca^{2+} pumps are used for Ca^{2+} extrusion, the steady state firing frequency increases nonlinearly with input current, which is not observed in Type I HMs. Exponential decay of Ca^{2+} yields the results most consistent with Type I biological data, producing both a first ISI and steady state ISI that rise linearly with input current. Mixtures of Na^{+}/Ca^{2+} exchangers and Ca^{2+} pumps (not shown) do not yield more reasonable results than exponential decay of Ca^{2+} alone.

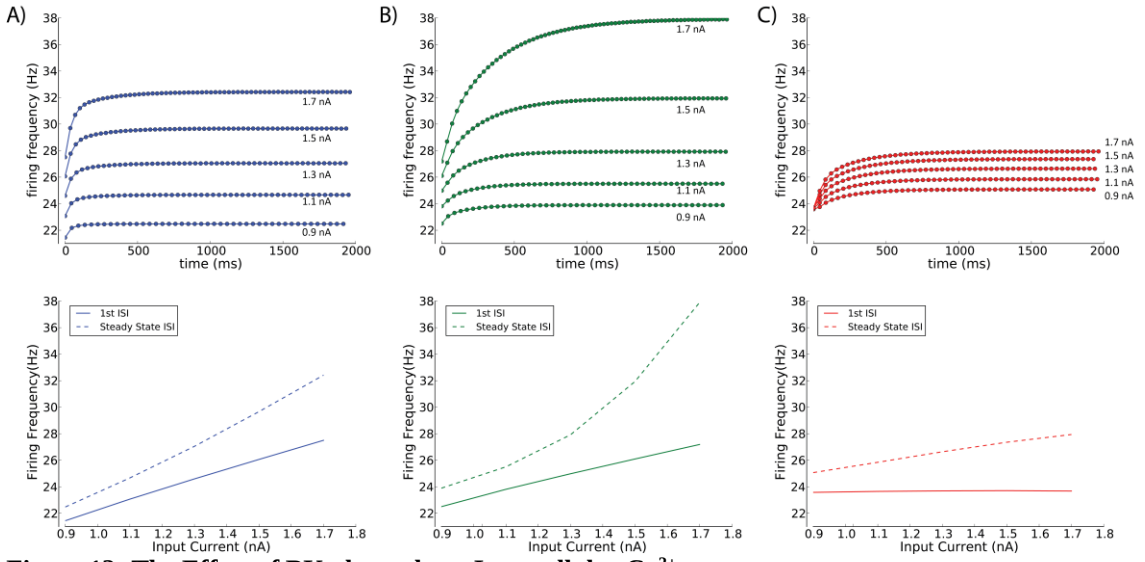

Figure 12: The Effect of BK-channels on Intracellular Ca^{2+}.
While the initial addition of BK channels does not seem to make a marked difference in each of the models' voltage traces (not shown,) subtle changes arise when we look at how this addition modifies firing frequency over time. The original firing frequency (dotted lines) are compared to the addition of BK (colored line) in each of the three Ca^{2+} extrusion models: A) exponential decay of Ca^{2+} (blue), B) Ca^{2+} pump (green), and C) Na^{+}/Ca^{2+} exchanger (red). Without BK, only an exponential decay of Ca^{2+} nicely characterizes Type I firing.

D3. Microdomain Buffering and Type D behavior

Also described in (Viana et al 1995), neonate and adult HMs exhibit Type D firing behavior, where a very short first ISI rapidly adapts to a much lower steady state firing frequency. With the addition of microdomain buffering to the three Purvis and Butera (2005) models with distinct Ca^{2+} extrusion mechanisms, we observe a sharp shortening of the first ISI (Figure 13), a slowing of microdomain Ca^{2+} accumulation, and an overall decrease in the height of Ca^{2+} spikes. With the application of a variety of different input currents to all models, a rapid shift toward Type D behavior in all models is observed (Figure 14, Figure 13).

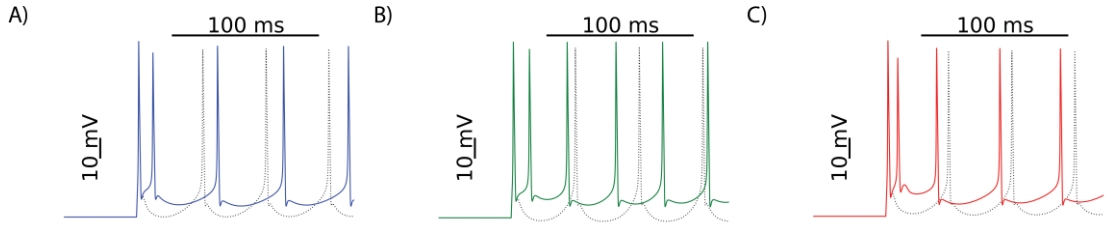

Figure 13: The effect of Buffering on Firing Frequency.
When Ca^{2+} buffering is added to Ca^{2+} microdomains, firing frequency tends to increase, with characteristically short first ISIs all three extrusion model variants: A) exponential decay of Ca^{2+} (blue), B) Ca^{2+} pump (green), and C) Na^{+}/Ca^{2+} exchanger (red). Note that the effect of buffering is the reverse of BK-channel addition.

The addition of Na^+/Ca^{2+} exchangers yields nonlinear changes to the first ISI under different input currents, but an unchanging firing frequency with all other ISIs regardless of input current. With Ca^{2+} pumps, the first ISI changes linearly with input current, as is observed in biological data, but at very low input currents the first ISI becomes uncharacteristically large, which does not fit with what is known of Type D HMs. Again exponential decay of Ca^{2+} exhibits the most biological behavior, exhibiting a first ISI that increases linearly with input current, and subsequent ISIs increasing linearly, but with a less pronounced slope.

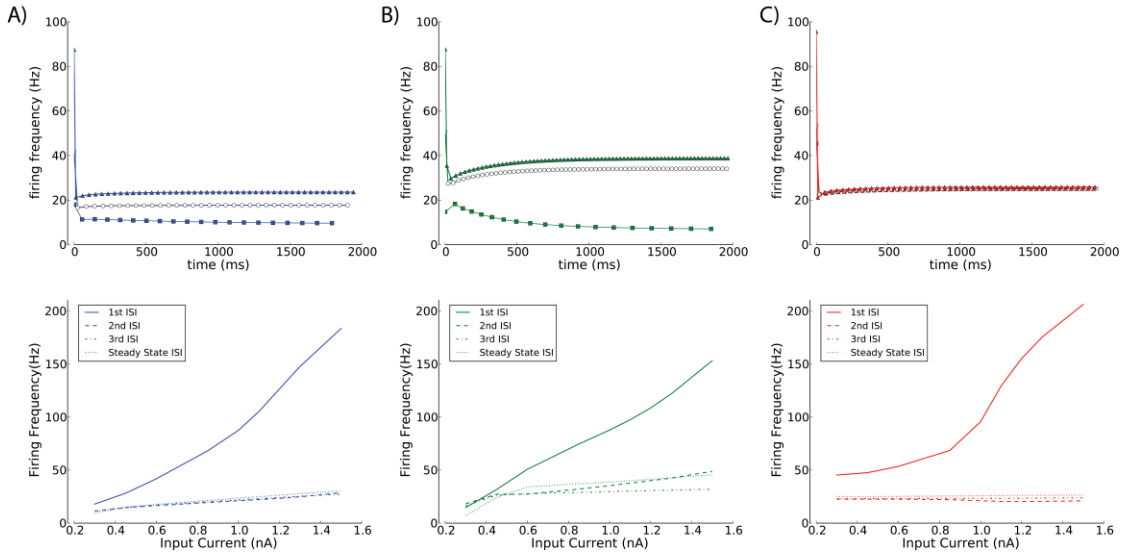

Figure 14: The Effect of Microdomain Buffering on Firing Dynamics.
Depictions of both the firing frequency over time for a few specific set input currents, and the full relationship between firing frequency and input current, for HM models modified with the addition of microdomain buffering, and calcium extrusion via A) exponential decay of Ca^{2+} (blue), B) Ca^{2+} pump (green), and C) Na^+/Ca^{2+} exchanger (red).

D4. Cytosolic Diffusion, Type ID behavior, and slow adaptation

Cytosolic diffusion of Ca^{2+} away from microdomains into the cytosol is well understood to be important in terms of intracellular Ca^{2+} dynamics, but is not typically considered a significant event with respect to electrophysiological properties. Here we present a simple linear model of Ca^{2+} diffusion demonstrating that not only does cytosolic diffusion have a profound effect on firing frequency, but it can also help to capture some firing frequency properties that have otherwise been difficult to capture with ion channels alone.

Very young neonates also demonstrate an extremely slow adaptation over several seconds that does not readily fit Type I or Type D classifications. The addition of cytosolic diffusion alone, without BK-channels or microdomain buffering readily produces this form of adaptation (Figure 15a).

By increasing the rate of diffusion, we may produce Type I behavior that exhibits an adaptation-acceleration-adaptation shape in its ISI vs time curves. While this is commonly seen in neonatal HMs, the behavior itself cannot readily be produced in any other manner (Figure 15b).

A further addition of BK-channels yields Type ID behavior, which is common to juvenile HMs, where a rapid acceleration gives way to a slower, linear adaptation (Figure 15c). The common theme to all forms of cytosolic diffusion based electrophysiological behavior is the addition of extremely slow adaptation properties, which themselves may go on at least for several seconds, if not until the neuron ceases to fire.

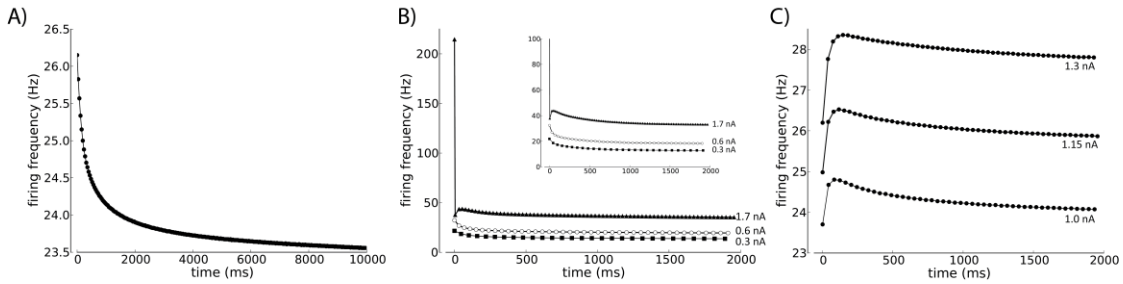

Figure 15: The effect of linear Ca2+ diffusion within the cell.
While previous additions yield a wide variety of biologically observed behaviors, we still lack mechanisms for slow adaptation properties. With the addition of linear Ca^{2+} diffusion, we can produce several distinct adaptation behaviors with either A) diffusion alone, producing an early P1 behavior, B) stronger diffusion, yielding a transient increase in frequency during early ISIs, or C) BK-channels and diffusion, which produces Type ID behavior. Notice how adaptation can be stretched out significantly, sometimes even lasting for tens of seconds.

D5. HVA Channel Kinetics

Based on the possibility of changes to gating kinetics due to developmental changes in ion channel protein composition, we additionally investigate the effect of modifications to HVA channel kinetics through variation of activation time constants. Instead of applying these changes directly to the original Purvis and Butera (2005) model, we take all of the modifications listed earlier in this section, so as to demonstrate how channel kinetics affect the final model itself.

Doubling HVA current activation tau (Figure 16d,e,f) tends to greatly accentuate the fAHP, and dramatically increases the frequency of the second ISI at higher input currents, while generally increasing the first ISI's frequency over a broad range of currents. Halving tau (Figure 16a,b,c) seems to push the capacity for dramatic increases in first ISI frequency completely out of the observed range, making both neonate and adult models behave more "neonate"-like. Changes to tau tend to have a mild effect on excitability in juveniles, with an increased tau decreasing firing frequencies across all ISIs regardless of input current.

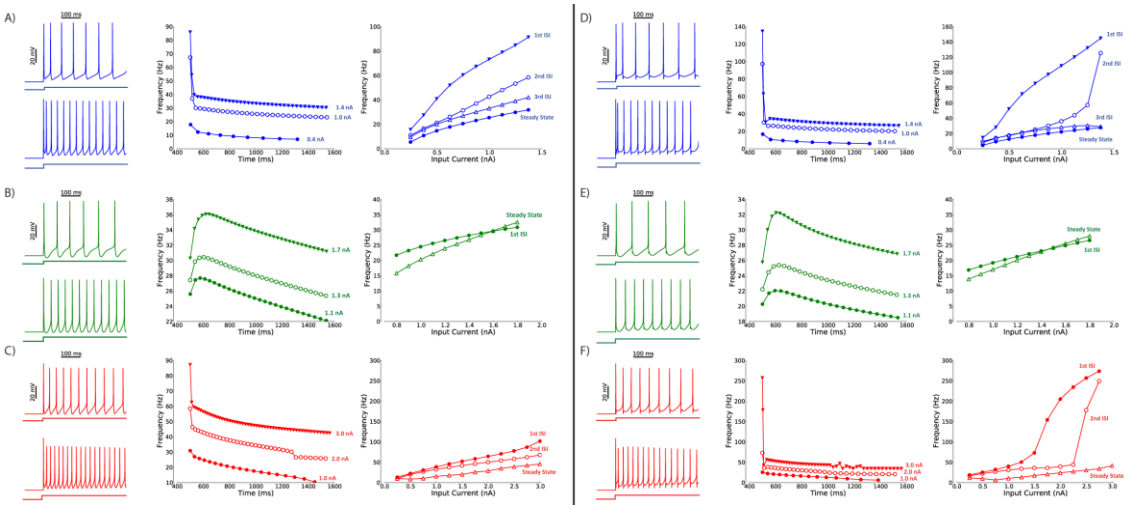

Figure 16: Depiction of Model Changes With Slower or Faster HVA Channel Kinetics.
Spike traces, firing frequency over time for select input currents, and firing frequency vs input current after a 0.5x (A,B,C) or 2.0x (D,E,F) change in HVA channel activation time constants, A,D) neonatal HM, B,E) juvenile HM, and C,F) adult HM.

D6. HVA Currents

As a final attempt at observing the effect of modifying the source of incoming Ca^{2+}, we take the final model with all modifications, and demonstrate the effect of increasing either of the two HVA Ca^{2+} channels. The main goal in this step is to explore the possibility that variations in Ca^{2+} influx from cell to cell can make certain cells more "neonatal" or "juvenile", even if they aren't developmentally at that age group.

While increasing HVA current tends to increase the frequency of the first ISI at lower input currents in neonates, paradoxically we see the opposite effect in adults. Decreasing HVA currents tends to have the inverse effect, and further stratifies ISI frequencies after the first. Subsequently, increasing HVA current (Figure 17d,e,f) tends to make juveniles more "adult", and adults more "juvenile", while decreasing it (Figure 17a,b,c) tends to return adults and juveniles to their more typical firing behavior. As might be expected, decreasing HVA current also reduces mitigation of the fAHP by the Ca-mediated ADP. Increasing HVA current in juveniles tends to bring early ISIs with different input currents closer together in terms of firing frequency, and push them further apart as conductance is decreased.

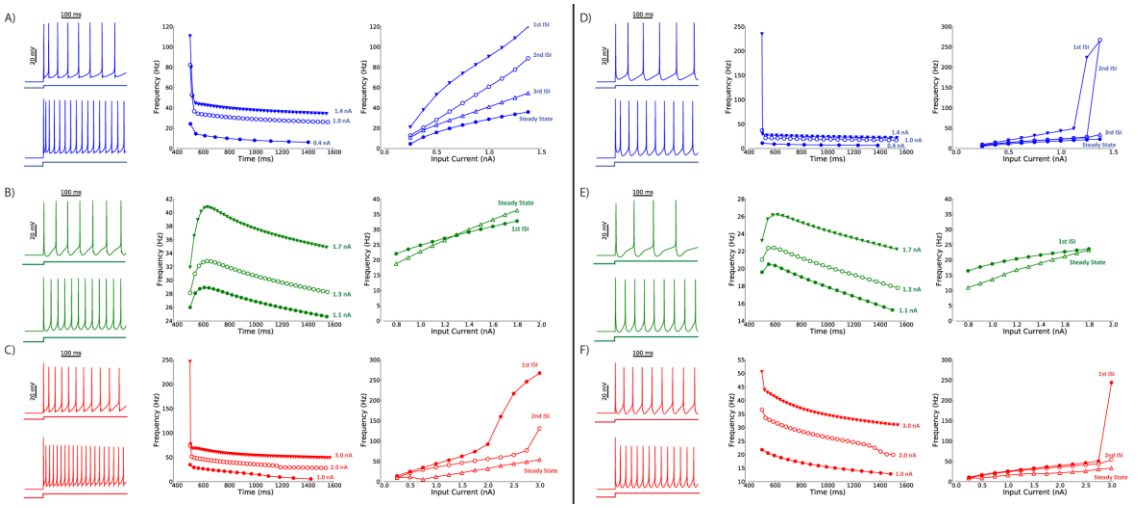

Figure 17: Depiction of Model Changes With Slower or Faster HVA Channel Conductance. Spike traces, firing frequency over time for select input currents, and firing frequency vs input current after a 0.75x (A,B,C) or 1.5x (D,E,F) change in HVA channel conductance time constants, A,D) neonatal HM, B,E) juvenile HM, and C,F) adult HM.

D7. Ca^{2+}-Related Parameter Families

For the reasons discussed at the beginning of this section, even though exact fitting is not a goal, knowing where various acceptable behaviors arise in parameter space is useful both in setting parameters, and understanding the degree in which the system can reasonably vary. Because many parameters are set based on biological findings, only a comparatively small number of parameters are open to exploration. Significant parameter variation is only reasonable where there exists a relative paucity of biological data. The exact capacity for microdomain buffering, and the conductance of HVA Ca^{2+} channels in the juvenile age range have the least support, and so the microdomain buffering parameter IW_m and the conductance for the HVA N-current are varied. Because each developmental age has its own requisite changes based on the literature, a separate parameter search is performed for each of the HM developmental age models (Figure 18).

The search itself involves replicating the simulations performed to produce Figure 10a for neonatal models, Figure 10c for juvenile models, and Figure 10e for adult models. This is then compared to biological data, where modified neonatal HM models are compared to Figure 10b, modified juvenile HM models are compared to Figure 10d, and modified adult HM models are compared to Figure 10e.

Topologically, distinct metrics for each of the developmental HM models is required to distinguish the nuanced differences between each age group while varying parameters. In neonatal HM models, linearity, non-overlapping, and sufficient spacing in the steady state, 1st ISI, 2nd ISI, and 3rd ISI curves on the *f* vs *I* plot are the primary test of suitability. Secondarily, the first ISI under a 1.4 nA input current must not deviate from biological data by more than 50 Hz, and the first ISI under a 1.0 nA input current must not deviate from biological data by more than 25 Hz. This is summarized in Figure 18a. In juvenile HM models, Type I or Type ID firing is absolutely required for consideration. In addition, during the adaptation exhibited in Type ID models, the model frequently

begins decaying at one slope, but changes to a secondary slope before the end of the simulation. This is not observed in the biological data, where the decay follows only one slope. When both decay slopes in model simulations are compared, if their respective slopes exceeds 15°, then the decay is deemed to be insufficiently linear. Steady state and 1st ISI curves on the *f* vs *I* plot must also not be parallel, as this is not seen in biological data, and the fAHP must not dip down as far as the mAHP. This is summarized in Figure 18b. In adult models, the defining feature is its high 1st ISI with an input of >2.0 nA. This high 1st ISI tends to either be present or entirely absent, and so if the 1st ISI is lower than biological data by 100 Hz, it is deemed absent. If this 1st ISI is below biological data by at least 25 Hz, it is considered present but insufficiently high. Nonlinearities in the 2nd ISI curve on the *f* vs *I* plot following the first few ISIs are not deemed acceptable, nor are abrupt shifts in firing frequency following the first few ISI on the *f* vs *t* plot. This is summarized in Figure 18c.

The grids given in Figure 18 give some indication that not only is there an appreciable amount of wiggle in certain Ca^{2+} parameters without losing acceptability in the model, but that aberrations in behavior tend to cluster together. There appears to be a very slight positive correlation between values for IW_m and I_N conductance that result in acceptable models. The biggest exception is the juvenile model, which displays what appears to be some measure of positive correlation, but loses its dependence on I_N conductance as IW_m is progressively reduced. Significantly more runs, however, would be required to mathematically confirm a positive correlation.

Given these parameter families, final parameters for IW_m and I_N conductance are chosen such that they both come close to the centroid of their respective families, while simultaneously representing the parameters yielding the closest fit to the biological data with respect to its neighbors.

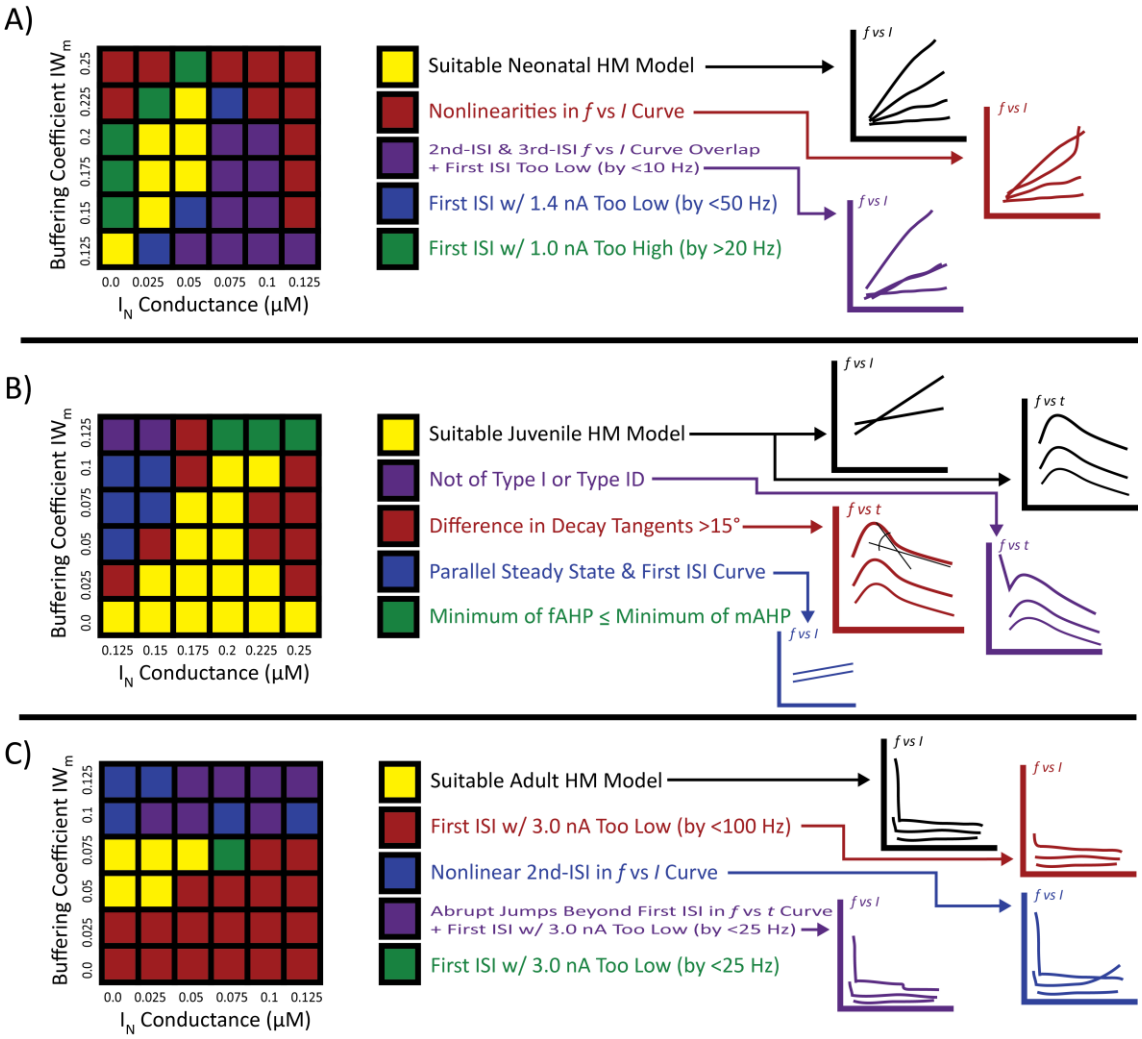

Figure 18: Ca^{2+} Mechanism Parameter-Space Exploration.
Exploration of parameter space for the A) neonatal HM model, B) juvenile HM model, and C) the adult HM model with respect to microdomain buffering and conductance in the HVA N-current, with all other parameters kept standard and fixed for each model. Each model type has its own criteria for acceptance, where each grounds for rejection is listed in its legend, ordered from most important at the top to least important at the bottom. Models that exhibit more than one criteria for rejection will be labeled with the more high priority issue.

E. Methods

E1. Measuring Spike Frequency

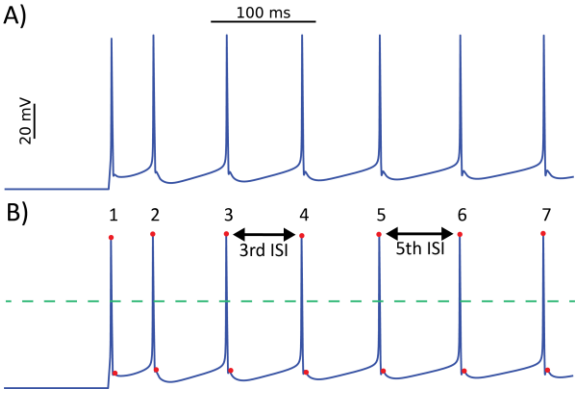

Figure 19: Determining Spike Frequency
A) Action potentials in the neonatal model in response to a square current pulse. B) Depiction of measuring firing frequency. Red dots represent local optima. All local optima above the green, dotted line are deemed spikes. Inter-spike intervals are calculated based on spike location.

Spike frequency for all models is measured with the same routine. First, local optima in the voltage trace are identified by taking the difference of every voltage data point V_t at time t with the voltage data point V_{t+1} at the subsequent time step $t+1$. Once this difference $\Delta V_t = V_{t+1} - V_t$ is computed at every time point t, the following check is made: if $\Delta V_t > 0$ and $\Delta V_{t+1} \leq 0$, then a local optima exists at time point t. Following this, a threshold is applied, such that for a local optima at time point t, if $V_t > -30$, then it is considered an action potential. Spike frequency is tabulated based on inter-spike interval (ISI) calculations; the frequency of the i-th action potential at time t_i is computed based on the time of the next action potential at t_{i+1} by the following equation:

$$ISI(i) = \frac{1}{t_{i+1} - t_i}$$

When t_i and t_{i+1} are measured in seconds, then this equation will have units in hertz. The process of determining firing frequency is summarized in Figure 19. Figures depicting firing frequency during STF and LTF simulations only report peak firing frequency per burst, for clarity.

E2. Simulated Glutamate and Serotonin Application

To simulate realistic excitatory glutamatergic rhythmic respiratory input to our HM models, we take the form of common medullary slice preparations, as described originally by (Smith et al 1991), and depicted in Figure 20. We apply an excitatory stimulus to our HM by modifying presynaptic voltage as detailed in the Models section. Glutamatergic presynaptic voltage is kept high for 1.1s, and removed for 5.9s before being applied again. Simulated drive is identical for all three developmental versions of the HM model, and remains constant in frequency throughout the duration of every simulation.

The intermittent application of 5-HT or hypoxia to induce LTF in biological experiments can vary greatly between species and experimental protocol. Common protocols in HMs and PMs include three bouts of 5 minute hypoxia spaced by 5 minutes without hypoxia (Baker-Herman & Strey 2011, McKay et al 2004), and three bouts of 3 minute hypoxia spaced by 5 minutes without hypoxia (Baker & Mitchell 2000, Bocchiaro & Feldman 2004). These biological experiments are frequently compared to a paradigm of continuous hypoxia that does not induce LTF, which can vary from 9 minutes (Bocchiaro & Feldman 2004) to 20 minutes (Baker & Mitchell 2000). Based on this, LTF simulations induced by intermittent application of simulated 5-HT in all three

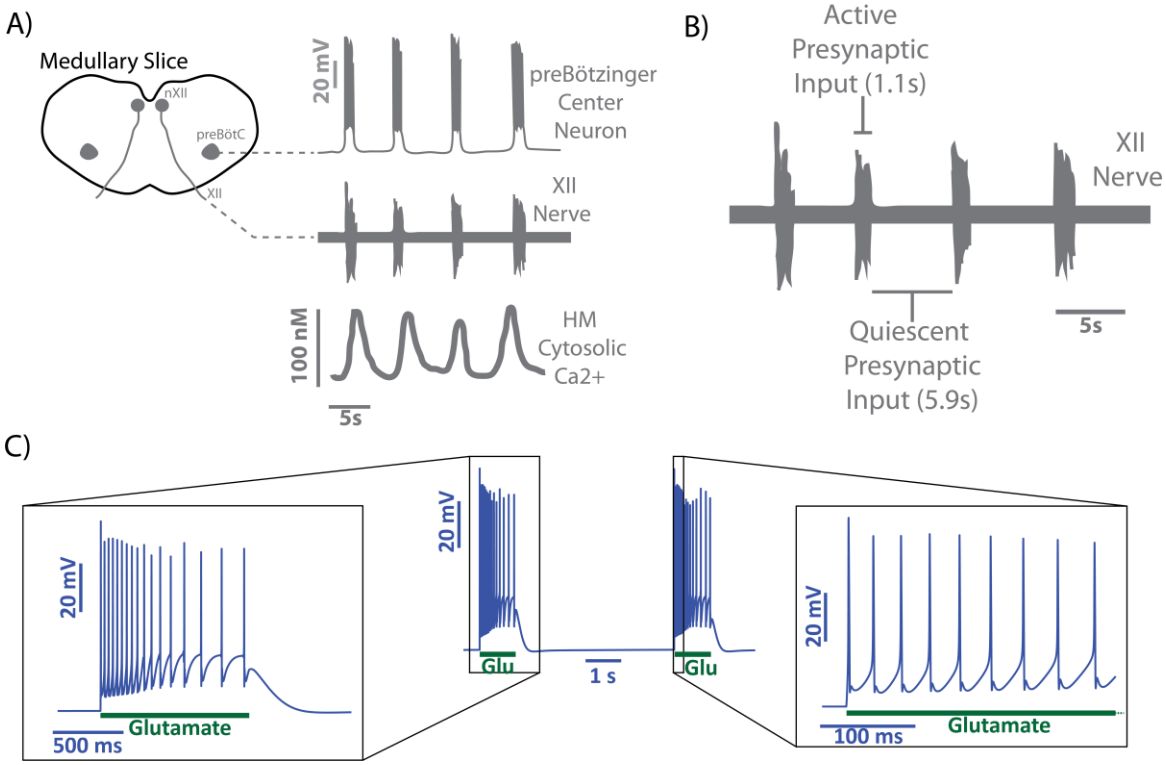

Figure 20: HM Excitatory Drive and Simiulated Application of Glutamate to the Model
The basis of presynaptic input to the model is shown here: A) a depiction of biological preBotC neural activity, biological XII nerve output, both adapted from Smith et al (1991), and input-driven Ca2+ oscillations in biological HM cytosol, adapted from Ladewig et al (2004). B) Measurements of XII nerve output to determine reasonable simulated glutamate application timing in the model, adapted from Smith et al (1991). C) Demonstration of two bursts from the adult HM model, with simulated glutamate applied as per the timing from B, and zoomed in two separate locations to enhance detail. This paradigm approximates natural glutamatergic input to HMs observed during medullary slice preparations.

developmental age group HM models receive three 4 minute bouts of simulated intermittent 5-HT starting 0.5 minutes within the simulation, with each spaced by 3 minutes of no 5-HT. Simulations receiving a continuous application of simulated 5-HT, which is not known to induce LTF, start simulated application of 5-HT at 0.5 minutes into the simulation, and continue for 18 minutes. Simulated application of 5-HT in STF-invoking simulations for all three developmental age group HM models begins simulated application of 5-HT 0.5 minutes into the simulation, and maintains this for 4 minutes.

Simulated application of 5-HT in cytosolic Ca^{2+} simulations begins starting at 40s, and continues until 90s.

E3. Simulated Pharmacology

To directly address the questions originally put forth in the Introduction, a series of simulation manipulations have been devised. Results from modeling work can serve as strong hypotheses for mechanisms that can be later tested in biological preparations. Even though this project is purely computational, and thus none of the results have been directly tested biologically, simulation findings are easier to verify experimentally when simulated manipulations closely model experimental paradigms. Thus the manipulations applied to the three developmental models take the form of simulated pharmacological experiments. It cannot be stressed enough, however, that unless otherwise specified, these simulated pharmacological manipulations exist purely within computational models, and should in no way be confused with actual biological preparations. The specific alterations to the model required to simulate these pharmacological effects are described below.

InsP3R blockade will be produced by making intracellular Ca^{2+} stores insensitive to changes in IP3 by removing buffering dependence on IP3 by setting the constant K_v to zero.

5-HT_2R blockade is modeled by making its associated G-coupled protein receptor $G_{\alpha q}$-GTP insensitive to 5-HT. This is performed by setting the constant k_{g2} to zero.

5-HT_{1A}R blockade is modeled similarly to 5-HT_2R, except instead of making $G_{\alpha q}$-GTP insensitive to 5-HT, we make G_i/G_0, the G-coupled protein associated with 5-HT_{1A}R, insensitive to 5-HT. This is accomplished via setting the constant k_{g1A} to zero.

I_h blockade, a rapid secondary effect of 5-HT_2R activation, is fulfilled by setting the constant c_h to zero.

PKC blockade can be used to distinguish between downstream effects of 5-HT_2R activation, such as changes to AMPAR production and conductance, and upstream effects, such as release of Ca^{2+} from InsP3R and I_h conductance reduction. In our models, we accomplish this simply by forcing [PKC] to be zero during the duration of simulated blockade.

MAPK separates AMPA phosphorylation from PKC from AMPAR upregulation. MAPK blockade is performed by forcing [MAPKK-PP] to zero for the duration of blockade.

It should be noted that unlike actual pharmacological agents, these simulated manipulations completely block their target, have no effect on similar receptors or receptor subtypes, and start or cease action immediately upon the application or removal of the given manipulation.

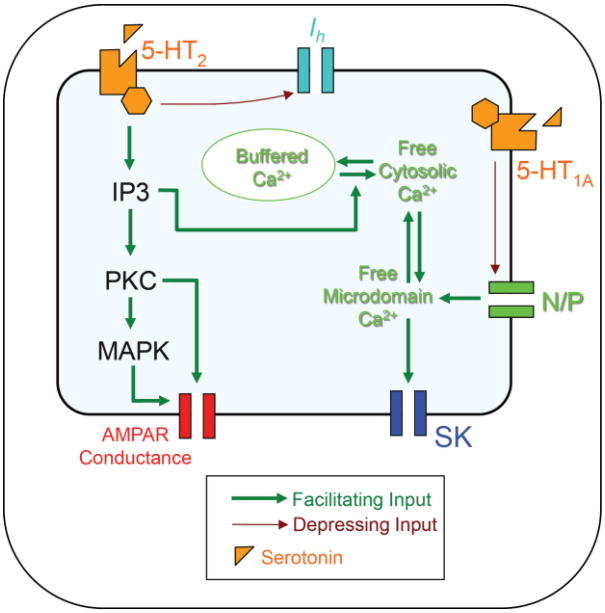

Figure 21: Simplified Secondary Messenger Diagram.
Description of all major affected outputs to the system starting from serotonergic inputs.

With a description of how each simulated pharmacological manipulation can be obtained, we proceed with a description of how the hypotheses set forth in the specific aims will be addressed. To aid in the description of precise manipulations to be taken, a simplified version of Figure 7 has been generated to clarify the exact pathways involved in each simulation (Figure 21). It should be noted that the model itself has not been simplified, and that this is simply for clarity of description. The exact manipulations taken for each of the specific aims is discussed sequentially below, with a corresponding modified version of Figure 21, along with the hypotheses addressed by these manipulations.

E4. 5-HT Application and Cytosolic Ca^{2+}

Both an increase in baseline Ca^{2+} and a decrease in Ca^{2+} spike size can be observed in biological imaging experiments of cytosolic Ca^{2+} during 5-HT application. In order to disambiguate the mechanisms involved, the simulation of several of the aforementioned simulated blockades are tested in the model. As per the previously outlined hypotheses, the primary goal is in confirming or refuting that low frequency Ca^{2+} changes in the model, a slow increase in baseline Ca^{2+}, is the result of 5-HT_2R activation, and that high frequency changes in the model, the decrease in Ca^{2+} spike size, is the result of HVA Ca^{2+} channel inhibition by 5-HT_{1A}R. In all of the subsequent simulated experiments described in this section, each model is run for a total of 90s of simulated time to allow sufficient time to establish both baseline equilibrium behavior and come to a new equilibrium after simulated 5-HT application. Simulated 5-HT and glutamate are applied as described above. Simulated blockades, when applicable, are performed from 0s to 90s. Prior to recording all simulations are run until behavior is periodically stable, and all other parameters are as previously defined unless otherwise specified. Exact manipulations are described as follows.

The basic simulated application of 5-HT is tested in all three developmental HM models to demonstrate reasonable behavior in each model, and clearly highlight any developmental differences that may exist. Following this, questions and aims are addressed directly.

The two potential mechanisms for a low frequency increases in cytosolic Ca^{2+} in our models are given in Figure 22. To test whether or not 5-HT_2R plays a role through InsP3R mediated Ca^{2+} release, simulated block of IP3's ability to activate InsP3R was performed. To test whether an increase in firing frequency could be increasing cytosolic Ca^{2+} by increased flow of Ca^{2+} into microdomains, a simulated block of 5-HT_{1A}R was performed to remove its capacity for indirectly activating SK channels, and separately perform a simulated block of 5-HT_2R to eliminate the effect of potential changes to AMPAR.

Because transient rises and falls in cytosolic Ca^{2+} are implicated to be caused by each individual burst of the HM, putative high frequency changes in Ca^{2+} are

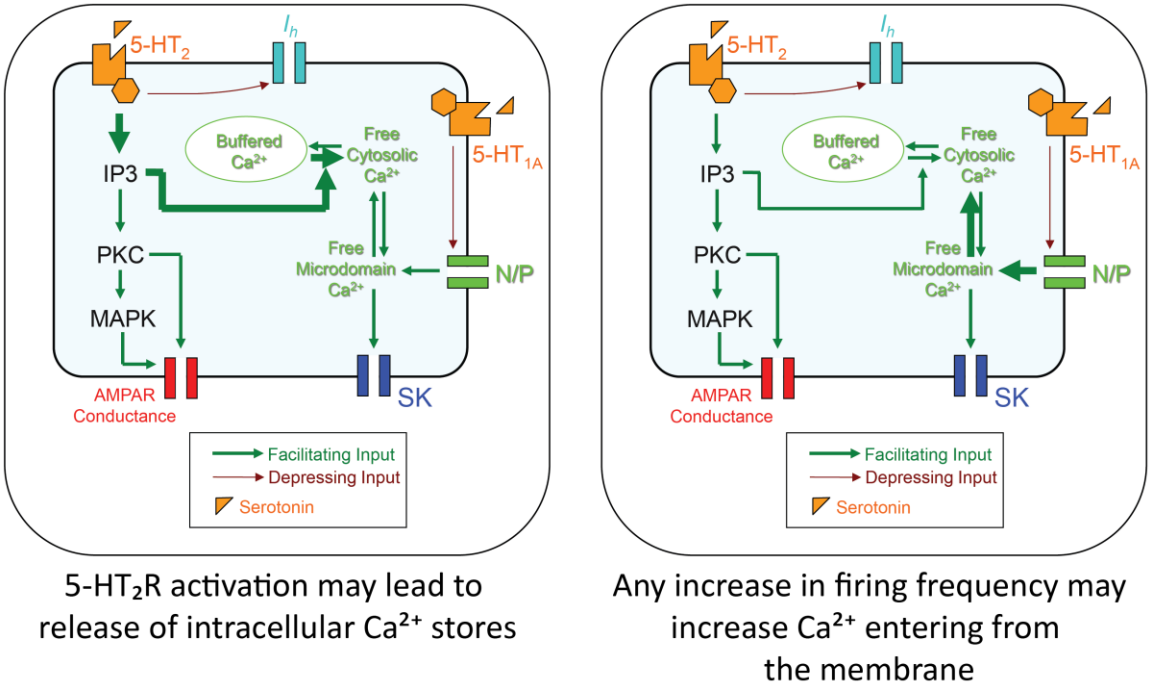

Figure 22: Potential Mechanisms For Cytosolic Ca^{2+} Increase.
Our main hypothesis for low frequency changes to cytosolic Ca^{2+} is that 5-HT_2R activation can lead to a release of intracellular Ca^{2+} stores via IP3 activation of InsP3R. An alternative explanation may be that increases in firing frequency could bring additional Ca^{2+} into the Ca^{2+} microdomains, where Ca^{2+} would then diffuse into the cytosol. 5-HT is known to increase firing frequency, and may potentially do so either through 5-HT_2 potentiation of AMPAR, or 5-HT_{1A} activation of SK channels.

hypothesized to be produced through changes to microdomain Ca^{2+}. The two potential mechanisms for high frequency increases in cytosolic Ca^{2+} are given in Figure 23. To test whether or not 5-HT_{1A}R have a role in reducing microdomain Ca^{2+}, we perform a simulated block of 5-HT_{1A}R. To test whether Ca^{2+} released from intracellular stores could diffuse into microdomains and activate SK channels, inhibiting voltage-gated Ca^{2+} channels by reducing membrane conductance, a simulated block of InsP3R was performed.

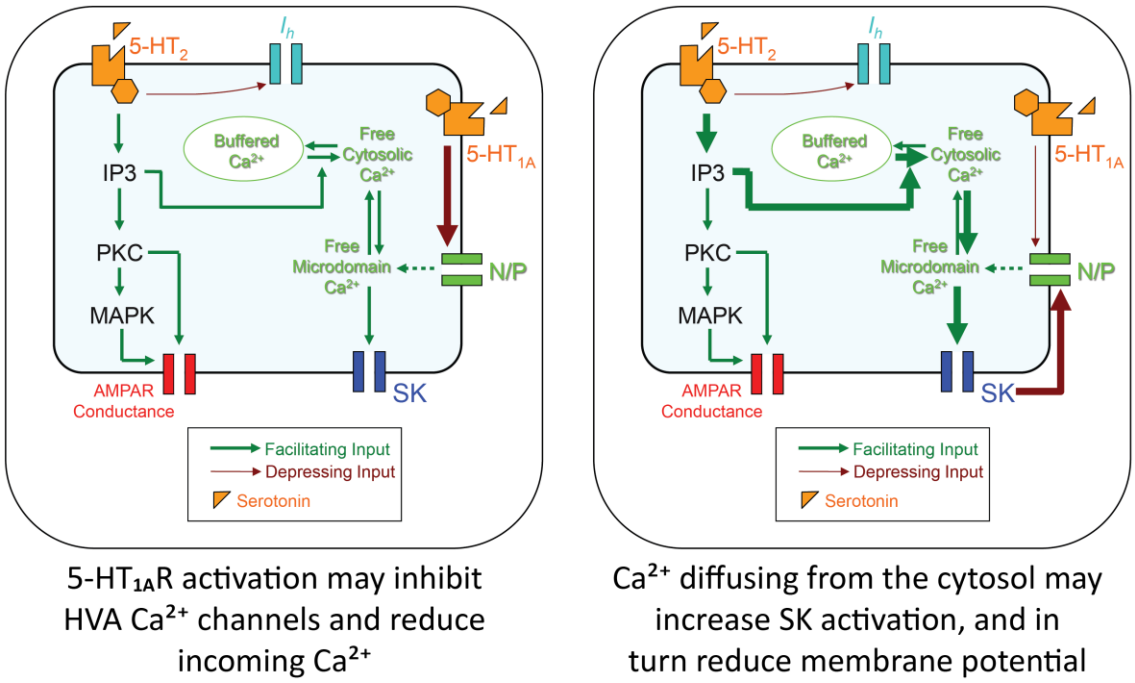

5-HT$_{1A}$R activation may inhibit HVA Ca^{2+} channels and reduce incoming Ca^{2+}

Ca^{2+} diffusing from the cytosol may increase SK activation, and in turn reduce membrane potential

Figure 23: Potential Mechanisms For Microdomain Ca^{2+} Increase.
We hypothesize that high frequency changes to cytosolic Ca^{2+} are caused by individual bursts of the HM, and therefore are predominantly caused by changes to Ca^{2+} entering the microdomains from voltage-gated Ca^{2+} channels. Our main hypothesis for high frequency Ca^{2+} changes is that 5-HT$_{1A}$R can inhibit HVA Ca^{2+} channels, mitigating the quantity of Ca^{2+} flowing to the microdomains. An alternate explanation is that Ca^{2+} released from intracellular stores diffuses into the microdomains, activates SK, and in turn inhibits voltage-gated Ca^{2+} channels indirectly via reduction of overall cell voltage.

E5. 5-HT Application and STF

While the application of 5-HT in biological preparations generally evokes an excitatory short-term response, part of this potentiation can persist transiently beyond the removal of 5-HT. It is currently not known what the physiological correlates of these behaviors are. To aid in clarifying the potential mechanisms that might implicate certain mechanisms as responsible for specific effects, a series of simulated blockades are performed. As per the hypotheses, the primary interest is in confirming or refuting that potentiation in the model associated with simulated 5-HT application is the result of 5-HT$_{1A}$R inhibition of HVA Ca^{2+} channels, and that transient potentiation in the model after the simulated application of 5-HT is the result of phosphorylation of AMPAR. In all of the subsequent simulated experiments described in this section, each model is run for a total of 8 minutes of simulated time to allow sufficient time for the system to respond to simulated 5-HT, and come back to baseline following its removal. Simulated 5-HT and glutamate are applied as described above. Simulated blockades, when applicable, are performed from 0 minutes to 8 minutes. Prior to recording all simulations are run until behavior is periodically stable, and all other parameters are as previously defined unless otherwise specified. Exact manipulations are described as follows.

The basic simulated application of 5-HT is tested in all three developmental HM models to demonstrate reasonable behavior in each model, and clearly highlight any developmental differences that may exist. Following this, questions and aims are addressed directly.

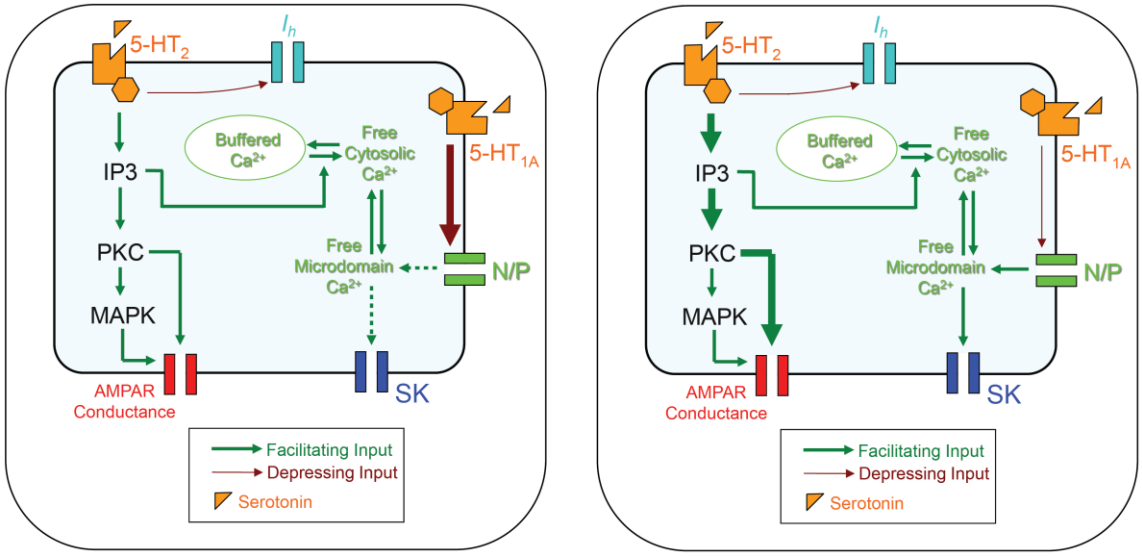

Figure 24: Potential Mechanisms For STF.
Our main hypothesis is that STF is caused by a 5-HT_{1A}R mediated inhibition of HVA Ca^{2+} channels, which in turn inhibits SK channels, and increases overall firing rate in the HM model. An alternate explanation is that 5-HT_2R activation results in PKC phosphorylation of AMPAR, which increases its conductance and potentiates the HM model.

The putative mechanisms underlying STF are given in Figure 24. To test whether 5-HT_{1A}R can indirectly inhibit SK channels via reduction of HVA Ca^{2+} conductance in the model, a simulated blockade of 5-HT_{1A} was performed. To test whether 5-HT_2R appreciably increase AMPAR conductance via direct phosphorylation by PKC during the simulated application of 5-HT in the model, but not necessarily after, a simulated block of 5-HT_2 was performed.

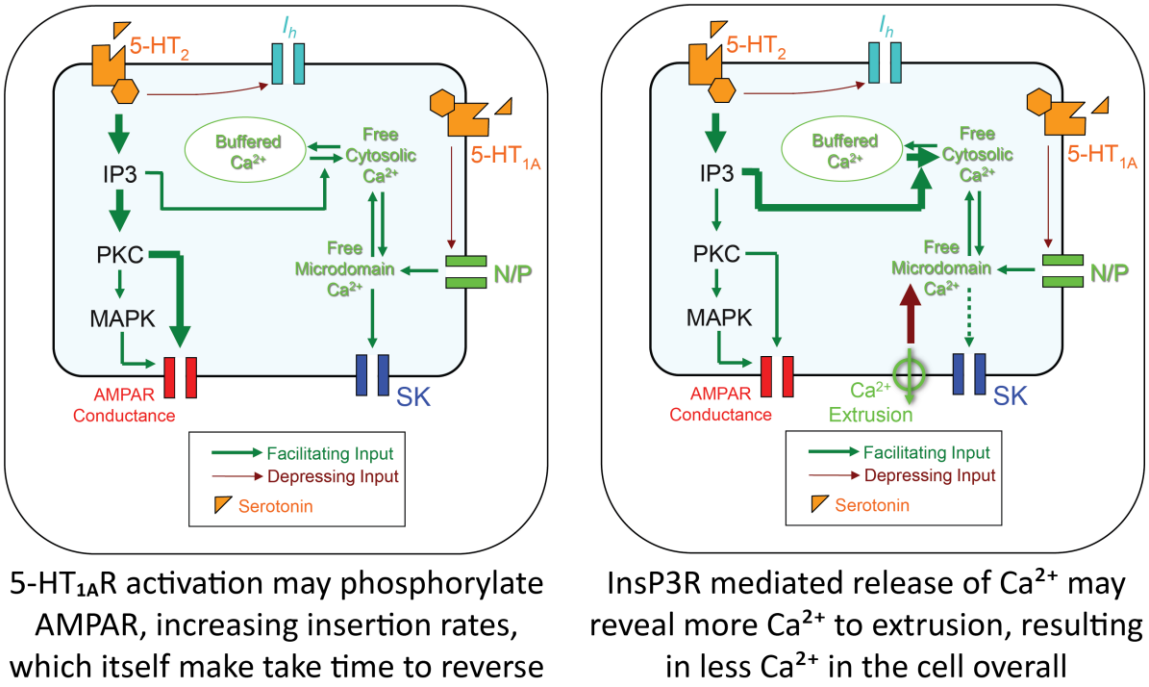

5-HT$_{1A}$R activation may phosphorylate AMPAR, increasing insertion rates, which itself make take time to reverse

InsP3R mediated release of Ca^{2+} may reveal more Ca^{2+} to extrusion, resulting in less Ca^{2+} in the cell overall

Figure 25: Potential Mechanisms For STF Transient.
Our main hypothesis is that the transient potentiation following STF is the product of 5-HT$_2$R mediated PKC phosphorylation of AMPAR, which would potentiate the HM model. An alternate explanation has cytosolic stores of Ca^{2+} depleted by lengthy 5-HT$_2$ activation, which in turn leaves more Ca^{2+} to potentially be removed via extrusion mechanisms. This may result in an overall reduced amount of Ca^{2+} in the cell, which would inhibit SK channels, and result in potentiation of the HM model.

Even after the removal of 5-HT, part of the STF potentiation persists for a short period of time. The putative mechanisms for this are given in Figure 25. To test whether PKC phosphorylation of AMPAR is responsible for a transient post-STF potentiation, a block of 5-HT$_2$R was performed, in addition to a block of PKC itself. To test whether a release of Ca^{2+} from intracellular stores, and an ultimate drop in intracellular Ca^{2+} is responsible for a transient post-STF potentiation, a block of InsP3R was performed.

E6. 5-HT Application and LTF

LTF is known to occur in various motoneurons, respiratory circuits, and the whole animal. It is also been hypothesized that a critical period in a number of respiratory-related brainstem areas may exist (Liu & Wong-Riley 2008, Liu & Wong-Riley 2010a, Liu & Wong-Riley 2010b, Wong-Riley & Liu 2008), where numerous ion channels change their density abruptly. We hypothesize that the changes during this critical period may be disruptive to LTF, and in turn test this in the developmental HM models by applying 5-HT and glutamate as noted previously. To test this, an LTF paradigm of three simulated 5-HT pulses, each lasting 4 minutes, with 3 minutes in between each pulse, will be applied to each of the three HM developmental models, over the course of a simulated experiment lasting one hour of simulated time.

While PKC is implicated in the initiation of LTF in biological experiments, the underlying mechanisms governing initiation and maintenance of LTF in the HM are not fully understood. Putative mechanisms governing maintenance are given in Figure 26. To

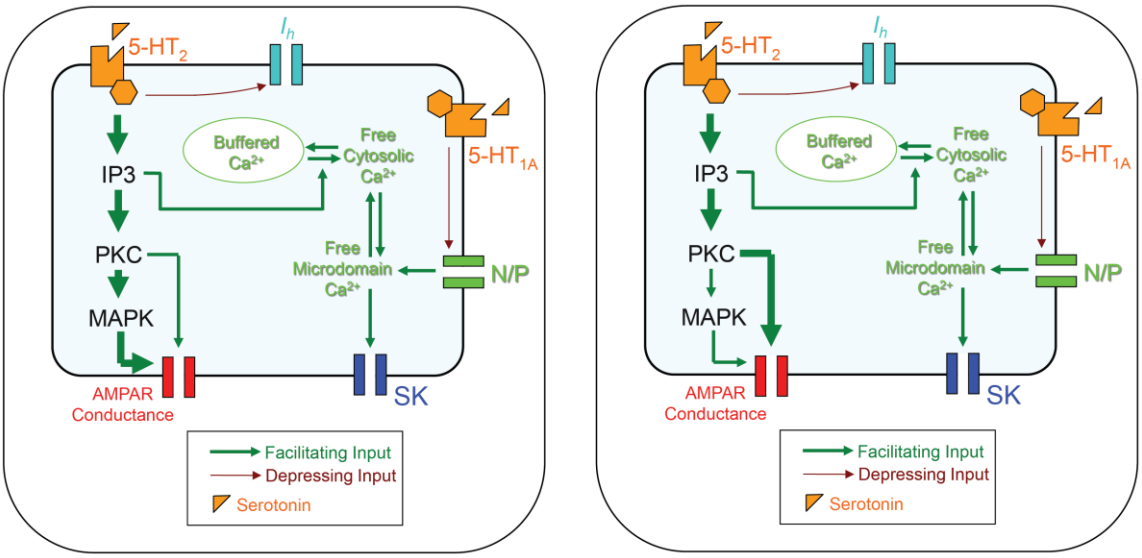

Figure 26: Potential Mechanisms For LTF Maintenance.
Our main hypothesis is that maintenance of LTF is governed by 5-HT$_2$R activation of MAPK, which results in an upregulation of AMPAR transcription. An alternative explanation is that direct phosphorylation of AMPAR by PKC, which increases insertion rates for AMPAR into the membrane, lasts sufficiently long to maintain LTF.

test whether MAPK upregulation of AMPAR is responsible for the maintenance of LTF through AMPAR upregulation in the model, a simulated block of MAPK will be applied during and/or after the simulated application of intermittent 5-HT in the following three paradigms: MAPK will be blocked starting at 0 minutes and ending at 30 minutes, MAPK will be blocked starting at 0 minutes and ending at 60 minutes, MAPK will be blocked starting at 40 minutes and ending at 60 minutes. To test whether PKC phosphorylation of AMPAR is responsible for the maintenance of LTF in the model, a simulated block of PKC will be applied during and/or after the simulated application of intermittent 5-HT with a timing identical to the three paradigms just discussed for simulated MAPK block. All simulated MAPK block and simulated PKC block simulations will be run for 60 minutes total, regardless of the actual start and stop times of their respective blockades.

F. Results

F1. 5-HT Application and Cytosolic Ca^{2+}

Since Ca^{2+} plays a central role in shaping firing frequency, an investigation of cytosolic Ca^{2+} levels, which change substantially with 5-HT application, is important in understanding the HM response to external stimulation. Within this section, differences between the three developmental HM models are reported, in addition to simulated blockade manipulations to the adult HM model to better understand: 1) baseline/low frequency changes in cytosolic Ca^{2+}, and 2) Ca^{2+} spikes/high frequency changes in cytosolic Ca^{2+}.

F1.a Developmental Differences

5-HT application in both neonate and adult HM models generates an increase in cytosolic Ca^{2+}, whereas in the juvenile HM model it leads to a decrease in cytosolic Ca^{2+} (Figure 27). In addition, the size of each Ca^{2+} spike in the adult HM model is half the size of its juvenile and neonatal counterparts, and after simulated 5-HT application, adult Ca^{2+} spikes decrease more dramatically in size.

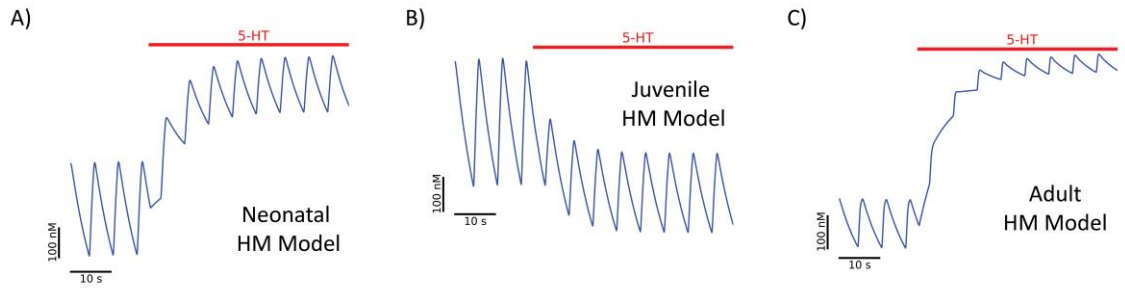

Figure 27: Developmental Differences in Cytosolic Ca^{2+} During Simulated 5-HT Application.
Depiction of Cytosolic Ca^{2+} during the simulated application of 5-HT in A) the neonatal HM model, B) the juvenile HM model, and C) the adult HM model. Each periodic rise of Ca^{2+} is the result of a burst of the HM model bringing in Ca^{2+} through voltage-gated Ca^{2+} channels.

F1.b Removal of Baseline Ca^{2+} Rise

When InsP3R is blocked in the adult HM model, we immediately see a complete negation of the rise in baseline Ca^{2+} (
Figure **28**b). Instead, the rise is replaced by a mild depression of baseline Ca^{2+}. A reduction in the loss of Ca^{2+} spike height is observed, but the reduction does not account for all loss of Ca^{2+} spike height. With HVA Ca^{2+} channels still inhibited by simulated 5-HT application, a decrease in Ca^{2+} spike height is still observed.

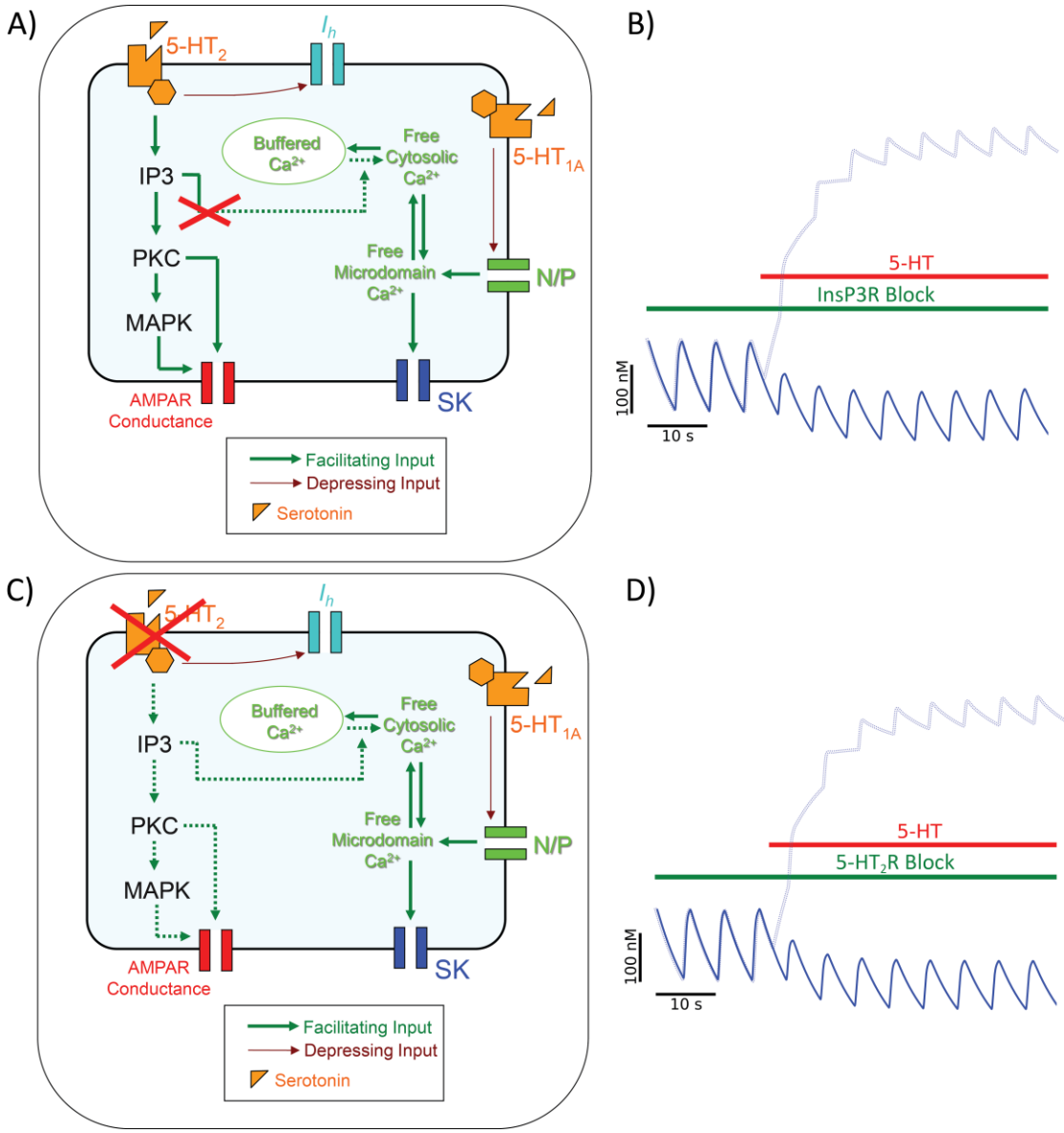

Figure 28: Mitigation of Baseline Cytosolic Ca^{2+} Rise.
The baseline rise in cytosolic Ca^{2+} can be eliminated in its entirety by either the simulated blockade of InsP3R or 5-HT_2R. A) InsP3R block only stops release of Ca^{2+} from intracellular stores, and B) eliminates cytosolic Ca^{2+} rise with simulated 5-HT application. C) 5-HT_2R block inhibits both release of Ca^{2+} from intracellular stores and modifications to AMPAR, and D) eliminates cytosolic Ca^{2+} rise with simulated 5-HT application. In both B and D, a simulation without any simulated blockade is added in as a faint dotted line for comparison.

Rather than directly antagonize InsP3R, we may instead inhibit upstream reactions by simulated blockade of 5-HT_2R. This helps to eliminate the possibility of downstream effects from PKC pathways beyond increasing IP3 levels. Upon simulated 5-HT_2R block (
Figure **28**d), near identical results are obtained when compared with simulated InsP3R blockade (

Figure **28**b), ruling out the role of AMPAR in baseline cytosolic Ca^{2+} increase and cytosolic Ca^{2+} spike height in the model.

F1.c Mitigation of Ca^{2+} Spike Reduction

While simulated inhibition of InsP3R mitigates baseline changes in Ca^{2+} in the model, 5-HT also affects voltage-gated Ca^{2+} channels. By simulated $5HT_{1A}R$ blockade, (Figure **29**), we see a retention and slight magnification of the change in baseline Ca^{2+}, presumably due to continual flow of Ca^{2+} from uninhibited voltage-gated Ca^{2+} channels. This is concomitant with a subsequent mitigation of Ca^{2+} spike height reduction by simulated 5-HT, which is to be expected as this simulated experiment has the highest levels of cytosolic Ca^{2+}. That Ca^{2+} spike height is reduced at all implicates elevated levels of Ca^{2+} in membrane microdomains, since conductance through voltage-gated Ca^{2+} are unchanged in this particular simulated experiment.

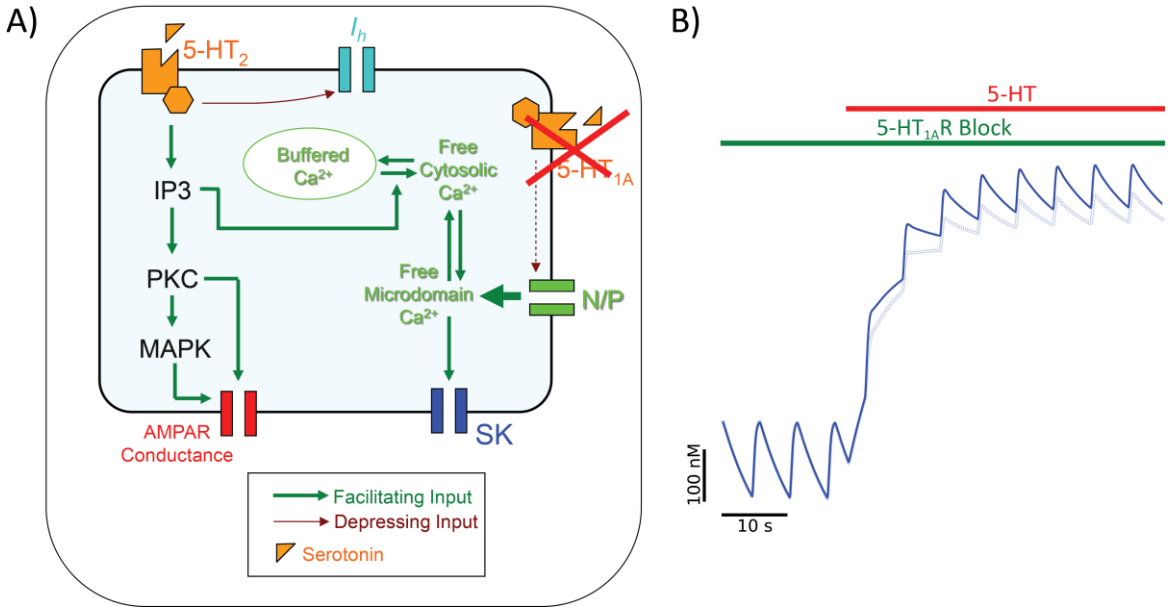

Figure 29: Mitigation of Cytosolic Ca2+ Spike Size Depression.
The depression of Ca^{2+} spike size can be mitigated but not entirely eliminated by the simulated block of 5-$HT_{1A}R$. A) 5-$HT_{1A}R$ block releases HVA Ca^{2+} from 5-$HT_{1A}R$ mediated inhibition, and B) mitigates the reduction of cytosolic Ca^{2+} spike height with simulated 5-HT application. In B, a simulation without any simulated blockade is added in as a faint dotted line for comparison.

F1.d Summary of Results

Based on these simulations, both simulated 5-HT_2R and InsP3R blockade will remove the baseline rise in Ca^{2+}. The only pathway these two blocks share in common are InsP3R mediated release of Ca^{2+} from intracellular stores. Therefore, this is the likely source of the cytosolic Ca^{2+} rise. The reduction in Ca^{2+} height was mitigated in all simulated blockade simulations, and so both 5-$HT_{1A}R$ and InsP3R mediated release of intracellular Ca^{2+} stores can be seen as responsible for Ca^{2+} spike height modification. A summary of effects is given in Figure 30.

Quantification of the three simulated experiments performed in this section can be found below. Notice the close similarities, but non-identical nature of simulated InsP3R block vs. 5-HT_2R block. Also note that simulated application of these blockers can have a mild but detectable effect on Ca^{2+} spike height prior to simulated 5-HT application. Finally, observe that Ca^{2+} spike height is not readily modulated by a single process, but affected by both InsP3R and voltage-gated Ca^{2+} dynamics in distinct ways.

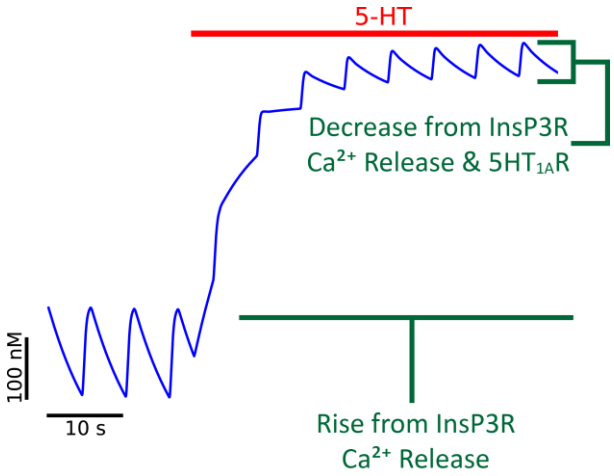

Figure 30: Summary of Causes For Cytosolic Ca^{2+} Related Effects.
The rise in baseline Ca^{2+} in the model is caused by release of Ca^{2+} from intracellular stores. The mitigation of Ca^{2+} spike height in the model is caused by both InsP3R mediated Ca^{2+} release and 5-HT_{1A}R inhibition of HVA Ca^{2+} channels.

Table 1: Quantification of 5-HT Application on Ca2+ Spike Height on Different Developmental Models.

Developmental Age	Ca^{2+} spike height before 5-HT (nM)	Ca^{2+} spike height after 5-HT (nM)	Ca^{2+} spike height change (nM)	Ca^{2+} spike height % change	Ca^{2+} baseline change (nM)
Adult	149.11	54.60	94.51	-63.4%	542.27
Juvenile	380.08	237.42	142.66	-37.8%	-143.57
Neonate	321.22	192.68	128.54	-40.0%	494.47

Table 2: Quantification of 5-HT Application on Ca2+ Spike Height Plus a Simulated Blockade.

Simulated Blockade	Ca^{2+} spike height before 5-HT (nM)	Ca^{2+} spike height after 5-HT (nM)	Ca^{2+} spike height change (nM)	Ca^{2+} spike height % change	Ca^{2+} baseline change (nM)
None	149.11	54.60	94.51	-63.4%	542.27
InsP3R	149.2	106.5	42.6	-28.6%	-62.7
5-HT_2R	150.6	104.2	46.4	-30.8%	-64.4
5-HT_{1A}R	151.2	87.2	64.1	-42.4%	587.8

F2. 5-HT Application and STF

The short-term response to hypoxia itself is complex and multifaceted. Here we deconstruct the various contributors to this phenomenon. Within this section, differences between the three developmental HM models are reported, in addition to 1) simulations addressing the mechanisms driving STF, and 2) transient STF-like behavior.

F2.a Developmental Differences

As in the cytosolic Ca^{2+} response to simulated 5-HT application, both the neonate and adult behave similarly: both exhibit a rapid rise in firing frequency, a sudden drop, and then a slower rise. In comparison, the juvenile model lacks the drop in firing frequency but maintains the slight rise during STF, but lacks any post-STF potentiation (Figure 31). Upon cessation of simulated 5-HT application, firing frequency drops below baseline levels very briefly, and then quickly rises above baseline before coming back down in both neonate and adult, but not juvenile, which mostly returns to baseline. The post-5-HT drop in firing frequency is appreciably larger in the neonatal model than the adult, as is the post-5-HT rise in firing frequency, and baseline firing frequency in general. Topologically, however, the adult and neonatal HM models fundamentally respond the in the same fashion to 5-HT application.

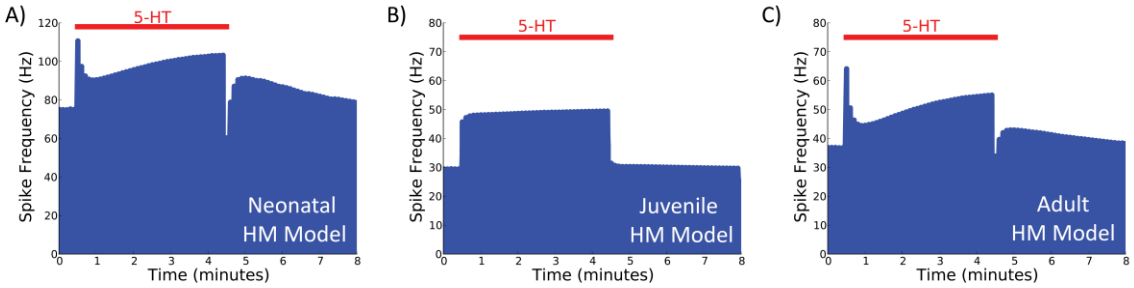

Figure 31: Developmental Differences in STF During Simulated 5-HT Application.
Depiction of STF through plots of HM peak firing frequency per burst during the simulated application of 5-HT in A) the neonatal HM model, B) the juvenile HM model, and C) the adult HM model.

F2.b Modifications to STF

Simulated applied 5-HT generates an increase in excitability in all three developmental HM models. With the simulated block of 5-HT_{1A}R, however, this increase in excitability is entirely stymied, with a slight inhibition present in the place of a potentiation (

Figure **32**). The post-STF potentiation is not affected by simulated 5-HT_{1A}R block, and therefore likely is governed by distinct mechanisms. Subsequently this implies that the majority of the STF response in the model is governed by 5-HT_{1A}R.

STF from simulated 5-HT application rapidly dips and recovers through the application of 5-HT in both the neonatal and adult HM models. However, under a simulated blockade of InsP3R, rather than a dip, firing frequency simply climbs throughout the simulation while 5-HT is applied. Subsequently, this does not remove post-STF potentiation. It does, however, remove any "rebound" suppression of firing frequency immediately following the removal of 5-HT. Subsequently, this implicates the rise in cytosolic Ca^{2+} for the early dip in STF (
Figure **32**).

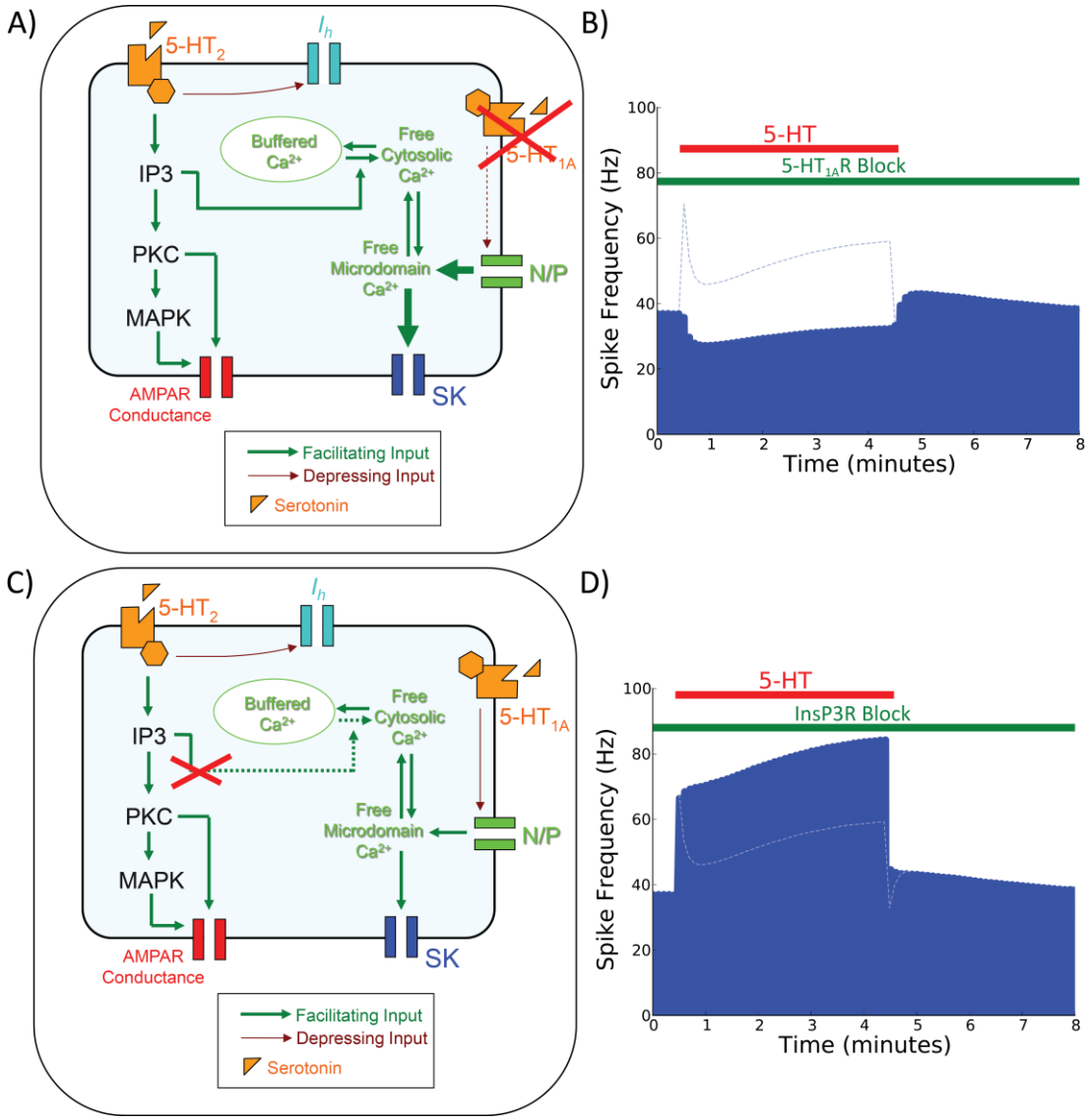

Figure 32: Removal and Enhancement of STF.
The immediate potentiation from simulated 5-HT application can be either eliminated or enhanced depending on the simulated blockade applied. A) 5-HT_{1A}R block inhibits HVA Ca^{2+} channels, and B) eliminates STF in its entirety with simulated 5-HT application. C) InsP3R block inhibits release of Ca^{2+} from intracellular stores, and D) eliminates a dip in excitability during STF, resulting in a larger overall STF response. In both B and D, the response from a simulation without any simulated blockade is added in as a faint dotted line for comparison in areas where there exists a significant discrepancy. Spike frequency here refers to the peak firing frequency for each burst.

F2.c Removal of post-STF potentiation

Following the application of 5-HT in the model, a brief potentiation of the HM persists beyond the removal of the 5-HT stimulus. This transient memory of STF rapidly

fades on its own, but can be removed altogether in the model through simulated block of either 5-HT_2R or simulated block of PKC (
Figure **33**). Both simulated blockades share modifications to AMPAR in common. A blockade of MAPK (not shown) has no discernible effect on STF or the post-STF potentiation, and so phosphorylation of AMPAR via PKC is implicated as the cause of this transient rise.

In addition to post-STF potentiation, a similar phenomenon occurs during STF itself, where a steady rise of potentiation in the model commences shortly after the simulated application of 5-HT. This rise itself is only present with the post-STF potentiation, and only eliminated when the post-STF potentiation is eliminated (
Figure **32**,
Figure 33). Because of this, this steady rise in potentiation during STF is likely an AMPAR phosphorylation mediated behavior, and can be viewed as the "wind-up" for the post-STF potentiation "wind-down" in excitability.

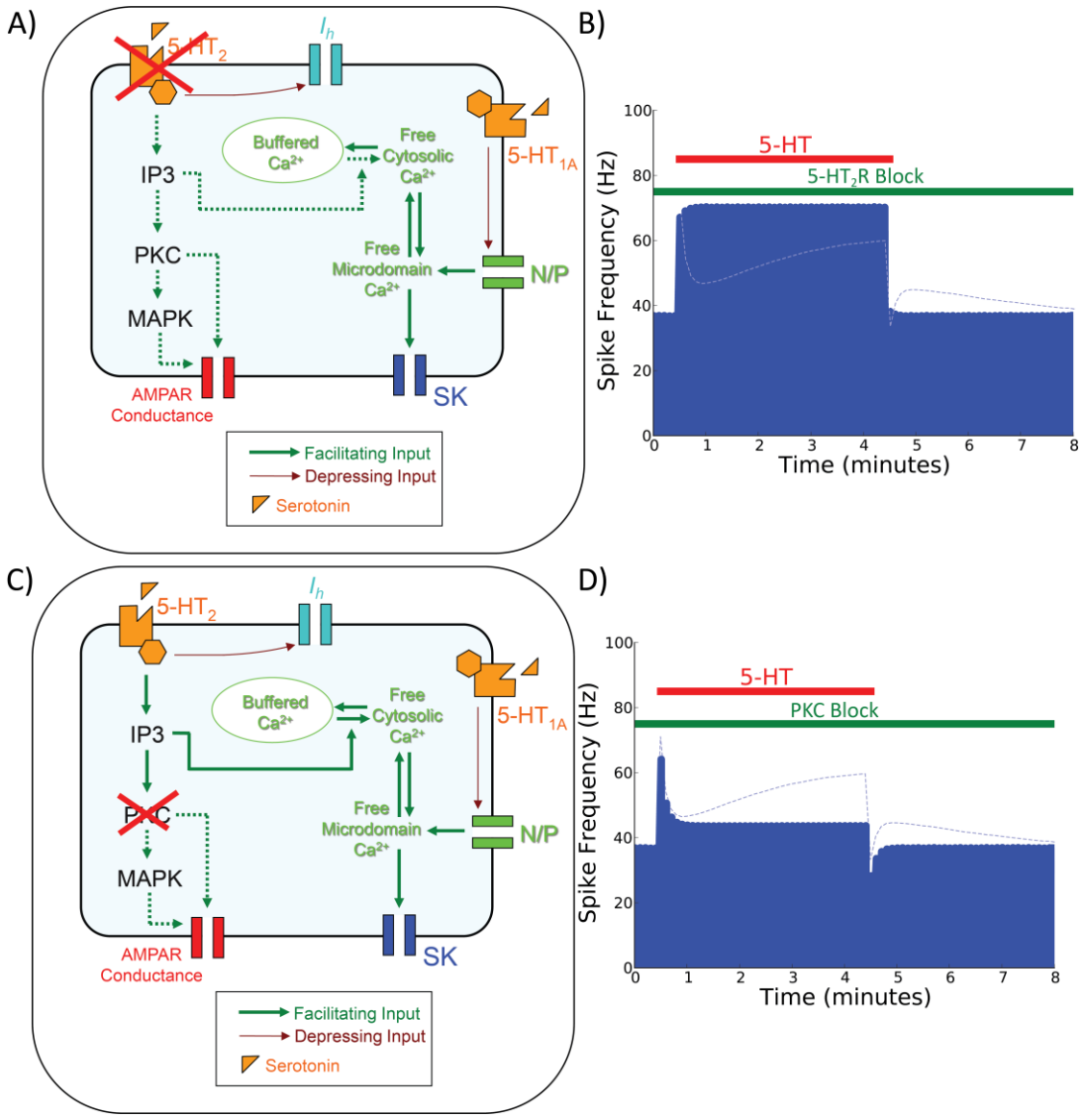

Figure 33: Removal of Post-STF Potentiation and Rise in Potentiation During STF.
The post-STF potentiation from 5-HT application in the model can be eliminated through two distinct simulated blockades, and is eliminated in tandem with a rise in potentiation during STF. A) 5-HT_2R block inhibits both release of Ca^{2+} from intracellular stores and modifications to AMPAR, and B) eliminates post-STF potentiation during simulated 5-HT application, and eliminates rising potentiation during STF through the removal of an early drop in excitability. C) PKC block inhibits modifications to AMPAR, and D) eliminates post-STF potentiation during simulated 5-HT application, and eliminates rising potentiation during STF without removing the early drop in excitability. In both B and D, the response from a simulation without any simulated blockade is added in as a faint dotted line for comparison in areas where there exists a significant discrepancy. Spike frequency here refers to the peak firing frequency for each burst.

F2.d Summary of Results

Given these simulations, simulated 5-HT_{1A}R block will remove STF in its entirety, and so the cause of most of the LTF response resides in 5-HT_{1A}R inhibition of HVA Ca^{2+} channels. In comparison, the post-STF potentiation seen in the neonatal and adult HM model can be removed either through simulated 5-HT_2R block or simulated PKC blockade, implicating AMPAR machinery as the primary culprit for this behavior. Specifically phosphorylation of AMPAR via PKC. Additionally, a steady rise in excitability during the simulated application of 5-HT is also affected by simulated 5-HT_2R or PKC block, and so this can be considered an extension of the post-STF potentiation that begins before simulated 5-HT application is removed. Specifically, a steady rise in AMPAR mediated excitability begins shortly after the application of simulated 5-HT, and steadily dissipates once it is removed. A InsP3R dependent decrease in excitability also occurs very rapidly after the simulated application of 5-HT in the model, and very rapidly after its removal. The removal, in particular, generates a very short-lived inhibition of excitability that occasionally appears in the biological literature on HM LTF. All of these effects are qualitatively summarized in Figure 34

Quantification of the aforementioned experiments can be found below. Note that Δf implies a change of frequency with relation to the baseline frequency, which itself is defined as the steady state frequency of each burst. Since the juvenile model was convex under the application of 5-HT, no minimal frequency was calculated. Because this section focuses more on behavioral properties than developmental changes, experiments involving blockers were performed on the adult HM model only, to mitigate redundancy.

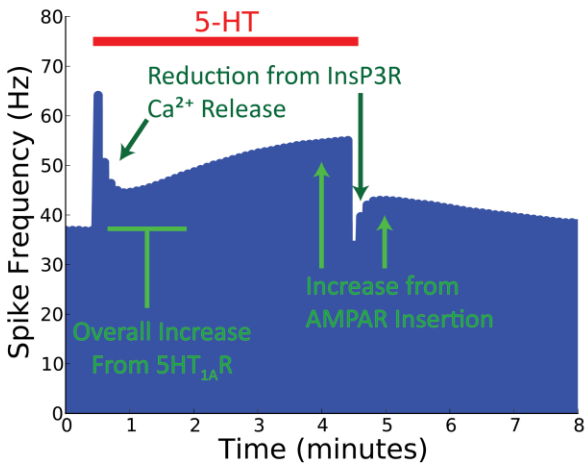

Figure 34: Summary of Causes For STF Related Effects.
STF is primarily the result of 5-HT_{1A}R inhibition of HVA Ca^{2+} channels. The steady increase in excitability during simulated application of 5-HT and subsequent decrease in excitability following the removal of simulated 5-HT is driven by PKC phosphorylation and increased insertion of AMPAR into the membrane. Decreases in excitability early in the application of 5-HT and shortly after the removal of 5-HT are driven by InsP3R mediated release of Ca^{2+} from intracellular stores. Spike frequency here refers to the peak firing frequency for each burst.

Table 3: Quantification of 5-HT Application on STF on Different Developmental Models.

Developmental Age	Baseline *f* (Hz)	Initial Δ*f* With 5-HT (Hz)	Minimal Δ*f* With 5-HT (Hz)	Final Δ*f* With 5-HT (Hz)	Initial Δ*f* After 5-HT (Hz)	Max Δ*f* After 5-HT (Hz)
Neonatal	75.08	+35.54	+15.26	+28.12	-14.76	+16.25
Juvenile	29.45	+16.28	N/A	+20.06	+1.99	+1.99
Adult	36.82	+27.28	+7.65	+18.19	-2.91	+6.14

Table 4: Quantification of 5-HT Application on STF Plus a Simulated Blockade.

Simulated Blockade	Baseline *f* (Hz)	Initial Δ*f* With 5-HT (Hz)	Minimal Δ*f* With 5-HT (Hz)	Final Δ*f* With 5-HT (Hz)	Initial Δ*f* After 5-HT (Hz)	Max Δ*f* After 5-HT (Hz)
None	36.82	+27.28	+7.65	+18.19	-2.91	+6.14
InsP3R	36.78	+29.53	N/A	+47.40	+7.73	+7.73
5-HT_2R	36.81	+30.30	N/A	+33.36	+1.35	+1.35
5-HT_{1A}R	36.82	-1.10	-9.67	-4.52	-3.60	+6.12
PKC	36.82	+27.28	+6.81	+6.85	-8.57	+0.12

F3. 5-HT Application and LTF

Unlike Ca^{2+} dynamics and STF, LTF's effects in the models are significantly delayed before clearly detectable. Because the LTF response is slow and temporally nuanced, not all manipulations may necessarily take effect immediately. Much as in STF and cytosolic Ca^{2+} dynamics, LTF in the HM models exhibits developmental differences. Here, developmental differences in the three models may imply the existence of a respiratory critical period. This section will directly address developmental differences between the three HM models, in addition to investigating 1) initiation of LTF, and 2) maintenance of LTF.

F3.a Developmental Differences

In all developmental models, when a continuous pulse of simulated 5-HT is applied, the firing frequency quickly comes back to steady state and exhibits no facilitation (Figure 35d,e,f). Both neonatal and adult HM models additionally experience a transient drop in firing frequency after stimulation that resolves back to baseline frequency. In contrast, the juvenile HM model exhibits no drop in excitability post-stimulation, and recovers almost immediately to baseline firing frequency. All models behave similarly in their short-term response to simulated 5-HT application as they did during the STF protocol, although neonatal and adult models see their late rise in the STF protocol steadily decline with continuous simulated application of 5-HT, where simulated 5-HT is simply applied for longer. This effect is also exhibited in the juvenile model, but in a far less pronounced manner.

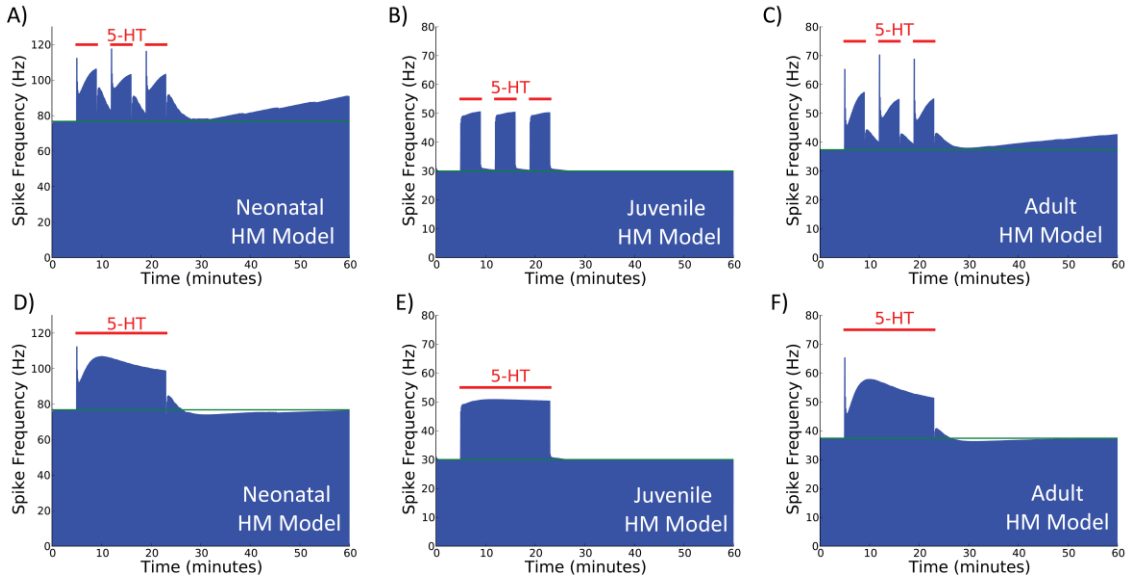

Figure 35: Intermittent vs Continuous Simulated 5-HT Application.
Intermittent and continuous application of simulated 5-HT to all three developmental HM models. Intermittent simulated 5-HT application in the A) neonatal model, B) juvenile model, and C) adult model. Continuous simulated 5-HT application in the D) neonatal model, E) juvenile model, and F) adult model. Spike frequency here refers to the peak firing frequency for each burst.

When three intermittent bouts of 5-HT are applied to either the neonatal or adult HM model, a slow but steady linear increase is firing frequency is observed (Figure 35a,c). However, when the same stimulus is applied to the juvenile HM model, no LTF is observed (Figure 35b). Unlike during continuous simulated 5-HT administration, firing frequency never dips below baseline levels post-stimulation in any of the models. LTF in the neonate is more pronounced than in the adult, although the neonate also subsequently has both a faster baseline frequency and a more pronounced STF response. All models behave similarly to the STF protocol during 5-HT application.

F3.b Initiators of LTF

When the simulated block of PKC is applied throughout the simulated experiment in both the adult and neonatal HM models, we see a complete inhibition of LTF behaviors (Figure 36a,c). Additionally, we also see the loss of 5-HT_2R mediated STF related behavioral changes instigated by the phosphorylation of AMPAR in the model, but not the inhibition of cytosolic Ca^{2+} release through InsP3R, both of which are associated with simulated 5-HT application.

Comparatively, when a simulated MAPK block is performed throughout the simulation in both the neonatal and adult HM model (Figure 38a,c), we see all STF behaviors maintained, but a loss of LTF, and even a slight inhibition overall following the

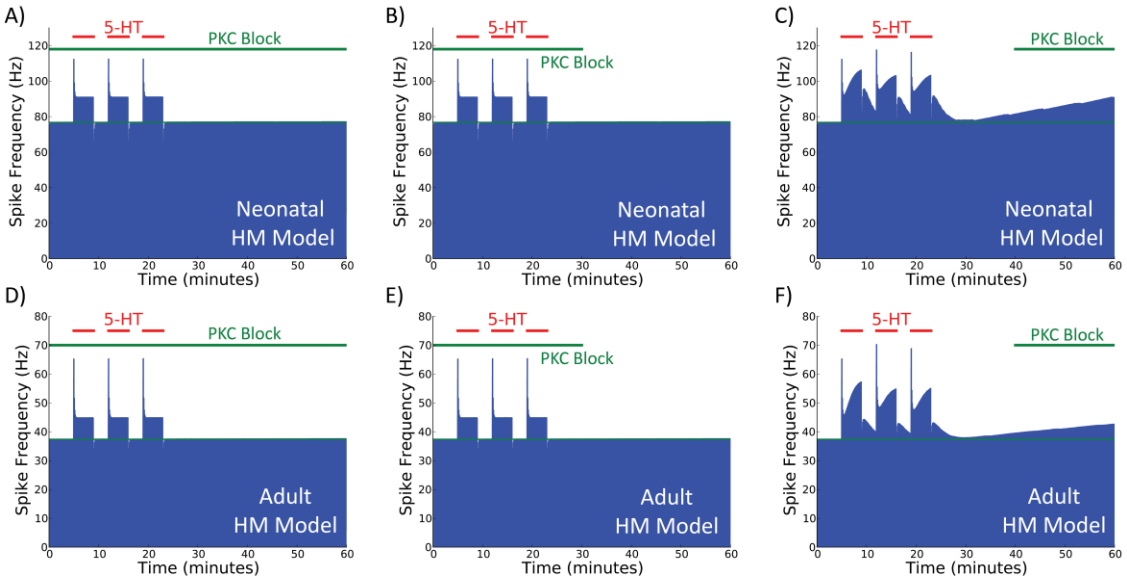

Figure 36: Simulated PKC Block and Its Effect On LTF.
The timing of a simulated PKC block determines whether or not it removes LTF in both the adult and neonatal HM models. When simulated PKC block is applied throughout the simulation in A) the neonatal HM model, and D) the adult HM model, LTF is inhibited. When simulated PKC block is applied during the application of 5-HT in B) the neonatal HM model, and E) the adult HM model, LTF is inhibited. When simulated PKC block is only applied after the initiation of LTF in C) the neonatal model, and E) the adult model, LTF is unaffected. Spike frequency here refers to the peak firing frequency for each burst.

cessation of 5-HT application. Since PKC, the initiator of the MAPK cascade, is critically involved in STF behavior in the model, it is to be expected that sparing PKC would likewise spare all STF effects related to 5-HT_2R related secondary messengers.

Rather than perform simulated PKC or MAPK block on the juvenile HM model, which does not exhibit LTF, we instead simulate a PKC agonist (Figure 37) concurrently with simulated 5-HT, in an attempt to recover LTF behavior. By maintaining simulated 5-HT application, the only distinction between Figure 37a and Figure 37b is the simulated PKC agonist. The application of this simulated agonist recovers LTF, in addition to recovering PKC mediated STF effects.

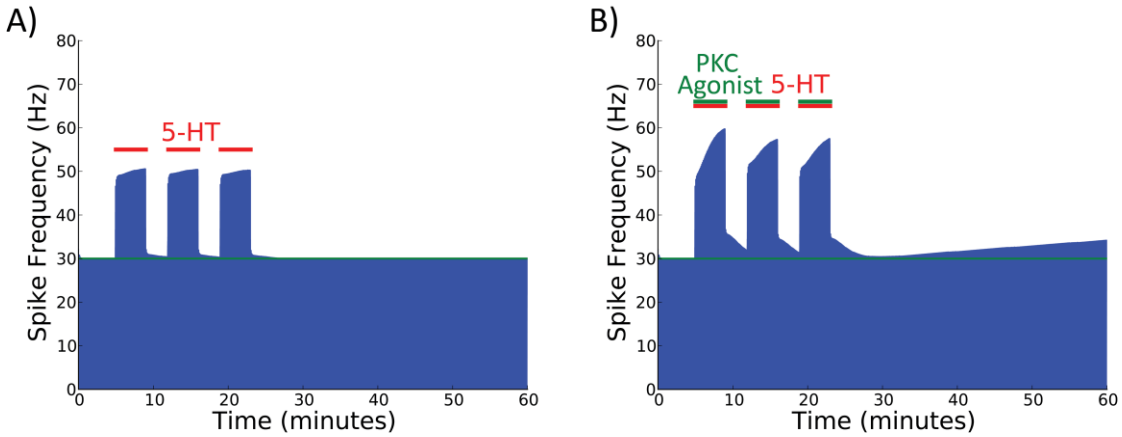

Figure 37: Recovering LTF in the Juvenile HM Model.
A simulated PKC agonist can recover LTF in the juvenile HM model. When comparing A) the juvenile HM model receiving intermittent simulated 5-HT with B) the juvenile HM model receiving intermittent simulated 5-HT and a simulated PKC agonist, LTF is exhibited in A but not B. Spike frequency here refers to the peak firing frequency for each burst.

F3.c Maintainers of LTF

Though initiation of LTF is implicated to be caused by PKC, completely different mechanisms may be associated with its maintenance. Rather than applying simulated blockade throughout the experiment, instead here we apply them well after the point of initiation.

When a simulated PKC block is applied well after initiation we see no effect on LTF in both the adult and neonatal HM models (Figure 36b,d). Instead we see what appears to be no effect whatsoever on behavior. The results are comparable to when no blockers are applied at all. Instead, when a MAPK block is applied after initiation in both the adult and neonatal HM model, we see the steady rise of firing frequency from LTF immediately mitigated and reduced to a steady decline back toward baseline firing frequency in both models (Figure 38b,d).

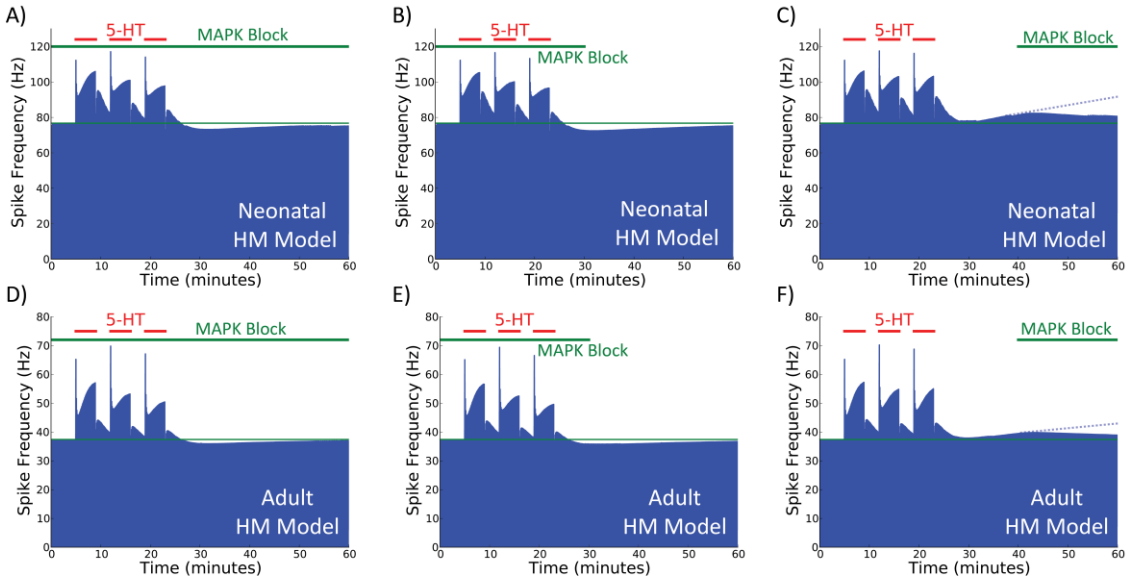

Figure 38: Simulated MAPK Block and Its Effect On LTF.
The timing of a simulated MAPK block either inhibits or disrupts LTF in both the adult and neonatal HM models. When simulated MAPK block is applied throughout the simulation in A) the neonatal HM model, and D) the adult HM model, LTF is inhibited. When simulated MAPK block is applied during the application of 5-HT in B) the neonatal HM model, and E) the adult HM model, LTF is inhibited. When simulated PKC block is only applied after the initiation of LTF in C) the neonatal model, and E) the adult model, LTF is disrupted, and potentiation immediately dissipates back to baseline. Spike frequency here refers to the peak firing frequency for each burst. A dotted line is added where LTF is disrupted, to clearly demarcate where firing frequency would have been –if LTF had been maintained.

F3.d Summary of Results

Developmental distinctions were observed between the juvenile HM model and the other two models. The adult and neonatal HM models exhibited LTF, whereas the juvenile HM model did not, potentially highlighting the existence of a developmental critical period in these models. Juvenile HM LTF could be recovered through the simulated application of a PKC agonist. While the simulated application of PKC block removed LTF when the block was performed throughout the entire simulation in the neonatal and adult HM models, PKC block following LTF initiation has no effect on the continued rise in potentiation. This confirms that the models matches the observation in the literature that PKC is a crucial component for the initiation of LTF. With the simulated application of MAPK block to the adult and neonatal HM model, LTF is removed when the block was performed throughout the simulation, but was still capable of disrupting LTF when applied after initiation. This implicates MAPK as both necessary for initiation and maintenance of LTF. These findings are summarized in Figure 39.

Quantification of the standard response to LTF is given below. As in the STF summary section, Δf is the frequency of each burst in relation to the baseline firing frequency, the steady state burst frequency. Note that even when LTF is not present, extremely small changes in firing frequency can be observed due to AMPAR insertion transients. The trough frequency is the lowest frequency observed between the peak of the post simulated 5-HT STF response, and the end of the simulation. Simulated PKC

block did not produce any trough, and so no trough data were calculated in these cases. All blockade quantifications are for blockade application throughout the course of the simulation.

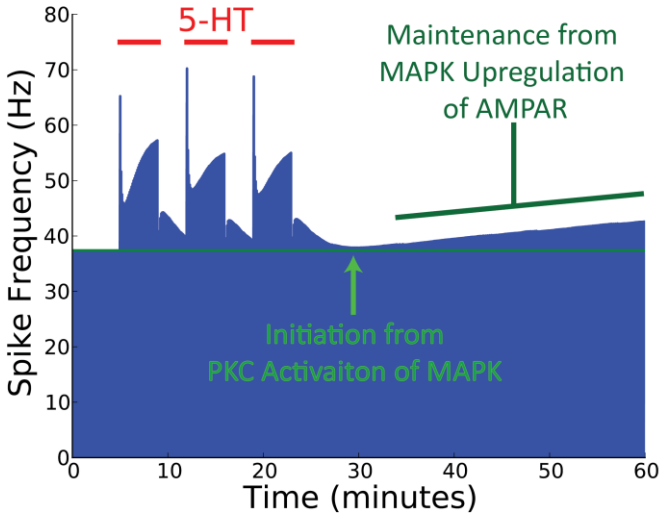

Figure 39: Summary of Causes For STF Related Effects.
LTF initiation is the result of PKC activation of MAPK cascades. LTF maintenance is the result of MAPK cascades upregulating AMPAR. Spike frequency here refers to the peak firing frequency for each burst.

Table 5: Quantification of LTF Under Intermittent vs Continuous 5-HT Application vs Developmental Age.

Developmental Age	5-HT Protocol	Baseline *f* (Hz)	Final Δ*f* vs Baseline (Hz)	Baseline vs Final % Change	Trough Δ*f* vs Baseline (Hz)	Baseline vs Trough % Change
Neonatal	Intermittent	76.69	13.81	18.01%	1.38	1.80%
Juvenile	Intermittent	29.96	0.01	0.03%	-0.19	0.63%
Adult	Intermittent	37.37	5.22	13.97%	0.52	1.40%
Neonatal	Continuous	76.69	-0.58	-0.76%	-2.72	-3.55%
Juvenile	Continuous	29.96	-0.06	-0.21%	-0.29	-0.98%
Adult	Continuous	37.37	-0.21	-0.56%	-1.15	-3.08%

Table 6: Quantification of LTF Under Various Simulated Blockades.

Developmental Age	Simulated Blockade (Agonist)	Baseline *f* (Hz)	Final Δ*f* vs Baseline (Hz)	Baseline vs Final % Change	Trough Δ*f* vs Baseline (Hz)	Baseline vs Trough % Change
Neonatal	PKC	76.69	0.35	0.46%	N/A	N/A
Adult	PKC	37.37	0.18	0.49%	N/A	N/A
Juvenile	(PKC)	29.96	4.16	13.89%	0.38	1.27%
Neonatal	MAPK	76.69	-1.56	-2.03%	-3.43	-4.47%
Adult	MAPK	37.37	-0.51	-1.36%	-1.44	-3.84%

G. Theory

One of the few weaknesses in the above HM models is that they represent a single-cell model of LTF, where most data on HM-based LTF is on the nXII. While normally it would be trivial to generate a network of HMs from the above models, the sheer number of ODEs used to model these systems make a network model prohibitive. In addition, it can be difficult to understand how all the mechanisms combine to form LTF with the level of complexity seen in the full HM models. To address both of these issues, we present a series of reduced models of various phenomena demonstrated above. The ultimate goal is to isolate the necessary mechanisms for LTF, and present them as a minimal model that can be inserted arbitrarily into other non-HM motoneurons.

To this end we present a minimal motoneuron model containing the necessary components to display both cytosolic Ca^{2+} behaviors as well as LTF. From here we derive a reduction of the complex cytosolic Ca^{2+} and buffering system in the full HM models, and demonstrate that it reasonably replicates data in the full model, which itself closely models cytosolic Ca^{2+} data in mouse HM (Ladewig et al 2004). Then, we derive a minimal model of LTF from first-principles, where LTF is attested to throughout the respiratory literature, and then insert this into the minimal motoneuron model to replicate the simulated LTF demonstrated in the full model. While we could also generate minimal models of STF, since it is more difficult to find a suitable analog to STF in the literature, we opt against focusing specifically on closely matching STF responses in our full HM models. Despite this, many of the properties of STF in the full HM models are exhibited as a natural consequence of modeling cytosolic Ca^{2+} and LTF related behaviors.

G1. Minimal Motoneuron Model

While the study of developmental changes in HMs requires looking at a slurry of different ion channels, to produce a motoneuron capable of mimicking both cytosolic Ca^{2+} and LTF data only requires a spiking neuron that's able to bring Ca^{2+} into the cell, and modulate its firing frequency based on that Ca^{2+}. Subsequently, this only requires five ion channels: fast Na^{2+}, delayed rectifier K^+, leak, voltage-activated Ca^{2+}, and Ca^{2+}-gated K^+:

$$C\frac{dV}{dt} = I_{input}(t) - \bar{g}_{leak}(V - E_{leak}) - \bar{g}_{Na}m_{\infty}(V)(V - E_{Na}) - \bar{g}_{K}n(V - E_{K}) - \bar{g}_{SK}z(V - E_{K}) - \bar{g}_{Ca}p(V - E_{Ca})$$

Each of the above gating variables changes over time based on the following equations and parameters, where $x = \{m, n, p\}$.

$$\frac{dx}{dt} = \frac{x_\infty(V) - x}{\tau_x(V)} \qquad x_\infty(V) = \frac{1}{1 + e^{(\alpha_x - V)/\beta_x}}$$

$$z_\infty([Ca^{2+}]_m) = \frac{1}{1 + \left(\frac{0.003}{[Ca^{2+}]_m}\right)^4} \qquad \tau_p(V) = \frac{\gamma_p}{1 + e^{-(\delta_p - V)/\varepsilon_p}} + \sigma_p$$

$$\tau_n(V) = \mu_n$$

$$\tau_z(V) = \mu_z$$

Where I_{input} mimics glutamate in the full model:

$$I_{input}(t) = \begin{cases} 100 & if\ ((t \bmod 6s > 0.5s)\ \&\ (t \bmod 6s < 1.5s)) \\ 0 & else \end{cases}$$

With the following parameters:

$$\bar{g}_{leak} = 0.38\mu S, \quad \bar{g}_{Na} = 1.12\mu S, \quad \bar{g}_K = 1.4\mu S, \quad \bar{g}_{SK} = 0.5\mu S, \quad \bar{g}_{Ca} = 0.08\mu S, \quad C = 0.04\,nF$$

$$\alpha_m = x, \quad \alpha_m = x, \quad \alpha_m = x, \quad \beta_m = x,$$

$$E_{leak} = -80\,mV, \quad E_{Na} = 60\,mV, \quad E_K = -80\,mV, \quad E_{Ca} = 80\,mV, \quad E_h = -38.8\,mV$$

G2. Reduction of Intracellular Calcium Dynamics

Considering the powerful effect 5-HT has on cytosolic Ca^{2+}, and the computational intensity of modeling Ca^{2+} via the diffusion equation, one might ask if some of the more important effects of 5-HT on Ca^{2+} can be modeled with a relative paucity of ODE's.

G2.a Single Compartment Dynamics

We begin this analysis by asking whether a single compartment of Ca^{2+} is capable of exhibiting either bistability or closeness to a bifurcation necessary to push Ca^{2+} from baseline levels to the elevated levels seen under 5-HT application. We begin by assuming a highly simplified model for influx and removal of Ca^{2+} from a simple Ca^{2+} compartment with buffering. Ca^{2+} coming in from voltage-gated Ca^{2+} channels is assumed to be constant, and Ca^{2+} pumped out from the membrane is assumed to be extruded exponentially. From here the main interaction is between the Ca^{2+} compartment and its buffered stores:

$$\frac{d[Ca^{2+}]}{dt} = (a - b[Ca^{2+}]) - IW\,(K_u[Ca^{2+}] * (1 - O_C) - K_r z\, O_C)$$

$$\frac{dO_C}{dt} = K_u[Ca^{2+}] * (1 - O_C) - K_r z\, O_C$$

Where *z* represents a constant that changes under 5-HT application, and the remainder of the constants are defined as follows:

$$IW = 0.32, \quad K_u = 100, \quad K_r = 0.348, \quad a = 0.1, \quad b = 0.1$$

$$z = \begin{cases} 0 & \text{without 5-HT} \\ 2 & \text{with 5-HT} \end{cases}$$

Though the phase plane for this system has tightly overlapping nullclines, it's trivial to show that only a single stable point for $[Ca^{2+}]$ exists at *a/b*:

$$0 = (a - b[Ca^{2+}]) - IW\,(K_u[Ca^{2+}] * (1 - O_C) - K_r z\, O_C)$$

$$0 = IW\,(K_u[Ca^{2+}] * (1 - O_C) - K_r z\, O_C)$$

$$IW(0) = IW\,(K_u[Ca^{2+}] * (1 - O_C) - K_r z\, O_C)$$

$$0 + 0 = (a - b[Ca^{2+}]) - IW\,(K_u[Ca^{2+}] * (1 - O_C) - K_r z\, O_C) + IW\,(K_u[Ca^{2+}] * (1 - O_C) - K_r z\, O_C)$$

$$0 = a - b[Ca^{2+}]$$

$$[Ca^{2+}] = \frac{a}{b}$$

Interestingly, buffering changes have little effect over $[Ca^{2+}]$ beyond short-term transients. Given that the decay rate *b* is generally fixed, the only way to alter Ca^{2+} in any sort of meaningful long-term way will be modifying *a*, the $[Ca^{2+}]$ coming into the system externally.

G2.b Fast/Slow Buffering

Rather than apply a constant with somewhat dubious biological meaning, instead we add a second buffering compartment that represents a very large, but very slowly leaky container compartment reminiscent of the Ca^{2+} stored spatially in the full model:

$$\frac{d[Ca^{2+}]}{dt} = (a - b[Ca^{2+}]) - IW\,(K_u[Ca^{2+}] * (1 - O_C) - K_r z\, O_C)$$
$$+ IZ\,\tau\,(K_u[Ca^{2+}] * (1 - O_{C2}) - K_r z\, O_{C2})$$

$$\frac{dO_C}{dt} = K_u[Ca^{2+}] * (1 - O_C) - K_r z\, O_C$$

$$\frac{dO_{C2}}{dt} = \tau\,(K_u[Ca^{2+}] * (1 - O_{C2}) - K_r z\, O_{C2})$$

We make this a large store of Ca^{2+} to replicate the spatial stores of Ca^{2+} in the full model (IZ = 200), while giving it a slow time constant ($\tau = 0.001$), making O_{C2} difficult to deplete, and a slowness that lets it approximate a constant when pertaining to its steady-state effect on $[Ca^{2+}]$, without changing the system's behavior otherwise:

$$C_1 = \tau\, K_u IZ\,(1 - O_{C2}) \qquad\qquad C_2 = K_r IZ\, O_{C2}$$

$$\frac{d[Ca^{2+}]}{dt} \approx (a - b\,[Ca^{2+}]) - IW\,(K_u[Ca^{2+}]*(1 - O_C) - K_r z\, O_C) - ([Ca^{2+}]\,C_1 - z\,C_2)$$

$$\frac{dO_C}{dt} = K_u[Ca^{2+}]*(1 - O_C) - K_r z\, O_C$$

$$0 = (a - b\,[Ca^{2+}]) - IW\,(K_u[Ca^{2+}]*(1 - O_C) - K_r z\, O_C) - (C_1 - z\,C_2)$$

$$IW(0) = IW(K_u[Ca^{2+}]*(1 - O_C) - K_r z\, O_C)$$

$$0 - 0 = (a - b\,[Ca^{2+}]) - ([Ca^{2+}]\,C_1 - z\,C_2)$$

$$0 = a - [Ca^{2+}]\,(b + C_1) + z\,C_2$$

$$[Ca^{2+}] \approx \frac{a + z\,C_2}{b + C_1}$$

The added benefit is that this also gives us a mechanism to alter the steady state of [Ca^{2+}] simply by applying 5-HT. If we combine this system with the minimal motoneuron model, we get an output strongly reminiscent of 5-HT's effect on cytosolic Ca^{2+} in the full HM models (Figure 40). To achieve this it should also be noted that we reduce the hundreds of [Ca^{2+}] compartments down to three [Ca^{2+}] copmartments: microdomain, pre-microdomian, and cytosolic. Each of which are serially connected, and contain their own buffering variable. Only the cytosolic compartment has a deep buffering compartment. We choose three compartments primarily because it gives better results than two compartments, which constitutes the minimal number of compartments possible while still maintaining the microdomains to be distinct from the cytosol.

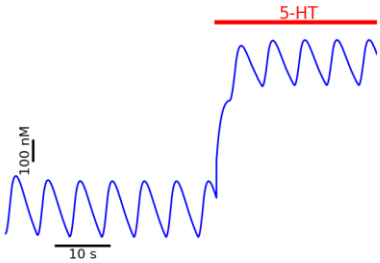

Figure 40: Reduced Cytosolic Ca^{2+}.
When the minimal motoneuron model and the reduced Ca^{2+} are combined under a simulated 5-HT application protocol, we see results strikingly similar on cytosolic Ca^{2+} that we see in the full HM model under 5-HT application. This includes both the rise in baseline Ca^{2+} and the reduction in Ca^{2+}spike height.

G3. Mathematical Foundations of LTF

Fundamentally LTF as a behavior can be represented with a much smaller set of equations than depicted in our realistic HM models. What we're looking for is a system

that responds not to the duration of input pulses, but to the number of pulses received within a short period of time. Furthermore, we want the system to come to a new steady state when sufficiently activated. Since it is relatively straightforward to increase the firing frequency of a variety of neuronal models in the short-term, this section will primarily focus on generating lasting behavioral changes in reduced models of the secondary messenger systems associated with LTF.

G3.a Kinetic Differentiation

To generate a system that responds not to the duration of a pulse, but to the number of pulses received within a short period of time, we effectively want a kinetic model with the following properties:

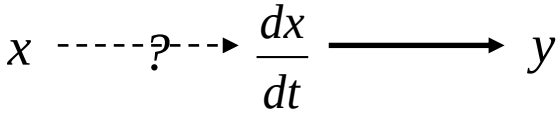

Effectively this corresponds to the following set of differential equations, where *a,b,c,e* in the following text represent rate constants:

$$\frac{dx}{dt} = (other\ inputs / outputs) - ax$$
$$\frac{dy}{dt} = \frac{dx}{dt} - ey + (other\ inputs / outputs)$$

Since *x* and y may play a role in a variety of other reactions not shown, the exact nature of *dx/dt* will change as we change what *x* interacts with, which is undesirable. We need a way to isolate *x*'s current state, to ensure we can simply make *y* vary based on changes in *x* without worrying about what interacts with *x*. The simplest way to do this is to create a new variable that closely approximates *x*. We rename *x* to x_1, and introduce x_2, which we design explicitly to tightly follow x_1:

$$x_2 = x_1$$
$$x_2 \approx x_1 - e^{-t\tau} \quad (\text{for large } \tau \text{ or } t)$$
$$x_1 - x_2 = e^{-t\tau}$$
$$\ln(x_1 - x_2) = -t\tau$$
$$\frac{dx_2}{x_1 - x_2} = \tau\, dt$$
$$\frac{dx_2}{dt} = \tau\,(x_1 - x_2) = \tau\, x_1 - \tau\, x_2$$
$$\frac{dx_2}{dt} = a\, x_1 - b x_2 \qquad (\text{for } a \approx b)$$

To this end, we can now say with certainty that:

$$\frac{dx_1}{dt} \approx \frac{dx_2}{dt}$$

From here, the simplest modification to our equation for *dy/dt* that satisfies our desired criteria is to replace dx_1/dt directly with dx_2/dt, which gives us the following modification to *dy/dt*:

$$\frac{dy}{dt} = c\frac{dx_2}{dt} + (other\ inputs / outputs)$$

We may now write out the full set of differential equations for the system:

$$\frac{dx_1}{dt} = (other\ inputs / outputs) - ax_1$$
$$\frac{dx_2}{dt} = ax_1 - bx_2$$
$$\frac{dy}{dt} = c\,(ax_1 - bx_2) - ey + (other\ inputs / outputs)$$

This can be more intuitively described through the following set of reactions, where dashed lines represent inhibition, and solid lines represent excitation:

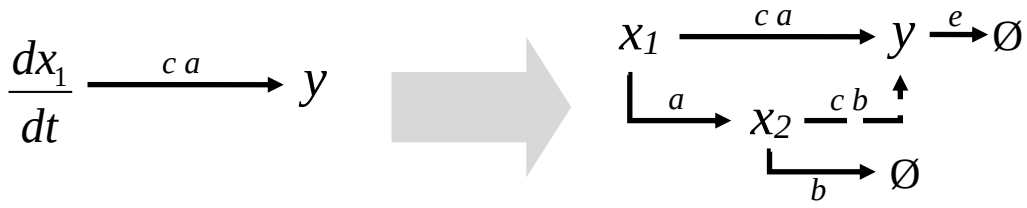

With a simple, clean system for producing differentiation, regardless of x_1's inputs, we can easily drive *y* based on changes to x_1 rather than x_1 directly. Subsequently this neither requires complex mathematics nor an elaborate reaction scheme.

G3.b Accumulation

The main difficulty in using a differentiation operation to sum incoming square wave pulses is that a positive pulse is received when a square wave turns on, but an equally strong negative pulse is received when the square wave turns off. This ought to result in a net zero accumulation of signals. However, realistic biological systems have a property that effectively permits for easy accumulation of differentiated signals: a lack of negative concentrations. So long as negative pulses from the removal of a square wave input are sufficiently truncated by hitting zero, it makes accumulation of signals possible, as the total amount of input from positive pulses will now be greater than negative pulses.

With the truncation of negative signals, all that one needs to accumulate successive pulses is an additional variable that changes sufficiently slowly compared to the incoming signal, allowing for multiple pulses to effectively be summed over time.

An example system demonstrating the truncation and accumulation behaviors are shown below, where the new variable *z* is introduced as the accumulation variable:

$$I(t) = \begin{cases} 100 & if\ \ (t \bmod 10) > 5 \\ 0 & if\ \ (t \bmod 10) \le 5 \end{cases}$$

$$\frac{dx_1}{dt} = I(t) - 5x_1$$
$$\frac{dx_2}{dt} = 5x_1 - 5x_2$$
$$\frac{dy}{dt} = 10x_1 - 10x_2 - 5y + 10$$
$$\frac{dz}{dt} = \frac{3}{4}y - \frac{1}{10}z$$

Integration of the aforementioned system starting from steady state conditions yields both truncation (Figure 41a) and accumulation (Figure 41b) behaviors.

G3.c Bistability

The sort of bistability exhibited in LTF can be modeled with a one-dimensional differential equation without bifurcations. The only requirement is that there exist two stable points, and so this is most simply modeled through a cubic polynomial ordinary differential equation. With the proper parameters, such a function will produce three stable points: an equilibrium point when LTF is off, an equilibrium point when LTF is on, and an unstable point representing the threshold between the two states. These three points will also subsequently be the roots of the cubic function, and so we get the following system:

$$\frac{dz}{dt} = pz^3 + qz^2 + rz + s$$

When we combine the above equation with the accumulator from the previous section, and properly set parameters, we get the following sample reduced LTF system:

$$I(t) = \begin{cases} 100 & if\ \ (t \bmod 10) > 5 \quad \text{and} \quad t < t_{\max} \\ 0 & if\ \ (t \bmod 10) \le 5 \quad \text{or} \quad t \ge t_{\max} \end{cases}$$

$$\frac{dx_1}{dt} = I(t) - 5x_1$$
$$\frac{dx_2}{dt} = 5x_1 - 5x_2$$
$$\frac{dy}{dt} = 10x_1 - 10x_2 - 5y + 10$$
$$\frac{dz}{dt} = 0.5y - 0.0092\left(-0.1728z^3 + 8.064z^2 - 73.92z + 124\right)$$

The phase plane for *dz/dt* vs *z* is shown in Figure 41c, and the equilibria for the system are given below:

Table 7: Equilibria for dz/dt vs z phase plane.

***z* =**	2.16517945965	9.45732657929	35.0441606277
Stability	Stable	Unstable	Stable

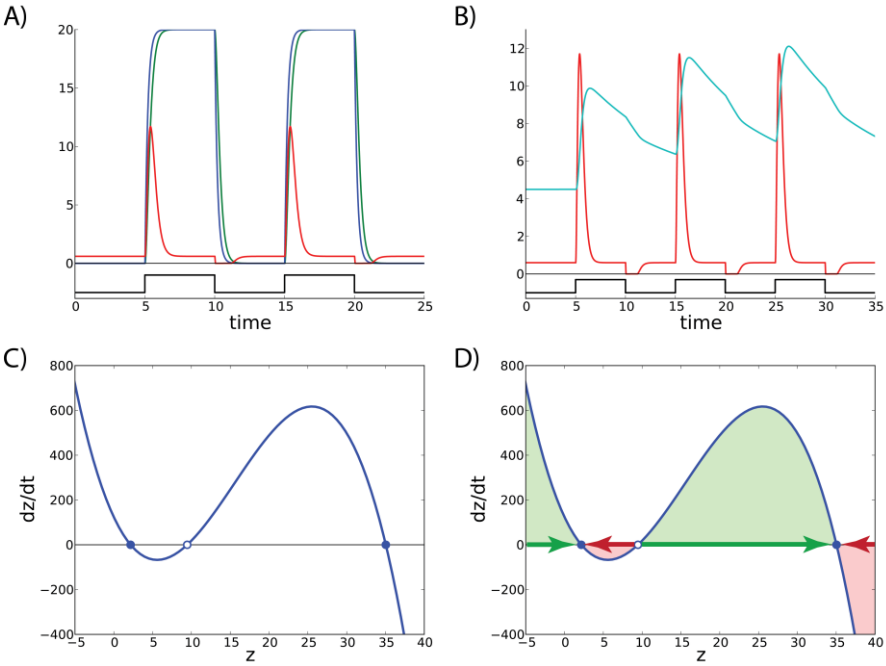

Figure 41: Derivatives, Truncation, Accumulation, and Bistability in the Reduced Model.
Depiction of the various reduced mechanisms from the full model that are vital to the replication of LTF. A) The derivative of the input stimulus, and truncation of negative signals, where x_1 is the blue line, x_2 is the green line, the derivative parameter *y* is the red line, and the input is a square pulse. B) Accumulation of the truncated derivative of the input, where *y* is the red line, and the accumulation parameter *z* is the cyan line. C) Phase plane of the accumulation parameter *z*, exhibiting bistability, and D) domains of attraction for the two stable points.

When two pulses are applied, no LTF is observed (Figure 42a); but when three pulses are applied, LTF is observed (Figure 42b).

G4. Reduced vs Full Model LTF

G4.a Spiking Reduced Model LTF

When the minimal LTF model is combined with the minimal motoneuron model, and the reduced Ca^{2+} model, we get behavior strikingly similar to the adult and neonate full HM model. Specifically, we see frequency-based single-neuron LTF under simulated intermittent hypoxia (Figure 42e), but not simulated continuous hypoxia (Figure 42d). Both a fast excitatory short-term response and a slower potentiation of the long-term response are observed.

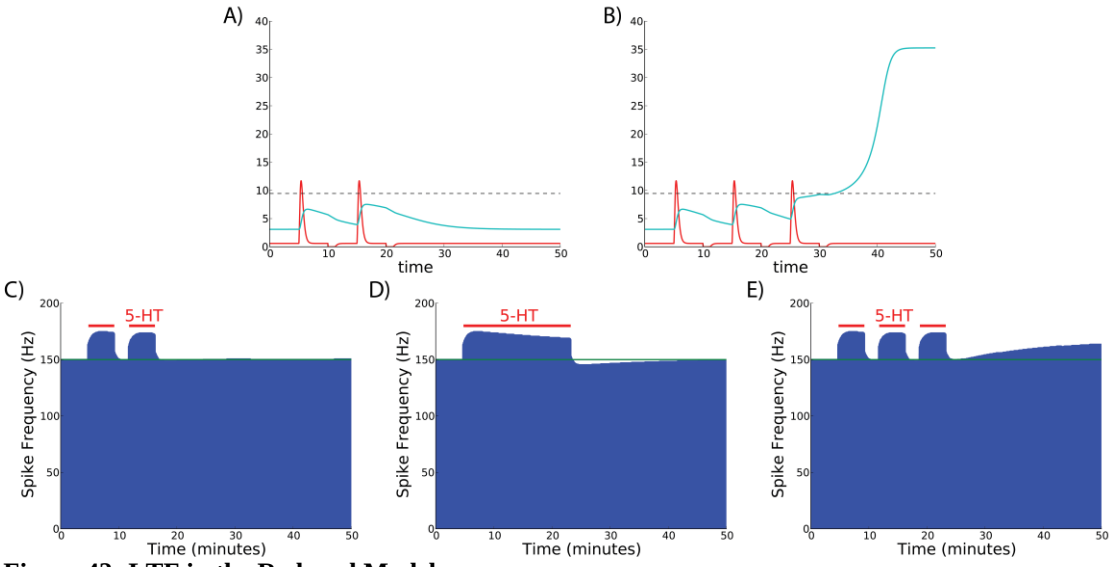

Figure 42: LTF in the Reduced Model.
The reduced LTF model in isolation (A,B), and combined with the spiking reduced model and reduced Ca^{2+} (C,D,E). A) When z (cyan) receives insufficient stimulus, no LTF is achieved. B) When z (cyan) crosses the threshold defined at its unstable equilibrium, LTF is achieved. C) When the combined system receives insufficient stimulus, no firing frequency based LTF is achieved. D) When the combined system receives an improperly patterend input, no firing frequency based LTF is achieved. E) When the combined system receives a sufficient number of pulses from a properly patterend input, LTF is achieved. Spike frequency here refers to the peak firing frequency for each burst.

G4.b Full Model LTF Secondary Messenger Correlates

The secondary messenger cascades in the full models can be readily broken down into their minimal LTF correlates based on topological considerations (Figure 43a), and general behavior (Figure 43c).

Since $G_{\alpha q}$-GTP mostly passes on the 5-HT input signal through PLC, DAG, IP_3, and PKC, the entirety of this circuit can be considered more or less part of the input signal, which corresponds to x_1 in the minimal model. Due to Raf receiving an excitatory

input from PKC, and a near-equivalent signal from Ras, with this generating a rough derivative of PKC as a result, we effectively get the dynamics of x_2 with Ras and y with Raf. This signal finally is sent into the MAPK cascade, which itself is known for potential bistable behavior, and exhibits a sufficiently slow decay as to permit a buildup upon repeated input stimuli, thus properly representing z.

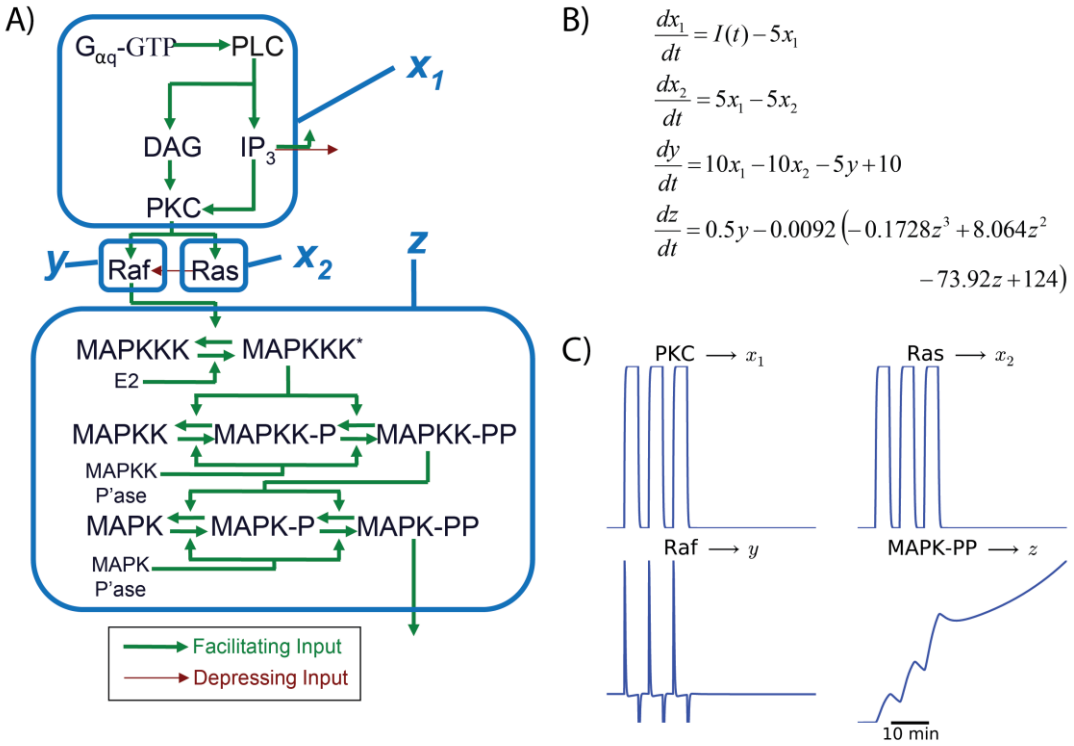

Figure 43: Correspondence Between Full Model Secondary Messenger Systems and Minimal LTF Model.
A comparison of secondary messenger systems in the reduced model, and the full model that inspired it. A) A diagram showing the entire secondary messenger cascade associated with 5-HT2R's G-coupled protein, and the groupings of chemical reactions that correspond to minimal LTF variables. B) The reduced model's defining differential equations. C) Plots of PKC, Ras, Raf, and activated MAPK (MAPK-PP or K-PP) in the neonatal full HM model displaying the variables in the minimal LTF model that they correspond to.

H. Discussion

H1. 5-HT Application and Cytosolic Ca^{2+}

Cytosolic Ca^{2+} exhibits two characteristic changes during the application of 5-HT: a steady rise in baseline cytosolic Ca^{2+}, measured from trough to trough of each Ca^{2+} spike; and a decrease in the height of Ca^{2+} spikes themselves. Both of these effects can be explained in the model via mechanisms of Ca^{2+} intake and release known to be affected by 5-HT application: voltage-gated Ca^{2+} channels, and InsP3 receptors.

The putative cause of a rise in baseline Ca^{2+} during simulated 5-HT application is release of Ca^{2+} from endoplasmic reticulum stores via InsP3R. Under the simulated blockade of InsP3R in the model, we not only see a removal of the rise in baseline Ca^{2+}, but a slight depression in baseline Ca^{2+}. Under InsP3R block, the observed depression in baseline Ca^{2+} in the model can be explained by the decrease in Ca^{2+} spike size from 5-HT_{1A}R. This decrease of incoming Ca^{2+} from microdomains in the model means less Ca^{2+} diffusing into the cell overall. This decrease in Ca^{2+} from the microdomains in the model is otherwise masked by the typical flood of Ca^{2+} from opened simulated intracellular stores. We can be certain that downstream phenomena involving AMPAR play little role in this behavior, as a simulated 5-HT_2R block inhibits both InsP3R and AMPAR-related mechanisms in the model, and the results are comparable to simulated InsP3R block.

The modulation of Ca^{2+} spike height appears to be more multifaceted. While simulated blockade of 5-HT_{1A}R does remove a good deal of the mitigation in Ca^{2+} height, as this retains a steady flow of Ca^{2+} from microdomains to the cytosol, the sharp increase in cytosolic Ca^{2+} from InsP3R can, in turn, inhibit firing frequency as it diffuses from cytosol to microdomains. In effect, the size of the Ca^{2+} spike observed in the model is highly regulated by the current Ca^{2+} state of the simulated cell, and so even with a faster firing frequency, and more Ca^{2+} from HVA Ca^{2+} channels, this increase in Ca^{2+} would inhibit firing frequency via SK channels, and thus the system is self-limiting. Since InsP3R activation isn't strongly mediated by firing frequency, release of intracellular Ca^{2+} stores is not inherently self-limiting, but the stores themselves are implicitly limited in size. Between these two properties, it would be quite difficult for the system to generate a runaway increase in cytosolic Ca^{2+}, which is known to be cytotoxic.

Subsequently, these results mostly support our hypotheses. While we confirm that InsP3R mediated release of Ca^{2+} from intracellular stores is responsible for the rise in baseline Ca^{2+} in the model, and while we also confirm that 5-HT_{1A}R inhibition of HVA Ca^{2+} channels mitigates Ca^{2+} spike height in the model, Ca^{2+} release from InsP3R channels can play a more subtle role in the Ca^{2+} spike height in the model than anticipated, and so it may be more correct to say that 5-HT_2R are responsible primarily for increase in baseline Ca^{2+} in the model and secondarily for modulating Ca^{2+} spike height in the model, whereas 5-HT_{1A}R are primarily responsible for modulating Ca^{2+} spike height alone in the model. These findings are summarized in Figure 44a.

Developmentally, the neonatal and adult HM models are topologically quite similar, but the juvenile HM is thoroughly distinct, curiously resembling simulated InsP3R block and simulated 5-HT_2R block in the adult HM model, although less severe in the drop in Ca^{2+} it receives. This appears to be due to differences in effective Ca^{2+} storage that result in less Ca^{2+} availability during InsP3R mediated release of Ca^{2+}. While the blocking of the opening of these channels is certain to generate a dip rather than a rise in baseline Ca^{2+} in both the neonatal and adult HM model, this action is fundamentally different than in the unmodified juvenile HM model, which simply lacks the buffered Ca^{2+} to generate a baseline rise. This distinction itself seems to be an emergent property of these systems, as the parameters and equations governing cytosolic Ca^{2+} buffering directly are identical in all three developmental HM models.

H2. 5-HT Application and STF

Under the short-term application of 5-HT, we see a number of responses related to voltage-gated Ca^{2+} channels, cytosolic Ca^{2+}, and AMPAR phosphorylation in the model. Fundamentally there are two clear behaviors exhibited in biological systems also exhibited in the model, and a third less clear behavior that may appear in biological systems: 1) With the application of hypoxia or 5-HT in biological systems, an immediate potentiation, or STF, is clearly observed. 2) After the removal of the 5-HT or hypoxic stimulus on the biological preparation, the potentiation lingers transiently in a muted form, which here is called post-STF potentiation. 3) After STF but before the post-STF potentiation, there is a slight inhibition sometimes exhibited in biological systems, and exhibited in the juvenile and adult HM model.

The simulated block of 5-HT_{1A}R completely removes the STF response in its entirety, leaving a slight inhibition of firing frequency in its place. In comparison, no other simulated block performed can completely eliminate the STF response in the models. This strongly implicates the inhibition of HVA Ca^{2+} channels by 5-HT_{1A}R in the STF response, which in turn inhibits SK channels, and results in a strong potentiation of the HM. While no other simulated block can remove STF entirely, simulated InsP3R block and simulated 5-HT_2R block can increase the magnitude of the STF response. This increase in magnitude appears to be part of a loss of an inhibitory component associated with InsP3R mediated Ca^{2+} release from intracellular stores.

In the early portion of simulated 5-HT application, we see an initial abrupt rise in firing frequency from 5-HT_{1A}R, which is then quickly inhibited exponentially in the neonatal and adult HM model, but not in the juvenile HM model. Given that simulated InsP3R block stops the exponential decay, it is concluded that this is a product of InsP3R mediated Ca^{2+} release in the model. After 5-HT is removed, the observed response is closely related to this exponential decay, but in reverse. Rather than an exponential decay from the peak firing frequency, we see an exponential decay to the steady state firing frequency from a depressed frequency, which itself is masked by the post-STF potentiation. With simulated PKC block, we can reveal the exponential decay, and with InsP3R block we can remove it. Both of these heavily implicate cytosolic Ca^{2+} as the formative player in these two related responses. Since high cytosolic Ca^{2+} would be expected to generate an inhibitory effect, it is quite reasonable that 5-HT application, as in the previous section, would generate high levels of cytosolic Ca^{2+}, and in turn reduce firing frequency. Likewise, simulated PKC block would reveal this decay primarily because the only other effect playing a major role is the phosphorylation of AMPAR, which can be seen increasing AMPAR conductance steadily with the application of 5-HT, and then lingering after 5-HT is removed. As is to be expected, the decay is missing in the juvenile HM model, and all models with InsP3R block. This subsequently explains the more square-wave like shape of juvenile STF in the model, given its lack of a cyotoslic Ca^{2+} mediated drop during STF. Subsequently, as simulated InsP3R mediated Ca^{2+} release also controls post-STF inhibition in the model, this also explains why no dip below baseline firing frequency is observed in the Juvenile HM model after the removal of simulated 5-HT. Developmentally, the neonatal model exhibits a greater depression of firing frequency after simulated 5-HT removal than the adult model, which corresponds to its greater cytosolic Ca^{2+} dynamics in general, where the juvenile model exhibits

greater rises in Ca^{2+} with simulated 5-HT, and with each HM burst. The net result are more pronounced effects coupled to cytosolic Ca^{2+} changes.

Even after the removal of simulated 5-HT, a transient potentiation of the juvenile and adult HM models lasts for several minutes. This post-STF potentiation is additionally accompanied by a steadily increasing potentiation during 5-HT application itself. Both the steady rise of excitability during simulated 5-HT application, and the steady fall of excitability following the removal of simulated 5-HT application are removed under simulated blockade of PKC and 5-HT_2R, but not under simulated MAPK block. The implication is that both of these mechanisms are the result of AMPAR phosphorylation by PKC, and that these two mechanisms are likely part of a singular phenomenon, where AMPAR phosphorylation increases insertion rates into the membrane during simulated 5-HT application, and the removal of that 5-HT stimulus results in a slow process of removing the excess of inserted AMPAR. The post-STF potentiation part of this process, however, is more clearly visible in biological LTF experiments, as it is not masked by other STF related behaviors.

In terms of eliciting an STF response at all, the primary factor in all of the models appears to be the inhibition of voltage-gated Ca^{2+} channels via 5-HT_{1A}Rs, which generates the bulk of the response. In comparison, the brief, transient post-STF potentiation appears to be driven by AMPAR phosphorylation in the model. This subsequently supports both of our STF related hypotheses, and lends credence to the possibility that 5-HT receptors of different types play distinct stereotyped roles in the response to hypoxia. Even though 5-HT_2R may play a role in post-STF potentiation, the majority of the response is still driven by 5-HT_{1A}R in our models, and so 5-HT_{1A}Rs may primarily be seen as supporting rapid, short-term responses to 5-HT, while 5-HT_2Rs are primarily involved mediating longer-term responses to intermittent challenges. Subsequently, these are all testable predictions that can be verified or refuted with biological experimentation. The relation of STF behaviors observed in the model, and its relation to biological STF phenomena, is given in Figure 44b.

H3. 5-HT Application and LTF

Whether or not LTF is achieved in the model is a factor of developmental properties, simulated pharmacological manipulations, and the duration and timing of simulated 5-HT application. All of these factors interplay with the upregulation and insertion of AMPAR, which effectively serves as the HM model's electrophysiological correlate to LTF.

In all models exhibiting LTF, successfully achieving LTF required the application of a series of intermittent bouts of 5-HT whose frequency is sufficiently fast to ensure an accumulation of secondary messenger cascades that ultimately push the simulated MAPK cascade from its low equilibrium point to its high equilibrium point, which in turn enhances the production of AMPAR. When a single, continuous pulse of simulated 5-HT is applied to any of the HM models, LTF is not achieved, as the system is potentiated primarily by increases in 5-HT concentration, rather than the total concentration of 5-HT. A single pulse of 5-HT is insufficient to push the MAPK cascade from its low equilibrium point to its high equilibrium point. Although it is conceivable that a potent enough single pulse could produce this effect in some motoneurons, this is not observed

in either real HMs or our models. Increasing the connection strength between PKC and the start of the MAPK cascade, however, could produce this effect.

Developmentally we observe that the neonatal and adult HM model exhibit LTF, but the juvenile model does not. This is likely due to the juvenile model's reduced density of 5-HT_2R, as 5-HT_2R block in the adult model resembles the juvenile HM model in terms of cytosolic Ca^{2+}, STF, and LTF. While it still should be entirely feasible to generate LTF in the juvenile model, as the density of 5-HT_2R is non-zero, it would require a far more intense series of 5-HT bouts, or a greater number of bouts, compared to the neonatal or adult model. Since the juvenile model corresponds to the critical period in the HM in rodents proposed by Wong-Riley, we can predict that rodents around P12 may lack robustness in a situation with an intermittent hypoxic challenge. Given that a lack of robustness in the face of hypoxic challenges may be associated with SIDS in humans and other animals, it is also reasonable to conjecture that a critical period during development where LTF is weakened or disrupted may potentially contribute to SIDS. Subsequently, this also supports our hypothesis that the juvenile age range, in contrast to the neonatal and adult age ranges, may contain a unique set of electrophysiological and pharmacological characteristics that are inherently disruptive to LTF. While we conclude that 5-HT_{1A}R are not a necessary facet to LTF in the model, the drop in 5-HT_2R in the juvenile model is absolutely crippling to LTF generation in the model, as this naturally blunts PKC activation. While findings in the model must remain conjecture until analogous biological experiments have been performed, they may lend insight into a minimal set of biological pharmacological manipulations that might lead to similar results.

In addition to SIDS, we also note that the neonatal model, in comparison to the adult model, has a far higher firing frequency. This may be because the larger nXII in the adult requires less drive per HM to maintain sufficient output. It may also be because neonates in general require stronger glottal drive as part of suckling behaviors. Alternately, it may simply be an arbitrary property of the model. Regardless of the reason, if the reduced drive in the single adult HM model is paralleled in adult biological nXII, then this may be a contributing factor to the existence of OSA in adults.

Through the use of various simulated blockades, LTF can be eliminated in HM models exhibiting it, and restored in HM models not displaying it. In instances where it arises naturally, such as in the adult and neonatal HM model, it can be eliminated either by simulated PKC or MAPK blockade. This is due to the fact that PKC feeds directly into the MAPK cascade. By blocking either, LTF becomes impossible. Likewise, when we take models where LTF does not exist, such as the juvenile HM model, applying a simulated PKC agonist alongside of simulated 5-HT, or in the place of 5-HT, will readily restore LTF. While blocking PKC or MAPK at all points in time during an experiment can negate LTF, this does not address initiation versus maintenance. Since simulated PKC block following initiation has no effect on LTF, but blocking MAPK after initiation quickly disrupts LTF, we can clearly say that MAPK is the primary maintainer of LTF in our models, whereas PKC is involved more in the initiation of LTF through stimulation of the MAPK cascade, as originally hypothesized. These findings are summarized in relation to biological LTF in Figure 44c.

In addition to LTF, we also observe a variety of long-term post 5-HT responses in the form of a dip in excitability prior to LTF becoming apparent. Curiously this effect is

not seen at all in the juvenile HM model under any circumstance. Yet, both the juvenile and adult HM models exhibit it quite visibly in MAPK blockade experiments, and under continuous simulated 5-HT application. If we consider that simulated PKC blockade eliminates the behavior, but MAPK does not, it becomes clear that the effect is related to AMPAR insertion, or in this case AMPAR removal, which appears to overcompensate for the removal of the simulated 5-HT stimulus when LTF isn't initiated. Phenomenally, this effect is also seen in the minimal motoneuron model + minimal LTF model, highlighting that this may potentially be a fundamental aspect of the AMPAR insertion system.

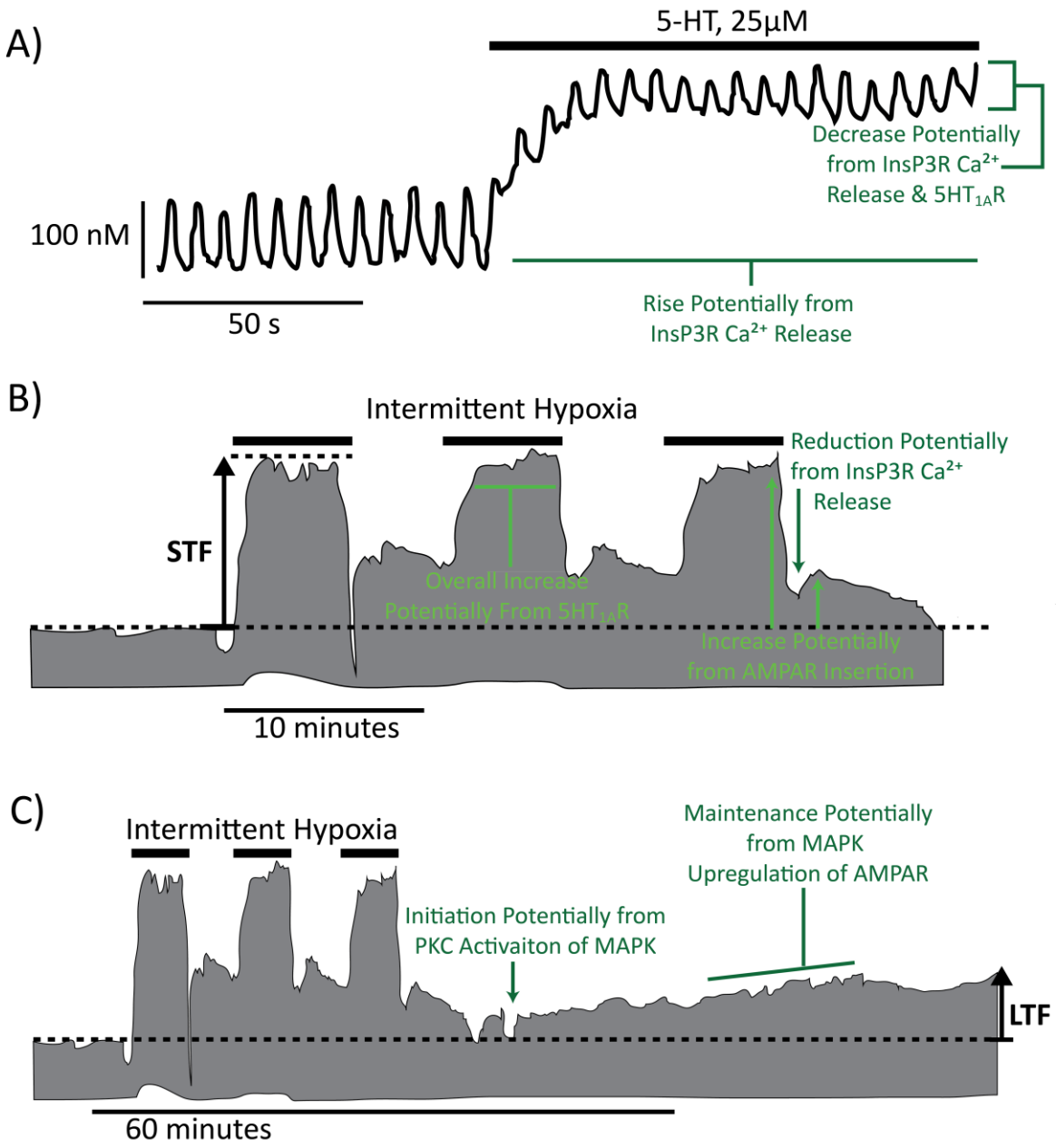

Figure 44: Summary of Model Effects Relevant to Biologically Observed Behaviors.
A visual depiction of effects observed from the HM models that have relevance in potentially explaining behaviors observed in biological experiments. A) Cytosolic Ca^{2+} related behaviors based on the HM models, with biological data traces adapted from Ladewig et al (2004). B) STF related behaviors based on HM models, with biological data traces adapted from Baker-Herman and Strey (2011). C) LTF related behaviors based on HM models, with data traces adapted from Baker-Herman and Strey (2011),

H4. Theory

In approaching a mathematical reduction of LTF and intracellular Ca^{2+} behaviors, we find in both cases that many of these behaviors can be replicated with far fewer differential equations. Depending on the specific intended experimental manipulations, much of the complexity of the MAPK and PKC pathways may not be strictly necessary to maintain their properties, as a full Ca^{2+} diffusion model isn't required to model certain 5-HT mediated behaviors. Such systems not only make analysis easier, they also highlight how similar behaviors could arise in biologically distinct but mathematically similar systems.

The capacity to perform derivatives with kinetic models highlights the ease in which relatively complex mathematical operations can be performed with surprisingly simple coupled chemical reactions. Combined with properties like multiple stable points, a plethora of elaborate systems can be crafted even before resorting to bifurcations. While this may be surprising to some that bifurcations are not at all necessary to get LTF or LTF-like effects, we must all bear in mind that even without bifurcations, dynamical systems can be quite complex in behavior. It should also be noted that a lack of mathematical necessity does not rule out the possibility that bifurcations in this system may exist in biological preparations, either for LTF related behaviors or for other unrelated processes.

Although the accumulation of repeated input signals may itself be a somewhat trivial process, segments of a biological system responsible for accumulation will subsequently also have the most relevance when considering which parts of the system tune for thresholding of hysteretic effects. In this sense, although accumulation parameters may be the least interesting mathematically, they end up being some of the most important biological components. Rapidly rising accumulation parameters allow for quick integration of signals, while slowly rising accumulation parameters require signals to be on for longer before accumulation truly commences. Slowly decaying accumulation parameters permit for the accumulation process itself to occur over longer periods of time without penalty, while more dramatic decays impose sharper time limitations on when input signals must arrive for accumulation.

That there exist analogous mathematical properties in both the full and reduced model in terms of secondary messenger systems permits a better mechanistic understanding of how each part of the full secondary messenger pathway exhibits its effects. This itself can help to pinpoint the most effective parts of the system to apply pharmacological manipulations, and so exhibits utility even for experimentalists. Furthermore, by using a reduced model as a map to the full model, one can go back and determine if there are any necessary behaviors within the full model that haven't yet been encapsulated in the reduced. In this way, by iteratively moving between full and reduced model, one can come to a more complete understanding of a system at a fundamental, mathematical level.

H5. Limitations

As in all protocols, the computational approach has its own strengths and limitations that must be kept in mind when comparing these results to biological experiments and other computational models.

All of the work done above has been in an isolated, single HM model. While much of the literature on HM LTF is in neonatal slice preparations, or XII nerve cuffs in the intact adult rat, and much of the literature on LTF in general is in overall LTF of respiratory output, some studies have been done in insolated HMs where it is typically called ivLTF (Feldman et al 2005). While many of these results may take on their own characteristic form, the overall condition of increasing output remains consistent in all preparations. For this reason we consider these varied forms of LTF comparable, especially since many of the more isolated forms of LTF are most likely parts of the overall LTF behaviors exhibited in the whole animal.

In the literature, LTF can take the form of either an increase in burst amplitude or burst frequency. While our HM models exhibit bursts, these bursts are driven by an external simulated glutamatergic drive that itself cannot be facilitated in our model. Since LTF in our model involves an increase in postsynaptic AMPAR density, it stands to reason that increasing the glutamatergic drive rather than the AMPAR density would have a similar effect: an amplitude-based LTF. In comparison, an increase in drive frequency would generate an output more analogous to frequency-based LTF. Subsequently, because upstream mechanisms can also potentially exhibit LTF, the LTF recorded in the XII nerve may itself be a compound LTF, combining increases in frequency and amplitude in glutamatergic drive with increases in postsynaptic AMPAR, which accentuate these drive changes. However, because our models exhibit LTF at the single cellular level, caution must be taken when comparing it directly to other forms of LTF.

Throughout this project, we have focused on modeling LTF, its initiation, and maintenance. However, because these studies of LTF overwhelmingly focus on LTF initiation and maintenance, and not cessation, we have very few clues to piece together putative mechanisms controlling the loss of LTF after a long period of time with no subsequent hypoxic insults. Furthermore, even if we had an understanding of the mechanisms driving cessation, the amount of computational resources required to run such simulations would be extremely prohibitive, as we are now potentially describing an order of magnitude increase in simulation time. Despite this, we can theorize possible mechanisms for LTF cessation based on what we know of the full and reduced model. An inhibitory feedback loop that progressively applies an inhibitory signal to the MAPK cascade could eventually push the system back down to its lower stable point, thus eliminating LTF. An alternate approach would be to have a bifurcation in the MAPK cascade that eliminates the high stable point, thus forcing the system to converge back to the only remaining stable point: the one associated with the non-LTF state. Both of these mechanisms could certainly be produced, but in the absence of additional biological data, we are reticent to make strong statements either way.

Although reduced models offer a powerful set of tools for investigating biological systems, caution must be exhibited when dealing in such models, as reductions often omit properties that may not be of interest in a particular experimental manipulation, but may

prove crucial for another manipulation that was not under consideration during the reduction. While replacing the diffusion PDE for Ca^{2+} with a single "slow buffering" compartment is sufficient for changes to baseline Ca^{2+} via InsP3Rs, there is no guarantee that it will model other behaviors not explicitly investigated, such as the drop in firing frequency during STF in the neonate and adult HM full models. Likewise, the MAPK cascade model used in the full HM models has been reported to exhibit oscillatory behavior (Qiao et al 2007). Subsequently, this may explain oscillatory behavior seen in systems not exhibiting LTF, but still exhibiting responses to 5-HT application (Feldman et al 2005). Indeed, while it would not be terribly difficult to modify our reduced models to include the aforementioned behavior, since such results are beyond the scope of this study, we opt to not pursue such additions further here.

H6. Summary of Predictions

Overall this project has produced a multitude of predictions that can now be tested by experimentalists to confirm their validity. A concise list of these predictions are as follows:

- **Rise** in baseline **Ca^{2+}** during 5-HT application is due to **InsP3R** Ca^{2+} release.
- **STF** is primarily due to **$5HT_{1A}R$** related mechanisms.
- **LTF** is primarily due to **$5HT_2R$** related mechanisms.
- **Post-STF potentiation** is primarily due to **$5HT_2R$** related mechanisms.
- **Initiation** of LTF is mediated by **PKC** stimulation of MAPK cascades.
- **Maintenance** of LTF is mediated by **MAPK** cascades that upregulate AMPAR.
- **Bistability** in the MAPK cascade is critical to **LTF** initiation and maintenance.

Subsequently, these predictions can be tested using the blockers and agonists detailed in the results section, in a similar fashion to the aforementioned simulated experiments.

H7. Testing Predictions

With a number of testable predictions resulting from this work, suggested pharmacological agents for replicating the simulated pharmacological manipulations may be helpful to experimentalists seeking to test any of the predictions described here. Pharmacological agents analogous to the manipulations described in the Methods section are given below.

Simulated InsP3R blocade is similar to the effects of the antagonist 2-aminoethoxydiphenyl borate (2-APB), which subsequently also has an effect on TRP channels, which are not considered to play a role in HM ivLTF.

Simulated $5\text{-}HT_2R$ blockade is roughly equivalent to the effect of applying Ketanserin, a known antagonist with a high affinity for $5\text{-}HT_{2A}$ and $5\text{-}HT_{2C}$ receptors. Although Ketanserin is also known to block $5\text{-}HT_6$, α_1 adrenergic receptors, and H1 histamine receptors, $5\text{-}HT_6$ are not produced in significant quantities in HMs (Zhan et al 2002), and H1 does not play a major role in HM ivLTF. α_1 receptors act on the same G-

coupled protein receptors as $5HT_2R$ in HMs, and so 5-HT application and NE application for HMs can be considered more or less interchangeable at least in terms of PKC pathways.

Simulated 5-HT_{1A}R blockade is roughly equivalent to the application of the relatively new drug 4-Cyano-N-[(2R)-2-[4-(2,3-dihydro-1,4-benzodioxin-5-yl)-1-piperazinyl]propyl]-N-2-pyridinylbenzamide hydrochloride, otherwise known as Lecozotan (Schechter et al 2005). Lecozotan is a specific 5-HT_{1A}R blocker, and is currently being investigated as a treatment for Alzheimer's disease (Moser et al 2012).

Simulated PKC corresponds to the pharmacological agent Gö 6976, a PKC blocker (Martiny-Baron et al 1993). PKC agonists can be used to recover downstream effects blocked by antagonists, or effects not receiving sufficient input to produce an output. The agonist phorbol 12-myristate 13-acetate (PMA) is simulated here (Han & Bakker 2006).

Simulated MAPK blockade can be performed experimentally via the antagonist SB203580 (Keifer et al 2007), which works without modifying Ca^{2+} release via InsP3R or modifying PKC phosphorylation of AMPAR.

H8. Conclusions

The role of 5-HT on the HM is multifaceted, and age dependent. Ranging from modifications to intracellular Ca^{2+} in both the cytosol and microdomains, to complex manipulations of AMPAR, both in terms of insertion and upregulation, 5-HT modifies a broad number of mechanisms in the HM associated with the regulation of firing frequency. Without these mechanisms, HMs would be unable to mobilize to counteract both short and long-term hypoxic conditions.

While intracellular Ca^{2+} in this project has centered around excitability, and its role in firing frequency, with secondary messenger modification a secondary focus, intracellular Ca^{2+} can play an extremely powerful role in a variety of behaviors not addressed. Potentially investigating changes to synaptic release, additional secondary messengers, or glia could permit for additional behaviors to be added to the model. Otherwise, we feel satisfied in the number of behaviors successfully matched using our otherwise simple Ca^{2+} diffusion model.

STF has been effectively studied during early scientific forays into 5-HT's effect on HMs, although most of these studies focus more on the hypoglossal motor nucleus, and cranial nerve XII than on individual HMs. Based on the three HM models presented, STF in the isolated HM may be quite a bit more complex in its behavior than a simple square wave response. Because of this, it may be of value to look more seriously into the various facets of the STF response biologically, and determine whether many of the secondary properties occurring during LTF in the model are similarly paralleled in biological preparations.

As the primary object of study for this project, and far and away the most computationally intensive simulations to run, LTF has been thoroughly characterized computationally, and is now ready to see the hypotheses associated with it tested in actual biological systems. The curious dichotomy between PKC as initiator, MAPK cascades as both the accumulator and maintainer, with the adjoining chemical reactions involved in

performing derivatives on incoming signals, makes this system incredibly unique. However, given the usefulness of counting the number of incoming stimulations, we would be entirely unsurprised if mathematically similar system appeared throughout biology. Certainly this work can be viewed as an extension to the Purvis and Butera (2005) model for investigating suitable hypotheses to answer questions posed in Feldman et al (2005) pertaining to ivLTF's underlying mechanisms. While ivLTF remains a relatively small and new field of inquiry, it cuts to the core of respiratory plasticity: the molecular mechanisms behind LTF at the cellular level. Here, in particular, models can serve as an excellent tool for winnowing down possible mechanisms in an otherwise vast sea of putative biochemical reactions.

Theoretically, there are always more behaviors to reduce, and models to strip down to their fundamental components. While through the course of this project, three three distinct developmental age groups in the full HM model have been thoroughly characterized, we are still working on an electrophysiological reduction of the developmental age groups that might shed even more light into the subtle differences between the neonatal, juvenile, and adult HM models that make them behave so differently, despite only a handful of parametric differences. In the near future we hope to achieve such reduced models, which we feel would perfectly complement the three full HM models presented here. Additionally, given the reduced LTF model presented here, it would be quite simple to take reduced developmental models, and test them against the full HM model, in terms of firing frequency output during a simulated LTF paradigm.

This project has also mainly focused in the single HM. However, with the reduced models currently in hand, and developmental reduced models expected in the near future, this system is ripe for a transition from single HM to full nXII. As a full nucleus model, we would be in a position to better match data from biological experiments, where actual recordings could be compared directly to the model's electrical output. Alternately, we could move in the opposite direction, adding more realism our single HM model, potentially adding additional compartments for dendrites. As noted in the Background & Significance section, a good deal is known about the morphology of rat HMs through development, and so this could be another avenue of investigation to explore moving forward. Certain voltage-gated Ca^{2+} channels in particular are known to exist in spatially distinct locations along the dendrites, which could additionally allow for dendritic Ca^{2+} dynamics to be studied in greater detail.

Rather than adding layers of detail to the HM model directly, instead more detailed simulated physiology upstream of the HM could also add additional dimensions to the model. As previously stated, LTF in the three developmental HM models is restricted to amplitude LTF, as frequency LTF requires an increase in inter-burst-intervals, which is not possible for the XII, which is driven by rhythmic input, and does not intrinsically burst on its own. By modeling the glutamatergic interneurons that link the Pre-Bötzinger complex to HMs, the capacity to modulate burst frequency in a respiratory circuit simulation becomes possible. In effect, this would also allow for an investigation of how amplitude and frequency LTF, which frequently come paired in biological studies of the respiratory system, combine and interact in the HM models.

While there are many potentially future directions for this project, from additional reductions to expansion of the model into either a full nXII, or a more in-depth single cell, complete with a detailed dendritic tree, we feel that the work done here is wholly

sufficient in presenting both full and reduced models of the HM's response to 5-HT. The capacity to replicate various known behaviors is a testament to the sufficiency of the model as it stands to describe phenomena like LTF at the single-cell level, and provide a reasonable explanation for its initiation, maintenance, and disruption in pathological states.

I. Bibliography

Abdala AP, Rybak IA, Smith JC, Zoccal DB, Machado BH, et al. 2009. Multiple pontomedullary mechanisms of respiratory rhythmogenesis. *Respir Physiol Neurobiol* 168: 19-25

Aldes LD. 1990. Topographically organized projections from the nucleus subceruleus to the hypoglossal nucleus in the rat: a light and electron microscopic study with complementary axonal transport techniques. *J Comp Neurol* 302: 643-56

Aldes LD, Chapman ME, Chronister RB, Haycock JW. 1992. Sources of noradrenergic afferents to the hypoglossal nucleus in the rat. *Brain Res Bull* 29: 931-42

Allbritton NL, Meyer T, Stryer L. 1992. Range of messenger action of calcium ion and inositol 1, 4, 5-trisphosphate. *Science (New York, NY)* 258: 1812

Amini B, Bidani A, Zwischenberger JB, Clark JW, Jr. 2004. A model of the rat phrenic motor neuron. *IEEE Trans Biomed Eng* 51: 1103-14

Antebi A, Fink GR. 1992. The yeast Ca (2+)-ATPase homologue, PMR1, is required for normal Golgi function and localizes in a novel Golgi-like distribution. *Molecular biology of the cell* 3: 633

Athanasiades A, Clark J, Ghorbel F, Bidani A. 2000. An ionic current model for medullary respiratory neurons. *Journal of Computational Neuroscience* 9: 237-57

Bach KB, Mitchell GS. 1996. Hypoxia-induced long-term facilitation of respiratory activity is serotonin dependent. *Respir Physiol* 104: 251-60

Baker-Herman TL, Mitchell GS. 2008. Determinants of frequency long-term facilitation following acute intermittent hypoxia in vagotomized rats. *Respiratory physiology & neurobiology* 162: 8-17

Baker-Herman TL, Strey KA. 2011. Similarities and differences in mechanisms of phrenic and hypoglossal motor facilitation. *Respiratory physiology & neurobiology* 179: 48-56

Baker TL, Mitchell GS. 2000. Episodic but not continuous hypoxia elicits long-term facilitation of phrenic motor output in rats. *J Physiol* 529 Pt 1: 215-9

Barsh LI. 1999. The Origin of Pharyngeal Obstruction during Sleep. *Sleep Breath* 3: 17-22

Bass NH, Morrell RM. 1997. The Neurology of Swallowing In *Dysphagia : diagnosis and management*, pp. 23-33. Boston: Butterworth-Heinemann

Bayliss DA, Umemiya M, Berger AJ. 1995. Inhibition of N- and P-type calcium currents and the after-hyperpolarization in rat motoneurones by serotonin. *J Physiol* 485 (Pt 3): 635-47

Bayliss DA, Viana F, Bellingham MC, Berger AJ. 1994a. Characteristics and postnatal development of a hyperpolarization-activated inward current in rat hypoglossal motoneurons in vitro. *J Neurophysiol* 71: 119-28

Bayliss DA, Viana F, Berger AJ. 1994b. Effects of thyrotropin-releasing hormone on rat motoneurons are mediated by G proteins. *Brain Res* 668: 220-9

Behan M, Brownfield MS. 1999. Age-related changes in serotonin in the hypoglossal nucleus of rat: implications for sleep-disordered breathing. *Neuroscience letters* 267: 133-36

Bellingham MC, Berger AJ. 1996. Presynaptic depression of excitatory synaptic inputs to rat hypoglossal motoneurons by muscarinic M2 receptors. *J Neurophysiol* 76: 3758-70

Berg AP, Talley EM, Manger JP, Bayliss DA. 2004. Motoneurons express heteromeric TWIK-related acid-sensitive K+ (TASK) channels containing TASK-1 (KCNK3) and TASK-3 (KCNK9) subunits. *J Neurosci* 24: 6693-702

Berger AJ, Takahashi T. 1990. Serotonin enhances a low-voltage-activated calcium current in rat spinal motoneurons. *J Neurosci* 10: 1922-8

Berridge MJ. 1987. Inositol trisphosphate and diacylglycerol: two interacting second messengers. *Annual review of biochemistry* 56: 159-93

Berridge MJ. 1997. Elementary and global aspects of calcium signalling. *Journal of experimental biology* 200: 315-19

Bianchi AL, Denavit-Saubie M, Champagnat J. 1995. Central control of breathing in mammals: neuronal circuitry, membrane properties, and neurotransmitters. *Physiol Rev* 75: 1-45

Blaustein M, Hodgkin A. 1969. The effect of cyanide on the efflux of calcium from squid axons. *The Journal of physiology* 200: 497-527

Bocchiaro CM, Feldman JL. 2004. Synaptic activity-independent persistent plasticity in endogenously active mammalian motoneurons. *Proceedings of the National Academy of Sciences* 101: 4292-95

Boehm J, Kang M-G, Johnson RC, Esteban J, Huganir RL, Malinow R. 2006. Synaptic incorporation of AMPA receptors during LTP is controlled by a PKC phosphorylation site on GluR1. *Neuron* 51: 213-25

Borke RC, Nau ME, Ringler RL, Jr. 1983. Brain stem afferents of hypoglossal neurons in the rat. *Brain Res* 269: 47-55

Bourgin P, Escourrou P, Gaultier C, Adrien J. 1995. Induction of rapid eye movement sleep by carbachol infusion into the pontine reticular formation in the rat. *Neuroreport* 6: 532-6

Bowker RM, Westlund KN, Sullivan MC, Wilber JF, Coulter JD. 1983. Descending serotonergic, peptidergic and cholinergic pathways from the raphe nuclei: a multiple transmitter complex. *Brain Res* 288: 33-48

Breen S, Rees S, Walker D. 1997. Identification of brainstem neurons responding to hypoxia in fetal and newborn sheep. *Brain Res* 748: 107-21

Brockhaus J, Ballanyi K, Smith JC, Richter DW. 1993. Microenvironment of respiratory neurons in the in vitro brainstem-spinal cord of neonatal rats. *J Physiol* 462: 421-45

Butera RJ, Jr., Rinzel J, Smith JC. 1999a. Models of respiratory rhythm generation in the pre-Botzinger complex. I. Bursting pacemaker neurons. *J Neurophysiol* 82: 382-97

Butera RJ, Jr., Rinzel J, Smith JC. 1999b. Models of respiratory rhythm generation in the pre-Botzinger complex. II. Populations Of coupled pacemaker neurons. *J Neurophysiol* 82: 398-415

Chan-Palay V, Jonsson G, Palay SL. 1978. Serotonin and substance P coexist i, neurons of the rat's central nervous system. *Proc Natl Acad Sci U S A* 75: 1582-6

Chung HJ, Xia J, Scannevin RH, Zhang X, Huganir RL. 2000. Phosphorylation of the AMPA receptor subunit GluR2 differentially regulates its interaction with PDZ domain-containing proteins. *The Journal of neuroscience* 20: 7258-67

Connaughton M, Priestley JV, Sofroniew MV, Eckenstein F, Cuello AC. 1986. Inputs to motoneurones in the hypoglossal nucleus of the rat: light and electron microscopic immunocytochemistry for choline acetyltransferase, substance P and enkephalins using monoclonal antibodies. *Neuroscience* 17: 205-24

Cuthbertson KS, Chay TR. 1991. Modelling receptor-controlled intracellular calcium oscillators. *Cell Calcium* 12: 97-109

Del Negro CA, Chandler SH. 1998. Regulation of intrinsic and synaptic properties of neonatal rat trigeminal motoneurons by metabotropic glutamate receptors. *J Neurosci* 18: 9216-26

Del Negro CA, Johnson SM, Butera RJ, Smith JC. 2001. Models of respiratory rhythm generation in the pre-Botzinger complex. III. Experimental tests of model predictions. *J Neurophysiol* 86: 59-74

Di Pasquale E, Tell F, Ptak K, Monteau R, Hilaire G. 2001. Perinatal changes of I(h) in phrenic motoneurons. *Eur J Neurosci* 13: 1403-10

Dipolo R, Beaugé L. 2006. Sodium/calcium exchanger: influence of metabolic regulation on ion carrier interactions. *Physiological reviews* 86: 155-203

Dobbins EG, Feldman JL. 1994. Brainstem network controlling descending drive to phrenic motoneurons in rat. *J Comp Neurol* 347: 64-86

Dong XW, Morin D, Feldman JL. 1996. Multiple actions of 1S,3R-ACPD in modulating endogenous synaptic transmission to spinal respiratory motoneurons. *J Neurosci* 16: 4971-82

Duffin J. 2004. Functional organization of respiratory neurones: a brief review of current questions and speculations. *Exp Physiol* 89: 517-29

Earnshaw BA, Bressloff PC. 2006. Biophysical model of AMPA receptor trafficking and its regulation during long-term potentiation/long-term depression. *The Journal of neuroscience* 26: 12362-73

Engel J, Schultens HA, Schild D. 1999. Small conductance potassium channels cause an activity-dependent spike frequency adaptation and make the transfer function of neurons logarithmic. *Biophys J* 76: 1310-9

Feldman JL, Del Negro CA. 2006. Looking for inspiration: new perspectives on respiratory rhythm. *Nat Rev Neurosci* 7: 232-42

Feldman JL, Janczewski WA. 2006. Point:Counterpoint: The parafacial respiratory group (pFRG)/pre-Botzinger complex (preBotC) is the primary site of respiratory rhythm generation in the mammal. Counterpoint: the preBotC is the primary site

of respiratory rhythm generation in the mammal. *J Appl Physiol* 100: 2096-7; discussion 97-8, 103-8
Feldman JL, Loewy AD, Speck DF. 1985. Projections from the ventral respiratory group to phrenic and intercostal motoneurons in cat: an autoradiographic study. *J Neurosci* 5: 1993-2000
Feldman JL, McCrimmon D. 2008. Neural Control of Breathing In *Fundamental neuroscience*, pp. 855-72. Amsterdam ; Boston: Elsevier / Academic Press
Feldman JL, Mitchell GS, Nattie EE. 2003. Breathing: rhythmicity, plasticity, chemosensitivity. *Annu Rev Neurosci* 26: 239-66
Feldman JL, Neverova NV, Saywell SA. 2005. Modulation of hypoglossal motoneuron excitability by intracellular signal transduction cascades. *Respir Physiol Neurobiol* 147: 131-43
Fenik VB, Davies RO, Kubin L. 2005. REM sleep-like atonia of hypoglossal (XII) motoneurons is caused by loss of noradrenergic and serotonergic inputs. *Am J Respir Crit Care Med* 172: 1322-30
Filiano J, Kinney H. 1994. A perspective on neuropathologic findings in victims of the sudden infant death syndrome: the triple-risk model. *Neonatology* 65: 194-97
Fisher ND, Nistri A. 1993. Substance P and TRH share a common effector pathway in rat spinal motoneurones: an in vitro electrophysiological investigation. *Neurosci Lett* 153: 115-9
Fregosi RF, Fuller DD. 1997. Respiratory-related control of extrinsic tongue muscle activity. *Respir Physiol* 110: 295-306
Fuller D, Zabka A, Baker T, Mitchell G. 2001. Selected contribution: phrenic long-term facilitation requires 5-HT receptor activation during but not following episodic hypoxia. *Journal of Applied Physiology* 90
Fuller DD, Bach KB, Baker TL, Kinkead R, Mitchell GS. 2000. Long term facilitation of phrenic motor output. *Respir Physiol* 121: 135-46
Furusawa K, Yamaoka M, Kogo M, Matsuya T. 1991. The innervation of the levator veli palatini muscle by the glossopharyngeal nerve. *Brain Res Bull* 26: 599-604
Gilliam EE, Goldberg SJ. 1995. Contractile properties of the tongue muscles: effects of hypoglossal nerve and extracellular motoneuron stimulation in rat. *J Neurophysiol* 74: 547-55
Golomb D, Amitai Y. 1997. Propagating neuronal discharges in neocortical slices: computational and experimental study. *Journal of Neurophysiology* 78: 1199-211
Gray PA, Janczewski WA, Mellen N, McCrimmon DR, Feldman JL. 2001. Normal breathing requires preBotzinger complex neurokinin-1 receptor-expressing neurons. *Nat Neurosci* 4: 927-30
Greer J, Smith J, Feldman J. 1991. Role of excitatory amino acids in the generation and transmission of respiratory drive in neonatal rat. *The Journal of physiology* 437: 727-49
Grunnet M, Jespersen T, Perrier JF. 2004. 5-HT1A receptors modulate small-conductance Ca2+-activated K+ channels. *J Neurosci Res* 78: 845-54
Haddad GG, Donnelly DF, Getting PA. 1990. Biophysical properties of hypoglossal neurons in vitro: intracellular studies in adult and neonatal rats. *J Appl Physiol* 69: 1509-17

Han R, Bakker AJ. 2006. The effect of the PKC inhibitor calphostin C and the PKC agonist phorbol 12-myristate 13-acetate on regulation of cytosolic Ca< sup> 2+</sup> in mammalian skeletal muscle cells. *Toxicology and applied pharmacology* 212: 247-55

Hao L, Rigaud J-L, Inesi G. 1994. Ca2+/H+ countertransport and electrogenicity in proteoliposomes containing erythrocyte plasma membrane Ca-ATPase and exogenous lipids. *Journal of Biological Chemistry* 269: 14268-75

Harvey PJ, Li X, Li Y, Bennett DJ. 2006. 5-HT2 receptor activation facilitates a persistent sodium current and repetitive firing in spinal motoneurons of rats with and without chronic spinal cord injury. *J Neurophysiol* 96: 1158-70

Henry EC, Sarko DK, Catania KC. 2008. Central projections of trigeminal afferents innervating the face in naked mole-rats (Heterocephalus glaber). *Anat Rec (Hoboken)* 291: 988-98

Henry JN, Manaker S. 1998. Colocalization of substance P or enkephalin in serotonergic neuronal afferents to the hypoglossal nucleus in the rat. *J Comp Neurol* 391: 491-505

Holstege JC. 1991. Ultrastructural evidence for GABAergic brain stem projections to spinal motoneurons in the rat. *J Neurosci* 11: 159-67

Holstege JC, Kuypers HG. 1987. Brainstem projections to spinal motoneurons: an update. *Neuroscience* 23: 809-21

Hornby PJ. 2001. Central neurocircuitry associated with emesis. *Am J Med* 111 Suppl 8A: 106S-12S

Hounsgaard J, Kiehn O. 1989. Serotonin-induced bistability of turtle motoneurones caused by a nifedipine-sensitive calcium plateau potential. *J Physiol* 414: 265-82

Hsiao CF, Trueblood PR, Levine MS, Chandler SH. 1997. Multiple effects of serotonin on membrane properties of trigeminal motoneurons in vitro. *J Neurophysiol* 77: 2910-24

Janczewski WA, Feldman JL. 2006. Distinct rhythm generators for inspiration and expiration in the juvenile rat. *J Physiol* 570: 407-20

Jean A. 2001. Brain stem control of swallowing: neuronal network and cellular mechanisms. *Physiol Rev* 81: 929-69

Karschin C, Dissmann E, Stuhmer W, Karschin A. 1996. IRK(1-3) and GIRK(1-4) inwardly rectifying K+ channel mRNAs are differentially expressed in the adult rat brain. *J Neurosci* 16: 3559-70

Keifer J, Zheng Z-Q, Zhu D. 2007. MAPK signaling pathways mediate AMPA receptor trafficking in an in vitro model of classical conditioning. *Journal of Neurophysiology* 97: 2067-74

Kinkead R, Mitchell GS. 1999. Time-dependent hypoxic ventilatory responses in rats: effects of ketanserin and 5-carboxamidotryptamine. *Am J Physiol* 277: R658-66

Kinney HC, Belliveau RA, Trachtenberg FL, Rava LA, Paterson DS. 2007. The development of the medullary serotonergic system in early human life. *Auton Neurosci* 132: 81-102

Kobler JB, Datta S, Goyal RK, Benecchi EJ. 1994. Innervation of the larynx, pharynx, and upper esophageal sphincter of the rat. *J Comp Neurol* 349: 129-47

Koch C, Segev I. 1989. Methods in neural modeling. MIT Press Cambridge, Mass

Koizumi H, Wilson CG, Wong S, Yamanishi T, Koshiya N, Smith JC. 2008. Functional imaging, spatial reconstruction, and biophysical analysis of a respiratory motor circuit isolated in vitro. *J Neurosci* 28: 2353-65

Koshiya N, Guyenet PG. 1996. Tonic sympathetic chemoreflex after blockade of respiratory rhythmogenesis in the rat. *J Physiol* 491 (Pt 3): 859-69

Kraiczi H, Hedner J, Dahlöf P, Ejnell H, Carlson J. 1999. Effect of serotonin uptake inhibition on breathing during sleep and daytime symptoms in obstructive sleep apnea. *Sleep* 22: 61

Kristensson K, Olsson Y. 1971. Uptake and retrograde axonal transport of peroxidase in hypoglossal neurons. Electron microscopical localization in the neuronal perikaryon. *Acta Neuropathol* 19: 1-9

Ladewig T, Lalley PM, Keller BU. 2004. Serotonergic modulation of intracellular calcium dynamics in neonatal hypoglossal motoneurons from mouse. *Brain research* 1001: 1-12

Lape R, Nistri A. 1999. Voltage-activated K+ currents of hypoglossal motoneurons in a brain stem slice preparation from the neonatal rat. *J Neurophysiol* 81: 140-8

Lape R, Nistri A. 2000. Current and voltage clamp studies of the spike medium afterhyperpolarization of hypoglossal motoneurons in a rat brain stem slice preparation. *J Neurophysiol* 83: 2987-95

Larkman PM, Kelly JS. 1997. Modulation of IH by 5-HT in neonatal rat motoneurones in vitro: mediation through a phosphorylation independent action of cAMP. *Neuropharmacology* 36: 721-33

Larkman PM, Kelly JS. 1998. Characterization of 5-HT-sensitive potassium conductances in neonatal rat facial motoneurones in vitro. *J Physiol* 508 (Pt 1): 67-81

Li Y, Bennett DJ. 2003. Persistent sodium and calcium currents cause plateau potentials in motoneurons of chronic spinal rats. *J Neurophysiol* 90: 857-69

Li YQ, Takada M, Kaneko T, Mizuno N. 1997. Distribution of GABAergic and glycinergic premotor neurons projecting to the facial and hypoglossal nuclei in the rat. *J Comp Neurol* 378: 283-94

Liao D, Scannevin RH, Huganir R. 2001. Activation of silent synapses by rapid activity-dependent synaptic recruitment of AMPA receptors. *The Journal of neuroscience* 21: 6008-17

Ling L. 2008. Serotonin and NMDA receptors in respiratory long-term facilitation. *Respiratory physiology & neurobiology* 164: 233-41

Lingenhohl K, Friauf E. 1994. Giant neurons in the rat reticular formation: a sensorimotor interface in the elementary acoustic startle circuit? *J Neurosci* 14: 1176-94

Lips MB, Keller BU. 1998. Endogenous calcium buffering in motoneurones of the nucleus hypoglossus from mouse. *The Journal of physiology* 511: 105-17

Liu Q, Wong-Riley MT. 2008. Postnatal changes in the expression of serotonin 2A receptors in various brain stem nuclei of the rat. *J Appl Physiol* 104: 1801-8

Liu Q, Wong-Riley MT. 2010a. Postnatal changes in the expressions of serotonin 1A, 1B, and 2A receptors in ten brain stem nuclei of the rat: implication for a sensitive period. *Neuroscience* 165: 61-78

Liu Q, Wong-Riley MT. 2010b. Postnatal changes in tryptophan hydroxylase and serotonin transporter immunoreactivity in multiple brainstem nuclei of the rat: Implications for a sensitive period. *J Comp Neurol* 518: 1082-97

Liu X, Sood S, Liu H, Horner RL. 2005. Opposing muscarinic and nicotinic modulation of hypoglossal motor output to genioglossus muscle in rats in vivo. *J Physiol* 565: 965-80

Lu W-Y, Man H-Y, Ju W, Trimble WS, MacDonald JF, Wang YT. 2001. Activation of synaptic NMDA receptors induces membrane insertion of new AMPA receptors and LTP in cultured hippocampal neurons. *Neuron* 29: 243-54

MacGregor RJ. 1987. *Neural and brain modeling*. San Diego, Calif.: Academic Press. xii, 643 p. pp.

Manaker S, Tischler LJ. 1993. Origin of serotoninergic afferents to the hypoglossal nucleus in the rat. *J Comp Neurol* 334: 466-76

Marks JD, Donnelly DF, Haddad GG. 1993. Adenosine-induced inhibition of vagal motoneuron excitability: receptor subtype and mechanisms. *Am J Physiol* 264: L124-32

Martin-Caraballo M, Greer JJ. 2001. Voltage-sensitive calcium currents and their role in regulating phrenic motoneuron electrical excitability during the perinatal period. *J Neurobiol* 46: 231-48

Martiny-Baron G, Kazanietz MG, Mischak H, Blumberg PM, Kochs G, et al. 1993. Selective inhibition of protein kinase C isozymes by the indolocarbazole Gö 6976. *Journal of Biological Chemistry* 268: 9194-97

McEnery MW, Vance CL, Begg CM, Lee W-L, Choi Y, Dubel SJ. 1998. Differential expression and association of calcium channel subunits in development and disease. *Journal of bioenergetics and biomembranes* 30: 409-18

McGuire M, Zhang Y, White DP, Ling L. 2004. Serotonin receptor subtypes required for ventilatory long-term facilitation and its enhancement after chronic intermittent hypoxia in awake rats. *Am J Physiol Regul Integr Comp Physiol* 286: R334-41

McKay LC, Janczewski WA, Feldman JL. 2004. Episodic hypoxia evokes long-term facilitation of genioglossus muscle activity in neonatal rats. *The Journal of physiology* 557: 13-18

McLarnon JG. 1995. Potassium currents in motoneurones. *Prog Neurobiol* 47: 513-31

Miles GB, Lipski J, Lorier AR, Laslo P, Funk GD. 2004. Differential expression of voltage-activated calcium channels in III and XII motoneurones during development in the rat. *European Journal of Neuroscience* 20: 903-13

Mons N, Decorte L, Jaffard R, Cooper D. 1998. Ca< sup> 2+</sup>-sensitive adenylyl cyclases, key integrators of cellular signalling. *Life sciences* 62: 1647-52

Moser U, Kaser S, Winkler D. 2012. DFP: Therapie der Alzheimer-Demenz: Status quo und Zukunftsperspektiven. *Journal für Neurologie, Neurochirurgie und Psychiatrie* 11: 72-78

Mosfeldt Laursen A, Rekling JC. 1989. Electrophysiological properties of hypoglossal motoneurons of guinea-pigs studied in vitro. *Neuroscience* 30: 619-37

Moss I. 2005. Neural Control of Breathing In *Physiologic basis of respiratory disease*, pp. 251-61. Hamilton: BC Decker, Inc.

Mynlieff M, Beam KG. 1994. Adenosine acting at an A1 receptor decreases N-type calcium current in mouse motoneurons. *J Neurosci* 14: 3628-34

Narita N, Narita M, Takashima S, Nakayama M, Nagai T, Okado N. 2001. Serotonin transporter gene variation is a risk factor for sudden infant death syndrome in the Japanese population. *Pediatrics* 107: 690-92

Neverova NV, Saywell SA, Nashold LJ, Mitchell GS, Feldman JL. 2007. Episodic stimulation of α1-adrenoreceptors induces protein kinase C-dependent persistent changes in motoneuronal excitability. *The Journal of neuroscience* 27: 4435-42

Nicholas AP, Pieribone VA, Arvidsson U, Hokfelt T. 1992. Serotonin-, substance P- and glutamate/aspartate-like immunoreactivities in medullo-spinal pathways of rat and primate. *Neuroscience* 48: 545-59

Niggli V, Sigel E, Carafoli E. 1982. The purified Ca2+ pump of human erythrocyte membranes catalyzes an electroneutral Ca2+-H+ exchange in reconstituted liposomal systems. *Journal of Biological Chemistry* 257: 2350-56

Núñez-Abades P, Cameron W. 1995. Morphology of developing rat genioglossal motoneurons studied in vitro: relative changes in diameter and surface area of somata and dendrites. *The Journal of comparative neurology* 353: 129-42

Nunez-Abades P, He F, Barrionuevo G, Cameron W. 1994. Morphology of developing rat genioglossal motoneurons studied in vitro: changes in length, branching pattern, and spatial distribution of dendrites. *Journal of comparative neurology* 339: 401-20

Nygren LG, Olson L. 1977. A new major projection from locus coeruleus: the main source of noradrenergic nerve terminals in the ventral and dorsal columns of the spinal cord. *Brain Res* 132: 85-93

O'Brien RJ, Xu D, Petralia RS, Steward O, Huganir RL, Worley P. 1999. Synaptic clustering of AMPA receptors by the extracellular immediate-early gene product Narp. *NEURON-CAMBRIDGE MA*- 23: 309-23

Onimaru H, Homma I. 2003. A novel functional neuron group for respiratory rhythm generation in the ventral medulla. *J Neurosci* 23: 1478-86

Ono T, Ishiwata Y, Inaba N, Kuroda T, Nakamura Y. 1994. Hypoglossal premotor neurons with rhythmical inspiratory-related activity in the cat: localization and projection to the phrenic nucleus. *Exp Brain Res* 98: 1-12

Panigrahy A, Filiano J, Sleeper LA, Mandell F, Valdes-Dapena M, et al. 2000. Decreased serotonergic receptor binding in rhombic lip-derived regions of the medulla oblongata in the sudden infant death syndrome. *Journal of Neuropathology & Experimental Neurology* 59: 377-84

Parkis MA, Bayliss DA, Berger AJ. 1995. Actions of norepinephrine on rat hypoglossal motoneurons. *J Neurophysiol* 74: 1911-9

Parkis MA, Berger AJ. 1997. Clonidine reduces hyperpolarization-activated inward current (Ih) in rat hypoglossal motoneurons. *Brain Res* 769: 108-18

Paton JF. 1996. The ventral medullary respiratory network of the mature mouse studied in a working heart-brainstem preparation. *J Physiol* 493 (Pt 3): 819-31

Paton JF, Richter DW. 1995. Role of fast inhibitory synaptic mechanisms in respiratory rhythm generation in the maturing mouse. *J Physiol* 484 (Pt 2): 505-21

Pedarzani P, Kulik A, Muller M, Ballanyi K, Stocker M. 2000. Molecular determinants of Ca2+-dependent K+ channel function in rat dorsal vagal neurones. *J Physiol* 527 Pt 2: 283-90

Peever JH, Shen L, Duffin J. 2002. Respiratory pre-motor control of hypoglossal motoneurons in the rat. *Neuroscience* 110: 711-22
Portas C, Bjorvatn B, Fagerland S, Grønli J, Mundal V, et al. 1998. On-line detection of extracellular levels of serotonin in dorsal raphe nucleus and frontal cortex over the sleep/wake cycle in the freely moving rat. *Neuroscience* 83: 807-14
Powers RK, Binder MD. 2003. Persistent sodium and calcium currents in rat hypoglossal motoneurons. *J Neurophysiol* 89: 615-24
Press WH. 1992. *Numerical recipes in Fortran 77: the art of scientific computing*. Cambridge university press.
Purvis LK, Butera RJ. 2005. Ionic current model of a hypoglossal motoneuron. *J Neurophysiol* 93: 723-33
Qiao L, Nachbar RB, Kevrekidis IG, Shvartsman SY. 2007. Bistability and oscillations in the Huang-Ferrell model of MAPK signaling. *PLoS Computational Biology* 3: e184
Rekling JC. 1990. Excitatory effects of thyrotropin-releasing hormone (TRH) in hypoglossal motoneurons. *Brain Res* 510: 175-9
Rekling JC, Funk GD, Bayliss DA, Dong XW, Feldman JL. 2000. Synaptic control of motoneuronal excitability. *Physiol Rev* 80: 767-852
Richter DW, Spyer KM. 2001. Studying rhythmogenesis of breathing: comparison of in vivo and in vitro models. *Trends Neurosci* 24: 464-72
Rikard-Bell GC, Bystrzycka EK, Nail BS. 1984. Brainstem projections to the phrenic nucleus: a HRP study in the cat. *Brain Res Bull* 12: 469-77
Rukhadze I, Kubin L. 2007. Mesopontine cholinergic projections to the hypoglossal motor nucleus. *Neurosci Lett* 413: 121-5
Safronov BV, Vogel W. 1996. Properties and functions of Na(+)-activated K+ channels in the soma of rat motoneurones. *J Physiol* 497 (Pt 3): 727-34
Saito Y, Ezure K, Tanaka I. 2002. Difference between hypoglossal and phrenic activities during lung inflation and swallowing in the rat. *J Physiol* 544: 183-93
Schechter LE, Smith D, Rosenzweig-Lipson S, Sukoff S, Dawson L, et al. 2005. Lecozotan (SRA-333): a selective serotonin 1A receptor antagonist that enhances the stimulated release of glutamate and acetylcholine in the hippocampus and possesses cognitive-enhancing properties. *Journal of Pharmacology and Experimental Therapeutics* 314: 1274-89
Schreiber M, Salkoff L. 1997. A novel calcium-sensing domain in the BK channel. *Biophys J* 73: 1355-63
Schulz B, Lambertz M, Schulz G, Langhorst P. 1983. Reticular formation of the lower brainstem. A common system for cardiorespiratory and somatomotor functions: discharge patterns of neighboring neurons influenced by somatosensory afferents. *J Auton Nerv Syst* 9: 433-49
Schutter ED. 2009. *Computational modeling methods for neuroscientists*. The MIT Press.
Shannon R, Baekey DM, Morris KF, Li Z, Lindsey BG. 2000. Functional connectivity among ventrolateral medullary respiratory neurones and responses during fictive cough in the cat. *J Physiol* 525 Pt 1: 207-24
Shannon R, Baekey DM, Morris KF, Lindsey BG. 1998. Ventrolateral medullary respiratory network and a model of cough motor pattern generation. *J Appl Physiol* 84: 2020-35

Smallwood JI, Waisman D, Lafreniere D, Rasmussen H. 1983. Evidence that the erythrocyte calcium pump catalyzes a Ca2+: nH+ exchange. *Journal of Biological Chemistry* 258: 11092-97

Smith JC, Butera RJ, Koshiya N, Del Negro C, Wilson CG, Johnson SM. 2000. Respiratory rhythm generation in neonatal and adult mammals: the hybrid pacemaker-network model. *Respir Physiol* 122: 131-47

Smith JC, Ellenberger HH, Ballanyi K, Richter DW, Feldman JL. 1991. Pre-Botzinger complex: a brainstem region that may generate respiratory rhythm in mammals. *Science* 254: 726-9

Song I, Huganir RL. 2002. Regulation of AMPA receptors during synaptic plasticity. *Trends in neurosciences* 25: 578-88

St-John WM, Paton JF, Leiter JC. 2004. Uncoupling of rhythmic hypoglossal from phrenic activity in the rat. *Exp Physiol* 89: 727-37

Sugimori M, Lang EJ, Silver RB, Llinás R. 1994. High-resolution measurement of the time course of calcium-concentration microdomains at squid presynaptic terminals. *The Biological Bulletin* 187: 300-03

Takahashi T. 1990a. Inward rectification in neonatal rat spinal motoneurones. *J Physiol* 423: 47-62

Takahashi T. 1990b. Membrane currents in visually identified motoneurones of neonatal rat spinal cord. *J Physiol* 423: 27-46

Talley EM, Lei Q, Sirois JE, Bayliss DA. 2000. TASK-1, a two-pore domain K+ channel, is modulated by multiple neurotransmitters in motoneurons. *Neuron* 25: 399-410

Talley EM, Sadr NN, Bayliss DA. 1997. Postnatal development of serotonergic innervation, 5-HT1A receptor expression, and 5-HT responses in rat motoneurons. *J Neurosci* 17: 4473-85

Thomas GM, Huganir RL. 2004. MAPK cascade signalling and synaptic plasticity. *Nature Reviews Neuroscience* 5: 173-83

Thomas RC. 2009. The plasma membrane calcium ATPase (PMCA) of neurones is electroneutral and exchanges 2 H+ for each Ca2+ or Ba2+ ion extruded. *The Journal of physiology* 587: 315-27

Topert C, Doring F, Wischmeyer E, Karschin C, Brockhaus J, et al. 1998. Kir2.4: a novel K+ inward rectifier channel associated with motoneurons of cranial nerve nuclei. *J Neurosci* 18: 4096-105

Tsai H, Hewitt C, Buchholz J, Duckles S. 1997. Intracellular calcium buffering declines in aging adrenergic nerves. *Neurobiology of aging* 18: 229-33

Tsao TH, Butera RJ. 2008. Computational model of TASK channels and PKC-pathway dependent serotonergic modulatory effects in respiratory-related neurons. *Adv Exp Med Biol* 605: 382-6

Umemiya M, Berger AJ. 1994. Properties and function of low- and high-voltage-activated Ca2+ channels in hypoglossal motoneurons. *J Neurosci* 14: 5652-60

Umemiya M, Berger AJ. 1995. Single-channel properties of four calcium channel types in rat motoneurons. *J Neurosci* 15: 2218-24

Upadhyay J, Knudsen J, Anderson J, Becerra L, Borsook D. 2008. Noninvasive mapping of human trigeminal brainstem pathways. *Magn Reson Med* 60: 1037-46

Ursin R. 2002. Serotonin and sleep. *Sleep Med Rev* 6: 55-69

Van Baelen K, Vanoevelen J, Missiaen L, Raeymaekers L, Wuytack F. 2001. The Golgi PMR1 P-type ATPase of Caenorhabditis elegans IDENTIFICATION OF THE GENE AND DEMONSTRATION OF CALCIUM AND MANGANESE TRANSPORT. *Journal of Biological Chemistry* 276: 10683-91

Viana F, Bayliss DA, Berger AJ. 1993. Multiple potassium conductances and their role in action potential repolarization and repetitive firing behavior of neonatal rat hypoglossal motoneurons. *J Neurophysiol* 69: 2150-63

Viana F, Bayliss DA, Berger AJ. 1995. Repetitive firing properties of developing rat brainstem motoneurones. *J Physiol* 486 (Pt 3): 745-61

Volgin DV, Rukhadze I, Kubin L. 2008. Hypoglossal premotor neurons of the intermediate medullary reticular region express cholinergic markers. *J Appl Physiol* 105: 1576-84

Weber A, Herz R, Reiss I. 1966. Study of the kinetics of calcium transport by isolated fragmented sarcoplasmic reticulum. *Biochem. Z* 345: 329-69

Weese-Mayer DE, Berry-Kravis EM, Maher BS, Silvestri JM, Curran ME, Marazita ML. 2003. Sudden infant death syndrome: association with a promoter polymorphism of the serotonin transporter gene. *American Journal of Medical Genetics Part A* 117: 268-74

Wong-Riley MT, Liu Q. 2008. Neurochemical and physiological correlates of a critical period of respiratory development in the rat. *Respir Physiol Neurobiol* 164: 28-37

Xia XM, Fakler B, Rivard A, Wayman G, Johnson-Pais T, et al. 1998. Mechanism of calcium gating in small-conductance calcium-activated potassium channels. *Nature* 395: 503-7

Xu XF, Tsai HJ, Li L, Chen YF, Zhang C, Wang GF. 2009. Modulation of leak K(+) channel in hypoglossal motoneurons of rats by serotonin and/or variation of pH value. *Sheng Li Xue Bao* 61: 305-16

Yu X, Carroll S, Rigaud J, Inesi G. 1993. H+ countertransport and electrogenicity of the sarcoplasmic reticulum Ca2+ pump in reconstituted proteoliposomes. *Biophysical journal* 64: 1232-42

Zhan G, Shaheen F, Mackiewicz M, Fenik P, Veasey S. 2002. Single cell laser dissection with molecular beacon polymerase chain reaction identifies 2A as the predominant serotonin receptor subtype in hypoglossal motoneurons. *Neuroscience* 113: 145-54

Zhou Z, Neher E. 1993. Mobile and immobile calcium buffers in bovine adrenal chromaffin cells. *The Journal of physiology* 469: 245-73

J. Appendix

J1. HH Models

Hodgkin-Huxley style models take the form of a set of ordinary differential equations (ODEs) that contain one voltage-based differential equation, and several other differential equations for each gating variable. The passive properties of such models can be readily derived from Kirchoff's laws as follows, presuming that *C* is the membrane's capacitance, *R* is the resistance of a given ion channel, *g=1/R* is the conductance through a given ion channel, and V_{rest} is the resting potential of a given ion channel:

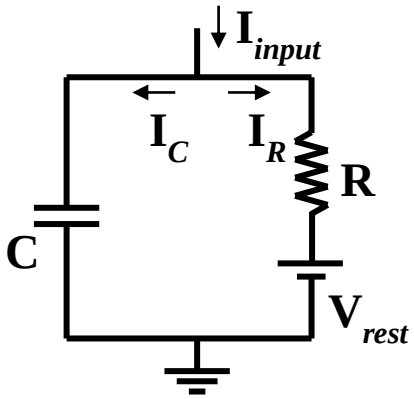

$$0 = I_{input} - I_C - I_R$$

$$0 = I_{input} - C\frac{dV}{dt} - \left(\frac{V - V_{rest}}{R}\right)$$

$$C\frac{dV}{dt} = I_{input} - \frac{1}{R}(V - V_{rest})$$

$$C\frac{dV}{dt} = I_{input} - g(V - V_{rest})$$

We can further extend these models to include an arbitrary number of ion channels, where *E* now represents the reversal potential for a given channel.

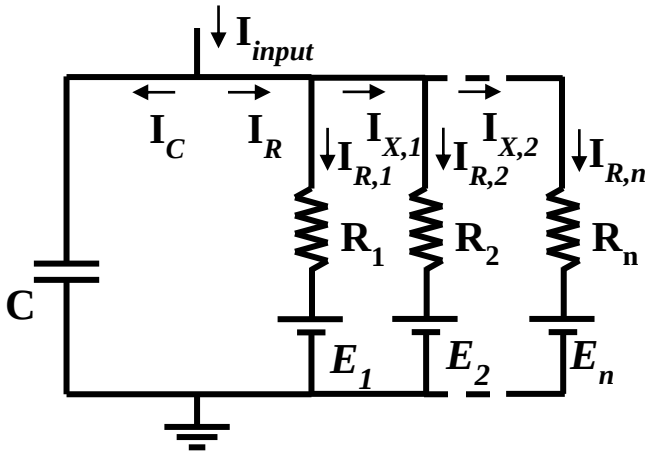

$$0 = I_{input} - I_C - I_R$$

$$0 = I_{input} - I_C - (I_{R,1} + I_{X,1})$$

$$0 = I_{input} - I_C - (I_{R,1} + (I_{R,2} + ...(I_{R,n})...))$$

$$0 = I_{input} - I_C - \sum_{i=1}^{n} I_{R,i}$$

$$C\frac{dV}{dt} = I_{input} - \sum_{i=1}^{n} g_i(V - E_i)$$

If we further presume that the resistance through each ion channel is variable, voltage-dependent, and changes with respect to one or more gating variables *x*, which themselves change with respect to a steady state equation and a time "constant" equation tau, and are put to the power j_x before being applied to the conductance, we have the following final set of differential equations:

$$C\frac{dV}{dt} = I_{input} - \sum_{i=1}^{n} \bar{g}_i \left[\prod x^{j_x}\right](V - E_i) \qquad \frac{dx}{dt} = \frac{x_\infty(V) - x}{\tau_x(V)}$$

J2. Kinetic Models

Chemical reactions, which include secondary messenger pathways, are frequently modeled via kinetic models. Kinetic models are comprised of reaction diagrams and their associated rate equations in differential form. Conceptually, these can be derived by taking relatively simple assumptions about these systems. Firstly, we presume that all reactions are independent, and happen with a given probability over a given span of time. Secondly, we assume that the number of molecules or atoms available to form reactions is comparatively large.

As an example, we take the example of some quantity X_T of a single molecular species X, which has a probability p of decaying over the time span Δt. If we assume our container to have a fixed volume, then we can also simply presume that X_T is correlated to $[X]$, and treat them synonymously from this point forward. Since each molecule of X has the same probability p of decaying, the number of X molecules that will decay within the given time step is $p[X]$, or:

$$X \longrightarrow \emptyset \quad \Rightarrow \quad \frac{\Delta[X]}{\Delta t} = -p[X] \quad \Delta t \to 0 \quad \Rightarrow \quad \frac{d[X]}{dt} = -p[X]$$

If instead we have three molecular species: X, Y, and Z, governed by the following relationship:

$$X + Y \rightleftharpoons Z$$

We now must generate an equation for the rate of change of each of the species above. First, because X and Y must interact before they can react, we need to determine the total number of possible collisions between X and Y, multiply this by the probability of collision p_c, before multiplying by the probability of any given collision producing a reaction p_r. Since every member of X can collide with any member of Y, we have $X_T Y_T = [X][Y]$ reactions in the total volume of the system, and since we have a sufficiently large amount of both X and Y, any given collision won't change $[X]$ or $[Y]$ enough to merit handling each collision separately, nor do we have to worry about more than one X colliding with the same Y or vice versa, as this will be a comparatively low probability event. Thus, the quantity of X and Y that combines to form Z will be $p_c p_r [X][Y]$. When Z decays, as above, with some probability p_d, and knowing that every X and Y that combine form a Z, and vice versa, we get the following equations for the system:

$$\frac{\Delta[X]}{\Delta t} = p_d[Z] - p_c p_r[X][Y] \qquad \frac{d[X]}{dt} = p_d[Z] - p_c p_r[X][Y]$$
$$\frac{\Delta[Y]}{\Delta t} = p_d[Z] - p_c p_r[X][Y] \quad \Delta t \to 0 \quad \frac{d[Y]}{dt} = p_d[Z] - p_c p_r[X][Y]$$
$$\frac{\Delta[Z]}{\Delta t} = p_c p_r[X][Y] - p_d[Z] \qquad \frac{d[Z]}{dt} = p_c p_r[X][Y] - p_d[Z]$$

Based on these examples, we can now generate a more general equation for any possible reaction fitting the assumptions we've already taken:

$$\begin{aligned} a_{1,1}X_1 + a_{1,2}X_2 + \ldots + a_{1,n}X_n &\longrightarrow b_{1,1}X_1 + b_{1,2}X_2 + \ldots + b_{1,n}X_n \\ a_{2,1}X_1 + a_{2,2}X_2 + \ldots + a_{2,n}X_n &\longrightarrow b_{2,1}X_1 + b_{2,2}X_2 + \ldots + b_{2,n}X_n \\ &\vdots \\ a_{m,1}X_1 + a_{m,2}X_2 + \ldots + a_{m,n}X_n &\longrightarrow b_{m,1}X_1 + b_{m,2}X_2 + \ldots + b_{m,n}X_n \end{aligned}$$

From which *a* and *b* are of non-negative integer value. This produces the following set of differential equations:

$$for\ y = [1, n]$$
$$\frac{d[X_y]}{dt} = \sum_{k=1}^{m}\left[e_{y,k}\prod_{i=1}^{n}[X_i]^{b_{k,i}} - c_{y,k}\prod_{i=1}^{n}[X_i]^{a_{k,i}} \right]$$

Where $c_{y,k}$ and $e_{y,k}$ are rate constants set either experimentally, or by deriving the constant from the likelihoods of reaction.

J3. Spherical Diffusion of Calcium

One-dimensional radial diffusion of Ca^{2+} can effectively represent simplified diffusion within a sphere, by tracking Ca^{2+} as it moves successively through spherical shells comprising the sphere. When these shells of volume are assumed to be infinitely thin, we may derive the necessary differential equations based on the continuity equation in radial coordinates:

$$\frac{\partial \rho}{\partial t} = -\nabla \bullet J$$

Where $\nabla \bullet f$ for arbitrary *f* in spherical coordinates is:

$$\nabla \bullet f = \frac{\partial}{\partial r} f_r + \frac{2}{r} f_r + \frac{1}{r \sin\theta} \frac{\partial}{\partial \theta} f_\theta + \frac{1}{r} \frac{\partial}{\partial \phi} f_\phi + \frac{\cot\phi}{r} f_\phi$$

Knowing that Ca^{2+} flux J is a conserved quantity, as per Fick's First Law of diffusion:

$$J = -D\nabla[Ca^{2+}]$$

Where D is the diffusion constant, a quantity that often varies between 0.2 and 0.6 $\mu m^2/ms$ in neurons and other cells (Allbritton et al 1992, Blaustein & Hodgkin 1969, Schutter 2009, Zhou & Neher 1993). Assuming ubiquitous concentration along each shell of volume lets us presume that $f_\phi = f_\phi = 0$ and $f_r = f$, thus:

$$\nabla \bullet f = \frac{\partial}{\partial r} f + \frac{2}{r} f$$

By combining this equation with the continuity equation and Fick's First Law, we come to Fick's Second Law in spherical coordinates, assuming fixed θ and ϕ:

$$\frac{\partial[Ca^{2+}]}{\partial t} = -\nabla \bullet J$$

$$\frac{\partial[Ca^{2+}]}{\partial t} = D\nabla \bullet (\nabla[Ca^{2+}])$$

$$\frac{\partial[Ca^{2+}]}{\partial t} = D\nabla \bullet \frac{\partial[Ca^{2+}]}{\partial r}$$

$$\frac{\partial[Ca^{2+}]}{\partial t} = D\left(\frac{\partial^2[Ca^{2+}]}{\partial r^2} + \frac{2}{r} \frac{\partial[Ca^{2+}]}{\partial r} \right)$$

From Fick's Second Law, we may now discretize this differential equation to make it manageable for numerical integration. Each of the three differentials above is considered separately through central ($\delta_{\Delta r}$), forward ($\Delta_{\Delta r}$), and backward ($\nabla_{\Delta r}$) differences, where τ is the time step, and ρ is the volume compartment:

For the first derivative over radius:

$$\frac{\partial[Ca^{2+}]}{\partial r} = \frac{mean(\Delta_{\Delta r}[Ca^{2+}], \nabla_{\Delta r}[Ca^{2+}])}{\Delta r} = \frac{1}{2} \frac{([Ca^{2+}]^\tau_{\rho+1} - [Ca^{2+}]^\tau_\rho) + ([Ca^{2+}]^\tau_\rho - [Ca^{2+}]^\tau_{\rho-1})}{\Delta r}$$

$$= \frac{[Ca^{2+}]^\tau_{\rho+1} - [Ca^{2+}]^\tau_{\rho-1}}{2\Delta r}$$

For the second derivative over radius:

$$\frac{\partial^2[Ca^{2+}]}{\partial r^2} = \frac{\delta_{\Delta r}^2[Ca^{2+}]}{\Delta r^2} = \frac{([Ca^{2+}]_{\rho+1}^{\tau} - [Ca^{2+}]_{\rho}^{\tau}) - ([Ca^{2+}]_{\rho}^{\tau} - [Ca^{2+}]_{\rho-1}^{\tau})}{\Delta r^2}$$
$$= \frac{[Ca^{2+}]_{\rho+1}^{\tau} - 2[Ca^{2+}]_{\rho}^{\tau} + [Ca^{2+}]_{\rho-1}^{\tau}}{\Delta r^2}$$

For the time derivative:

$$\frac{\partial[Ca^{2+}]}{\partial t} = \frac{\Delta_{\Delta t}[Ca^{2+}]}{\Delta t} = \frac{[Ca^{2+}]_{\rho}^{\tau+1} - [Ca^{2+}]_{\rho}^{\tau}}{\Delta t}$$

When combined this gives us:

$$\frac{[Ca^{2+}]_{\rho}^{\tau+1} - [Ca^{2+}]_{\rho}^{\tau}}{\Delta t} = D\left(\frac{[Ca^{2+}]_{\rho+1}^{\tau} - 2[Ca^{2+}]_{\rho}^{\tau} + [Ca^{2+}]_{\rho-1}^{\tau}}{\Delta r^2} + \frac{[Ca^{2+}]_{\rho+1}^{\tau} - [Ca^{2+}]_{\rho-1}^{\tau}}{r\Delta r}\right)$$
$$[Ca^{2+}]_{\rho}^{\tau+1} = [Ca^{2+}]_{\rho}^{\tau} + \frac{D\Delta t}{\Delta r^2}\left(\frac{[Ca^{2+}]_{\rho+1}^{\tau} - 2[Ca^{2+}]_{\rho}^{\tau} + [Ca^{2+}]_{\rho-1}^{\tau}}{\Delta r^2} + \frac{[Ca^{2+}]_{\rho+1}^{\tau} - [Ca^{2+}]_{\rho-1}^{\tau}}{r\Delta r}\right)$$

Though one can stop here, through a simple substitution, the above equation can be simplified without loss of generality. Merely by substituting $u = r[Ca^{2+}]$, we can effectively reduce the equation for Fick's Second Law in spherical coordinates, to one in linear coordinates:

$$\frac{\partial[Ca^{2+}]}{\partial t} = D\left(\frac{\partial^2[Ca^{2+}]}{\partial r^2} + \frac{2}{r}\frac{\partial[Ca^{2+}]}{\partial r}\right)$$
$$\frac{1}{r}\frac{\partial u}{\partial t} = D\left(\frac{\partial^2\left(\frac{u}{r}\right)}{\partial r^2} + \frac{2}{r}\frac{\partial\left(\frac{u}{r}\right)}{\partial r}\right)$$
$$\frac{1}{r}\frac{\partial u}{\partial t} = D\left(\frac{\partial}{\partial r}\left[-\frac{u}{r^2} + \frac{1}{r}\frac{\partial u}{\partial r}\right] + \frac{2}{r}\left[-\frac{u}{r^2} + \frac{1}{r}\frac{\partial u}{\partial r}\right]\right)$$
$$\frac{\partial u}{\partial t} = D\left(-\frac{r}{r^2}\frac{\partial u}{\partial r} + \frac{2ru}{r^3} - \frac{r}{r^2}\frac{\partial u}{\partial r} + \frac{r}{r}\frac{\partial^2 u}{\partial r^2} + \frac{2}{r}\frac{\partial u}{\partial r} - \frac{2u}{r^2}\right)$$
$$\frac{\partial u}{\partial t} = D\left(\left[\frac{2}{r}\frac{\partial u}{\partial r} - \frac{2}{r}\frac{\partial u}{\partial r}\right] + \left[\frac{2u}{r^2} - \frac{2u}{r^2}\right] + \frac{\partial^2 u}{\partial r^2}\right)$$
$$\frac{\partial u}{\partial t} = D\frac{\partial^2 u}{\partial r^2}$$

Subsequently, this results in the following discretization, which was used in all simulations:

$$u_{\rho}^{\tau+1} = u_{\rho}^{\tau} + \frac{D\Delta t}{\Delta r^2}\left(\frac{u_{\rho+1}^{\tau} - 2u_{\rho}^{\tau} + u_{\rho-1}^{\tau}}{\Delta r^2}\right)$$

Conversion back to $[Ca^{2+}]$ from u only requires dividing by r, where $\rho = \{c1, c2, ..., c\max - 1\}$ represents the Ca^{2+} compartment:

$$\frac{\partial [Ca^{2+}]_{\rho}}{\partial t} = D\left(\frac{\partial^2 [Ca^{2+}]_{\rho}}{\partial r^2} + \frac{2}{r}\frac{\partial [Ca^{2+}]_{\rho}}{\partial r}\right)$$

In this manner, spherical diffusion of Ca^{2+} may be simply handled as a set of $|\rho|$ ordinary differential equations.